

Internal Report
DESY F31-90-01
January 1990

**Measurement of Total Hadronic Cross Section
 $\sigma(e^+e^- \rightarrow \text{Hadrons})$ in the Continuum
at the C.M. Energy $W = 9.39 \text{ GeV}$
and Determination of Γ_{ee} of the
 $\Upsilon(1S)$ and $\Upsilon(2S)$ Resonances**

by

Z. Jakubowski

Eigentum der	DESY	Bibliothek
Property of		library
Zugang:		
Acquisition:	07. DEZ. 1990	
Leihfrist:	7	Tage
Loan period:	7	days

DESY behält sich alle Rechte für den Fall der Schutzrechtserteilung und für die wirtschaftliche Verwertung der in diesem Bericht enthaltenen Informationen vor.

DESY reserves all rights for commercial use of information included in this report, especially in case of filing application for or grant of patents.

**“Die Verantwortung für den Inhalt dieses
Internen Berichtes liegt ausschließlich beim Verfasser”**

Interner Bericht
DESY F31-90-01
January 1990

**Measurement of total hadronic cross section
 $\sigma(e^+e^- \rightarrow \text{hadrons})$ in the continuum
at the c.m. energy $W=9.39$ GeV
and determination of Γ_{ee} of the
 $\Upsilon(1S)$ and $\Upsilon(2S)$ resonances** *cu*

Zbigniew Jakubowski
Institute of Nuclear Physics, Cracow
and
Deutsches Elektronen Synchrotron, Hamburg

November 1989
Ph.D. Dissertation
Cracow Institute of Nuclear Physics

She walked up to me so gracefully
She took my crowns of thorns
Come in, she said, I'll give you
Shelter from the storm

Shelter from the Storm
Bob Dylan

To my wife

Abstract

This work is based on a study of e^+e^- collisions in the energy region of $\Upsilon(1S)$ and $\Upsilon(2S)$ resonances. Using the data taken by the Crystal Ball Detector in the continuum below $\Upsilon(1S)$ we have determined the value of R , the ratio of the hadronic cross section to the Born cross section of μ pair production, at c.m. energy $W = 9.39$ GeV to be

$$R = 3.48 \pm 0.04 \pm 0.14.$$

This is the most precise measurement of R below the $\Upsilon(1S)$ threshold. Resonance scan data were used to determine the leptonic partial widths Γ_{ee} of $\Upsilon(1S)$ and $\Upsilon(2S)$. We find

$$\Gamma_{ee}(\Upsilon(1S)) = (1.34 \pm 0.03 \pm 0.06) \text{ keV}$$

$$\Gamma_{ee}(\Upsilon(2S)) = (0.56 \pm 0.03 \pm 0.02) \text{ keV}.$$

The method of obtaining Γ_{ee} from the measured excitation curve is not unique. Our results are $\sim 10\%$ higher than those already published mainly because we used an internally consistent treatment of the radiative corrections. We discuss the effect of applying different theoretical prescriptions for the radiative corrections on Γ_{ee} .

Both results presented here require the knowledge of the absolute cross sections to a high precision. Uncertainties in the corrections to the cross section due to detector efficiency constitute the main source of the systematic error. To minimize these uncertainties substantial modifications of the detector simulation program GHEISHA were necessary to obtain a satisfactory description of the data. The modifications may be of importance for other calorimetric experiments.

Streszczenie

Prezentowana rozprawa została wykonana w oparciu o dane e^+e^- w okolicach energii odpowiadającej masie rezonansów $\Upsilon(1S)$ i $\Upsilon(2S)$. Używając danych współpracy Crystal Ball zebranych w kontinuum poniżej rezonansu $\Upsilon(1S)$ wyznaczono wartość R , t.j. stosunek hadronowego przekroju czynnego do Bornowskiego przekroju czynnego na produkcję par mionowych, przy energii układu środka masy $W = 9.39$ GeV otrzymując:

$$R = 3.48 \pm 0.04 \pm 0.14.$$

Jest to najbardziej dokładny z dotychczas opublikowanych pomiar R poniżej progu $\Upsilon(1S)$. Dane ze skanu rezonansu zostały wykorzystane do wyznaczenia cząstkowej szerokości leptonowej Γ_{ee} rezonansów $\Upsilon(1S)$ i $\Upsilon(2S)$. Zmierzone:

$$\Gamma_{ee}(\Upsilon(1S)) = (1.34 \pm 0.03 \pm 0.06) \text{ keV}$$

$$\Gamma_{ee}(\Upsilon(2S)) = (0.56 \pm 0.03 \pm 0.02) \text{ keV}.$$

Metoda wyznaczenia Γ_{ee} ze zmierzonej krzywej rezonansowej nie jest jedyna. Nasze rezultaty są $\sim 10\%$ wyższe od dotychczas publikowanych głównie z powodu odmiennego traktowania poprawek radiacyjnych. Przedyskutowano wpływ różnych używanych metod na mierzoną wartość Γ_{ee} .

Oba przedstawione tutaj rezultaty wymagają znajomości absolutnego przekroju czynnego z dużą dokładnością. Niepewność wyznaczenia poprawek aparaturowych do przekroju czynnego stanowi główne źródło błędów systematycznych. Aby zminimalizować tę niepewność konieczne były znaczne zmiany programu symulacyjnego GHEISHA. Przedstawione modyfikacje mogą być również istotne dla innych eksperymentów kalorymetrycznych.

Contents

1 Introduction	5
2 Basic Concepts	7
2.1 Particle Production in the Continuum	8
2.2 Definition of R	9
2.3 Resonance Production and Decays	13
2.4 Radiative Corrections and Definition of Γ_{ee}	14
3 Experimental Layout	18
3.1 DORIS-II	18
3.2 The Crystal Ball Detector	20
3.3 Organization of the Data Acquisition	23
3.4 Interpretation of the Energy Deposited in the Crystals	25
4 Selection of Hadronic Events	28
4.1 Selection Criteria	28
4.2 Efficiency Determination	41
4.3 Background	42
4.3.1 QED Processes	42
4.3.2 Two-Photon Collisions	43
4.3.3 Beam-gas Background	44
5 Determination of Γ_{ee}	50
5.1 Γ_{ee} Measurements	50
5.1.1 Γ_{ee} of the $\Upsilon(1S)$	53
5.1.2 Γ_{ee} of the $\Upsilon(2S)$	56
5.1.3 Systematic errors for Γ_{ee}	57
5.2 Discussion of Γ_{ee} Results	58
6 Determination of R at $W = 9.39$ GeV	61
6.1 Measurement of R	61
6.2 Systematic Error on R	61

6.3 Discussion of the Results on R	63
7 Summary	67
A Monte Carlo Techniques	69
A.1 Event Simulation	69
A.2 On Monte Carlo Testing Techniques	70
A.3 Changes of the GHEISHA Code	72
A.3.1 Geometry Routines	73
A.3.2 Checking of the dE/dx Constants	76
A.3.3 Multiple Scattering	79
A.3.4 Absorption of Negatively Charged Particles	81
A.3.5 Light Saturation Problem	88
A.3.6 Neutron Transport	89
A.4 General Remarks on Monte Carlo Techniques	90
B Luminosity Measurement	92
C Asymmetric Errors of Poisson Distribution	94

1. Introduction

Ever since the discovery of the Υ resonances in 1977 [1] measurements of their leptonic partial decay widths Γ_{ee} have been of great interest. The measured values support the interpretation of the Υ family as bound states of charge $|q| = 1/3$ particles and serve as tests for potential models, which describe the $\Upsilon(nS)$ as the n^3S_1 states of a $b\bar{b}$ system. Moreover, the total widths Γ_{tot} are usually derived from the measured Γ_{ee} widths via the relation $\Gamma_{tot} = \Gamma_{ee}/B_{\mu\mu}$, where $B_{\mu\mu}$ is the $\Upsilon(nS)$ branching ratio to μ pairs. (Hereafter we assume lepton universality.)

In this thesis we report on a precision measurement of Γ_{ee} for the $\Upsilon(1S)$ and $\Upsilon(2S)$ resonances performed with the Crystal Ball detector operating at the DORIS-II e^+e^- storage ring at DESY. Γ_{ee} is determined by measuring the cross section for the process $e^+e^- \rightarrow \text{hadrons}$ as a function of the e^+e^- center-of-mass (c.m.) energy in the region of the resonance. We use four scans of the $\Upsilon(1S)$ and one of the $\Upsilon(2S)$. From the $\Upsilon(1S)$ scans and the continuum data below the resonance we also obtain a value for R , the ratio of non-resonant hadronic cross section to the Born cross section of μ pair production, at c.m. energy $W = 9.39$ GeV. It is worth mentioning here that the measurement of R was one of the first cases where radiative corrections were necessary to explain the MARK I data [2]. The author was participating in the LENA scan experiment with the main aim of finding exotic phenomena in the continuum below $\Upsilon(1S)$. Consequent application of the radiative corrections allows explanation of the data without any exotic physics [3].

Extracting Γ_{tot} from $\Gamma_{ee}/B_{\mu\mu}$ requires consistent application of radiative corrections in the separate determinations of Γ_{ee} and $B_{\mu\mu}$, which has not been the case for previously quoted values of Γ_{tot} for the Υ resonances. In this thesis the radiative corrections are done in such a way that our Γ_{ee} can be used with previous determinations of $B_{\mu\mu}$. We compare our result to previous Γ_{ee} measurements by re-normalizing them to correspond to the same radiative corrections.

The hadron production in the continuum and definition of R are discussed in sections 2.1 and 2.2. Γ_{ee} and in turn Γ_{tot} strongly depend on the parametrization used for the visible cross section $\bar{\sigma}(W)$. The different theoretical formulations for it are in some detail discussed in section 2.4. Section 3.2 gives a short description of the Crystal Ball detector. The hadronic event selection criteria and selection efficiencies are shown in sections 4.1 and 4.2, respectively. Section 4.3 is devoted to the backgrounds in the hadronic data sample. In section 5.1 we discuss our procedure to determine Γ_{ee} and present our results. The effect on Γ_{ee} of different theoretical formulations for $\bar{\sigma}(W)$ is discussed in section 5.2. The measurement of R is given in section 6, which is followed by section 7 containing the final conclusions. The apparatus

response was simulated by the EGS for e^+ and γ , and by GHEISHA for all other particles. Since the changes applied to the GHEISHA Monte Carlo simulation program can be useful for other experiments they are presented in more detail in appendix A. The luminosity determination is discussed in appendix B.

The results of this analysis have been published [4].

2. Basic Concepts

We believe that all known particles are composed of two types of fermions, the quarks and the leptons. There also exist intermediate bosons that mediate the forces between the fermions. Basic properties of the fermions arranged in generations are shown in table 2.1. Quarks carry an additional quantum number—color (red, blue, green). Free quarks are not observed in the experiment. All experimentally observed final states are color singlets and we do not observe states with a fractional charge. This experimental fact is called “confinement”. The mesons are constructed as quark-antiquark states while baryons are three quark conglomerates such that the final objects are colorless. No experimental evidence has been found that leptons and quarks have any internal substructure. The question of generation number is not resolved at the present level of theory. Leptons carry their lepton family quantum number. This number is conserved in all known types of interactions.

There are basically five electromagnetic processes leading to particle production at e^+e^- storage ring at c.m. energies around 10 GeV. These are: a) one photon annihilation leading to fermion pair production in the final state, b) one photon annihilation leading to resonance production in the final state, c) elastic scattering, d) and e) annihilation into two photons, and f) $\gamma\gamma$ interactions. Fig. 2.1 shows the corresponding graphs in the lowest order QED. Processes $e^+e^- \rightarrow e^+e^-$ and $e^+e^- \rightarrow \gamma\gamma$ (graphs (a), (c), (d), and (e), respectively) are used for the normalization of the experimental data. They are discussed more explicitly in appendix B. Process (f) contributes to the experimental background. More details about it will be given in section 4.3.2. In the following sections processes of type (a) and (b) are discussed.

In the next sections we will be dealing with so-called “radiative corrections”. The name “radiative corrections” is very often used to describe various things. In our case by radiative corrections we will refer to the fact that any process including charged particles implies some

Table 2.1: Basic properties of quarks and leptons

		fermions				
type	particles			properties		
	1	2	3	electric charge	color	
quarks	u	c	t?	+2/3	r b g	
	d	s	b	-1/3	r b g	
leptons	ν_e	ν_μ	ν_τ	0	0	
	e	μ	τ	-1	0	

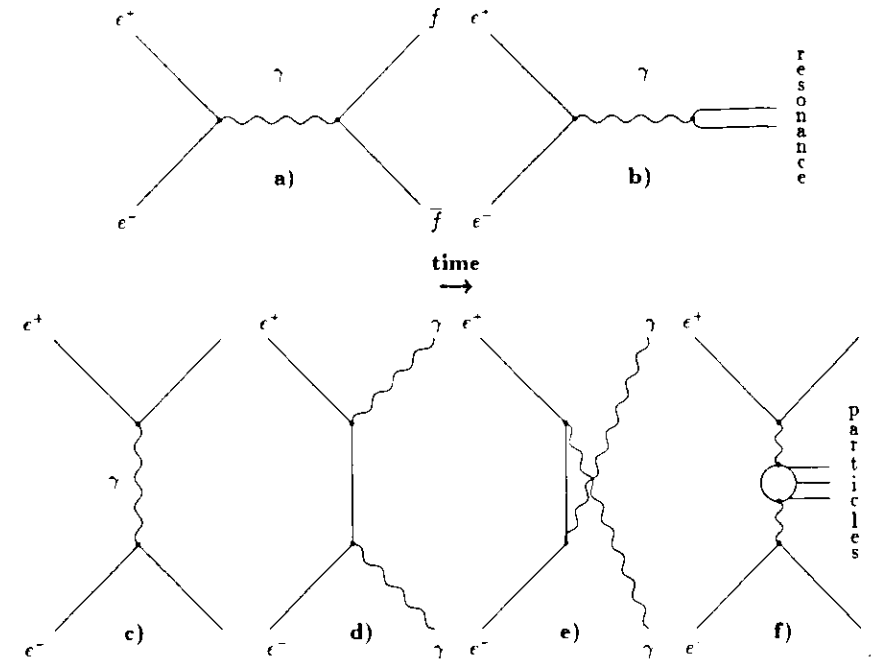


Figure 2.1: Lowest order processes contributing to particle production in e^+e^- collisions. a) One photon annihilation leading to fermion pair production in the final state; b) One photon annihilation leading to resonance production in the final state; c) Elastic scattering; d) and e) Annihilation into two photons, and f) $\gamma\gamma$ interactions.

rearrangement of the electromagnetic current when going from the initial state to the final one. This implies that some charge acceleration takes place and as the effect photons are radiated. The name “radiative corrections” is sometimes by analogy extended to the higher order QCD or electroweak corrections.

2.1 Particle Production in the Continuum

Particle production in the continuum much below Z' is dominated by one photon annihilation (graph 2.1a). The following discussion will not hold for the process $e^+e^- \rightarrow e^+e^-$ as in this case we have to consider also elastic scattering (graph 2.1c). In the c.m. system the following expression is obtained in lowest order QED for the *fermion-antifermion* pair angular distribution

$$\frac{d\sigma}{d\Omega} = \frac{\alpha^2}{4W^2} \beta_f q_f^2 \left[(1 + \cos^2 \theta) + (1 - \beta_f^2) \sin^2 \theta \right], \quad (2.1)$$

where α is the electromagnetic coupling constant, β_f the velocity of particles within the produced pair in speed of light units, E_{beam} beam energy, θ the angle with respect to beam axis, $W = 2E_{\text{beam}}$ the c.m. energy and q_f the charge of produced fermions in electron charge units. If $\beta_f \approx 1$ eq. 2.1 reduces to

$$\frac{d\sigma}{d\Omega} = \frac{\alpha^2}{4W^2} q_f^2 (1 + \cos^2 \theta). \quad (2.2)$$

Integration over the full solid angle leads to

$$\sigma^\circ(e^+e^- \rightarrow ff) = \frac{4\pi}{3} \frac{\alpha^2}{W^2} q_f^2. \quad (2.3)$$

Hereafter, by the superscript $^\circ$ we mark the fact that the calculation is done in lowest order QED/QCD. This convention will be kept throughout this thesis. In case of quark-antiquark pair production we have to account for the number of colors. Thus eq. 2.3 reads

$$\sigma^\circ(e^+e^- \rightarrow \text{quark-antiquark}) = \frac{4\pi\alpha^2}{W^2} q_f^2. \quad (2.4)$$

Due to confinement we do not observe free quarks but multihadron final states. The production of quarks is independent of the hadronization because of asymptotic freedom, i.e. the confinement plays an essential role at large distances between quarks while the production of quarks is believed to be pointlike. Thus the expression for the lowest order QCD hadronic cross section can be written as follows

$$\sigma^\circ(e^+e^- \rightarrow \text{hadrons}) = \frac{4\pi\alpha^2}{W^2} \sum_{i=1}^{n_f} q_i^2, \quad (2.5)$$

where n_f is the number of opened quark thresholds. It is worth to note here the $1/W^2$ energy dependence of the cross section. It is a typical feature of one photon annihilation.

2.2 Definition of R

R is defined as the ratio of the non-resonant hadronic cross section to the Born cross section of μ pair production

$$R = \frac{\sigma^\circ(e^+e^- \rightarrow \text{hadrons})}{\sigma^\circ(e^+e^- \rightarrow \mu^+\mu^-)} = \frac{\sigma^\circ(e^+e^- \rightarrow \text{hadrons})}{\sigma^\circ(e^+e^- \rightarrow \mu^+\mu^-)}. \quad (2.6)$$

The lowest order μ pair production cross section at fixed c.m. energy W is given by eq. 2.3 [5]

$$\sigma^\circ(e^+e^- \rightarrow \mu^+\mu^-) = \frac{4\pi}{3} \frac{\alpha^2}{W^2} = \frac{86.9}{W^2} \text{ nb GeV}^2. \quad (2.7)$$

In lowest order QCD the theoretical prediction for R is given by:

$$R^\circ = 3 \sum_{i=1}^{n_f} q_i^2 \stackrel{n_f=4}{=} 3^{1/3}. \quad (2.8)$$

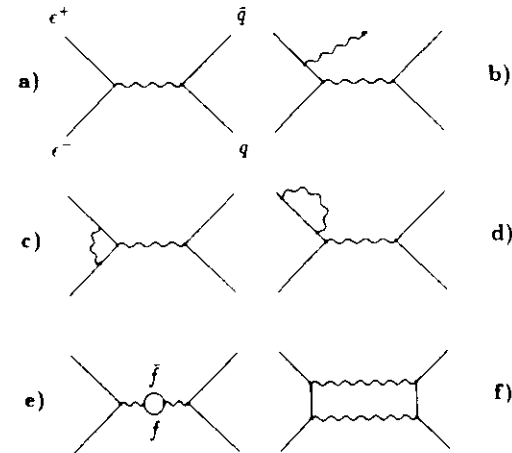


Figure 2.2: Representative set of Feynman diagrams which contribute to $\mathcal{O}(\alpha^3)$ in $e^+e^- \rightarrow q\bar{q}$. To this order the graphs c-f contribute only through their interference with the lowest order graph a.

where q_i are quark charges and n_f is the number of opened quark thresholds. The factor of 3 accounts for the number of colors. Historically, R was one of those quantities where we explicitly needed to account for the color degree of freedom. Such a definition of R makes its experimental determination sensitive to any effects leading to hadrons in the final state.

The first order cross section, as employed in the definition of R , has to be calculated from the measured cross-section by applying radiative corrections. The representative set of the Feynman graphs for the process $e^+e^- \rightarrow q\bar{q}$ is shown in fig. 2.2. We have also to consider the graph 2.2 b representing the initial state bremsstrahlung, since experimentally we cannot distinguish radiative from non-radiative events, at least not for low photon energies. In fact the cross-section for graph 2.2 b diverges for low photon energies; however, this divergence is cancelled by the interference term resulting from the lowest order graph 2.2 a and the vertex correction graph 2.2 c (Kinoshita-Lee-Nauenberg theorem). Generally, we can write the following expression for a hadronic cross section at given c.m. energy W

$$\sigma(W) = \int_0^{k_{\text{max}}} \sigma(W, \vec{k}) d\vec{k} \quad (2.9)$$

where $|\vec{k}| \equiv k = 2E_{\text{photon}}/W$ is the fraction of the beam energy carried by the radiated photon and $\sigma(W, \vec{k})$ is the true differential cross-section. The maximum momentum k_{max} carried away by a photon is limited by the requirement that at least one π pair can be produced and yields

$$k_{\text{max}} = 1 - \frac{4m_\pi^2}{W^2}. \quad (2.10)$$

The emission of the photons can influence selection efficiencies by changing the multiplicity and topology of a produced final state. As an example we can consider a high energy photon staying undetected in the beam pipe. It will influence both, the energy deposited in the detector and the topology of the whole event due to the boost of the center of mass of the remaining $q\bar{q}$ system. All those effects are taken into account automatically in the efficiency calculation by the Monte Carlo method described below.

Evaluation of the graphs in fig. 2.2 yields a rather complicated expression for the differential cross-section $\sigma(W, \vec{k})$ which is best dealt with in form of a Monte Carlo event generation program. However, when integrated over the photon energies and emission directions the expression becomes relatively simple:

$$\sigma(W) = \sigma^c(W)(1 + \delta_R) \quad (2.11)$$

The factor $(1 + \delta_R)$ accounts for the radiative corrections. The term δ_R contains the following contributions

$$\delta_R = \delta_A + \delta_\mu + \delta_\tau + \delta_{quarks} + \delta_{hard} \quad (2.12)$$

where δ_A originates from soft photon bremsstrahlung (graph b), vertex correction (graph c), correction of the electron propagator (graph d), and electron vacuum polarization (graph e of fig. 2.2):

$$\delta_A = t \ln k_{min} + \frac{2\alpha}{\pi} \left[\frac{13}{6} \ln \frac{W}{m_e} + \frac{1}{6} \pi^2 - \frac{14}{9} \right] \quad (2.13)$$

with

$$t = \frac{2\alpha}{\pi} \left(2 \ln \frac{W}{m_e} - 1 \right) \quad (2.14)$$

the so-called equivalent radiator thickness. The photon energy cutoff k_{min} is an arbitrarily selected value such that photons below the k_{min} do not change the selection efficiency. The terms δ_μ , δ_τ , and δ_{quarks} account for the leptonic and hadronic vacuum polarization corresponding to graph 2.2e. Term δ_A contains the electron vacuum polarization (see eq. 2.15). It is customary to write the vertex correction and the soft photon contribution as one term since an infrared divergence in the initial state radiation is cancelled by including the vertex correction. For the vacuum polarization due to e , μ , τ the correction depends only on lepton mass and is approximately given by

$$\delta_{e,\mu,\tau} = \frac{2\alpha}{\pi} \left(\frac{2}{3} \ln \frac{W}{m_{e,\mu,\tau}} - \frac{5}{9} \right). \quad (2.15)$$

The correction δ_{quarks} has to be evaluated numerically [6].

The term δ_{hard} is responsible for the hard photon emission where by "hard photon" we mean a photon of energy above k_{min} . In the parametrization according to ref. [7] it yields

$$\delta_{hard} = \frac{1}{2} t \left[2 \ln \frac{k_{max}}{k_{min}} - \ln \frac{(1 - k_{max})}{(1 - k_{min})} - (k_{max} - k_{min}) \right]. \quad (2.16)$$

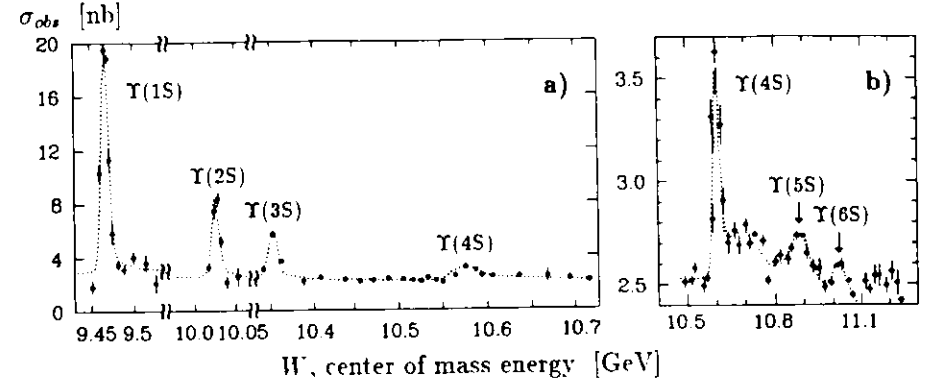


Figure 2.3: The e^+e^- total cross section: a) the energy region $\Upsilon(1S)$ through $\Upsilon(4S)$; b) The energy region $\Upsilon(4S)$ through $\Upsilon(6S)$ (from ref. [8]).

The acceptance of the apparatus is normally found by the Monte Carlo method since the integration is not easy (or impossible) to perform analytically due to the complicated shape of the apparatus acceptance function. Note that in the acceptance we have to include not only the geometrical effects but also reconstruction and selection efficiencies etc., i.e. effects difficult to express in terms of analytical functions. Technically we generate the events with or without the radiative photon depending on the generated k value (photons with energy below k_{min} are not produced). The apparatus acceptance is then found as the ratio of the number of Monte Carlo events passing the selection criteria, $N_{accepted}$, to the total number of generated events, $N_{generated}$:

$$\epsilon = \frac{\int_0^{k_{max}} \sigma(W, \vec{k}) \tilde{\epsilon}(\vec{k}) d\vec{k}}{\int_0^{k_{max}} \sigma(W, \vec{k}) d\vec{k}} = \frac{N_{accepted}}{N_{generated}} \quad (2.17)$$

where $\tilde{\epsilon}(\vec{k})$ is the apparatus acceptance function.

From eq. 2.11 we finally get

$$\sigma^c = \frac{\sigma^{obs}(W)}{(1 + \delta_R)\epsilon} \quad (2.18)$$

Combining 2.6 with 2.18 we obtain the following expression for R

$$R = \frac{R^{obs}}{(1 + \delta_R)\epsilon} \quad (2.19)$$

where $R^{obs} = \sigma^{obs}(e^+e^- \rightarrow q\bar{q}) / \sigma^c(e^+e^- \rightarrow \mu^+\mu^-)$. Figure 2.3 shows the behavior of the total cross section in the Υ energy region.

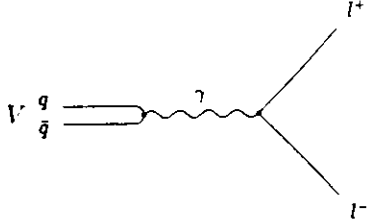


Figure 2.4: A lowest order QCD diagram of the leptonic decay of a vector meson.

2.3 Resonance Production and Decays

In one photon annihilation we can directly produce resonances carrying the photon quantum numbers, i.e. $J^{PC} = 1^{--}$ (vector mesons). The decay of the resonances leads, in general, to multiparticle final states. The partial width for the decay of the vector meson V to a lepton pair (fig. 2.4) is given by the Van Royen-Weisskopf formula [9]

$$\Gamma(V \rightarrow l^+ l^-) = \frac{16\pi\alpha^2 q^2}{M_V^2} |\psi(0)|^2 \quad (2.20)$$

where q^2 is the squared sum of the charges of the quarks in the meson. A comparison with eq. 2.4 reveals the similarities. The decay of the vector meson is naturally the time-reversed process of its formation. So the expressions should be equal apart from phase space factors. The amplitude of the quark-antiquark wave function at the origin is denoted by $\psi(0)$. The factor $|\psi(0)|^2$ reflects the pointlike production of the resonance.

The formation and decay of the resonance with mass M of angular momentum J in the collision of the particles with spins s_a and s_b are described by a Breit-Wigner formula

$$\sigma_{el}(W) = \frac{4\pi}{W^2} \frac{(2J+1)\Gamma_{el}^2}{(2s_a+1)(2s_b+1)[(M-W)^2 + \Gamma_{tot}^2/4]} \quad (2.21)$$

where Γ_{tot} is the total width and W the c.m. energy. The subscript el refers to the fact that this formula is valid for elastic processes $a + b \rightarrow resonance \rightarrow a + b$. Generally the term Γ_{el}^2 in eq. 2.21 should be replaced by $\Gamma_i \Gamma_f$, where Γ_i and Γ_f are the partial widths corresponding to the initial and the final state.

It is useful to define the decay branching ratio B_i for the process i as

$$B_i = \frac{\Gamma_i}{\Gamma_{tot}} \quad (2.22)$$

The total width of any of $\Upsilon(1S)$, $\Upsilon(2S)$, and $\Upsilon(3S)$ is in the range 30-50 keV. The process involving the annihilation of the quarks of an intermediate resonant state (like the one in fig. 2.4) is suppressed with respect to the situation when the quarks survive its decay. In case of the first three members of the Υ family the situation that the b quarks survive is kinematically impossible and this is reflected in the small values of their total widths. The

Table 2.2: $\Upsilon(1S)$ branching ratios [5]. Note that the first three branching ratios carry the uncertainty of $B_{\mu\mu}$ and α_s measurements.

Decay	Branching Ratio
$\Upsilon(1S) \rightarrow 3g$	79.5%
$\Upsilon(1S) \rightarrow q\bar{q}$	9.2%
$\Upsilon(1S) \rightarrow \gamma g g$	2.5%
$\Upsilon(1S) \rightarrow e^+ e^-$	$(2.8 \pm 0.3)\%$
$\Upsilon(1S) \rightarrow \mu^+ \mu^-$	$(2.8 \pm 0.2)\%$
$\Upsilon(1S) \rightarrow \tau^+ \tau^-$	$(3.2 \pm 0.4)\%$

production of open beauty is possible in the case of $\Upsilon(4S)$ and this is reflected by its total width of ~ 19 MeV.

The decays of the lower members of the Υ family can proceed via the following channels:

1. $\Upsilon \rightarrow 3g$ (decay to three gluons);
2. $\Upsilon \rightarrow \gamma g g$;
3. $\Upsilon \rightarrow \gamma^* \rightarrow f\bar{f}$ where $f\bar{f}$ is a fermion pair;
4. $\Upsilon \rightarrow \gamma\gamma\gamma$.

Process No. 4 has a negligible cross section. The width for the dominant decay $\Upsilon \rightarrow 3g$ is given by [10]

$$\Gamma(\Upsilon \rightarrow 3g) = \frac{160\alpha_s^3(\pi^2 - 9)}{81 M_\Upsilon^2} |\psi(0)|^2 \quad (2.23)$$

The ratio

$$\frac{\Gamma(\Upsilon \rightarrow \gamma g g)}{\Gamma(\Upsilon \rightarrow 3g)} = \frac{36g_s^2}{5} \frac{\alpha}{\alpha_s(Q^*)} \left[1 + \frac{\alpha_s(Q^*)}{\pi} (2.2 \pm 0.6) + \dots \right] \quad (2.24)$$

is one of the best quantities that can be used to measure the strong coupling constant [11]. The strong coupling constant used is the one found within the \overline{MS} renormalization scheme with $Q^* = 0.157M_\Upsilon$, wherein to similar structures of the amplitudes cause the large QCD corrections to cancel almost completely. Q^* is the so-called optimal scale [11], specific for a given process.

Table 2.2 shows the $\Upsilon(1S)$ decay branching ratios. The direct decay of $\Upsilon \rightarrow e^+ e^-$ is a background to our luminosity sample (see sect. B); the luminosity has to be corrected for this contribution.

2.4 Radiative Corrections and Definition of Γ_{ee}

The measured excitation curve $\sigma(W)$ of the resonance in the process $e^+ e^- \rightarrow \Upsilon \rightarrow hadrons$ is used to obtain Γ_{ee} . Without QED radiative corrections the cross section for the formation

of the Υ in e^+e^- annihilation has a Breit-Wigner form of width Γ_{tot} (eq. 2.21). For the $\Upsilon(1S)$ and $\Upsilon(2S)$ Γ_{tot} is about two orders of magnitude smaller than the r.m.s. spread Δ caused by synchrotron radiation in the c.m. energy of the storage ring. For DORIS-II $\Delta \approx 8$ MeV. Thus the Breit-Wigner can be safely approximated by a *delta* function, $\sigma_{BW} = A^\circ \delta(W - M)$, with A° the area of the Breit-Wigner and M the mass of the resonance:

$$A^\circ = \frac{6\pi^2}{M^2} \Gamma_{ee}^\circ B_{had} \quad (2.25)$$

where B_{had} is the resonance branching ratio into hadrons. Convoluting this δ -function with the Gaussian distribution of the beam energy gives the effective lowest-order cross section:

$$\sigma^\circ(W) = A^\circ \frac{\exp(-z^2/2)}{\Delta\sqrt{2\pi}}, \quad z \equiv \frac{W - M}{\Delta}. \quad (2.26)$$

The $^\circ$'s in these equations indicate that the quantities are to lowest order in QED, corresponding to the Feynman graph of fig. 2.5 a. The $\sigma^\circ(W)$ must then be multiplied by the efficiency for detecting hadronic events in order to get the observed cross section; this factor is discussed in section 5.1.1. Here we are concerned with the QED radiative corrections to the *production* cross section $\sigma^\circ(W)$. They change both its shape and its normalization. The relevant Feynman diagrams to $\mathcal{O}(\alpha^3)$ are shown in fig. 2.5 a-e.

Radiative corrections were initially calculated by Yennie et al. [12] and Bonneau and Martin [6]. Several other theoretical calculations have appeared since then [13-17]. Generally, the result is a convolution between the lowest order cross section $\sigma^\circ(W)$ and a photon energy distribution function which mainly reflects a bremsstrahlung energy spectrum. The result is of the form

$$\sigma(W) = A^\circ \frac{\exp(-z^2/4)}{\Delta\sqrt{2\pi}} N(z). \quad (2.27)$$

Most previous measurements of Γ_{ee} have used the functional forms for $N(z)$ as obtained by Jackson and Scharre [13] or by Greco et al. [14], respectively:

$$\begin{aligned} N_{JS}(z) &= \left(\frac{2\Delta}{W}\right)^t \Gamma(1+t) D_{-t}(-z) + (\delta_v + \Pi) \exp(-z^2/4), \quad (a) \\ N_{GPS}(z) &= \left(\frac{2\Delta}{W}\right)^t \Gamma(1+t) D_{-t}(-z) \times (1 + \delta_v + \Pi). \quad (b) \end{aligned} \quad (2.28)$$

Here Γ denotes the gamma function and D_{-t} is Weber's parabolic cylinder function [18]. Note that in the limit $t \rightarrow 0$, $D_{-t}(-z) \rightarrow \exp(-z^2/4)$ and the Gaussian shape of the machine resolution is recovered.

In the above formulæ $\delta_v = \frac{3}{4}t + \frac{2\alpha}{\pi}(\frac{\pi^2}{3} - \frac{1}{2})$ stems from the vertex correction (fig. 2.5 d), where t is the equivalent radiator thickness. Π is the vacuum polarization correction from the diagram of fig. 2.5 b. It includes the effect of all the lepton and quark loops in 2.5 b: $\Pi = \delta_e + \delta_\mu + \delta_\tau + \delta_{quarks}$. The electron loop contributes $\delta_e \approx 0.014$ at energies W near the Υ resonances. Muon and tau loops are calculated with their corresponding masses [15]. The quark loop contributions have been estimated by Berends and Komen [19] from the measured $\sigma(e^+e^- \rightarrow hadrons)$ to be $\delta_{quarks} \approx 0.017$. Summing all fermion loop contributions yields

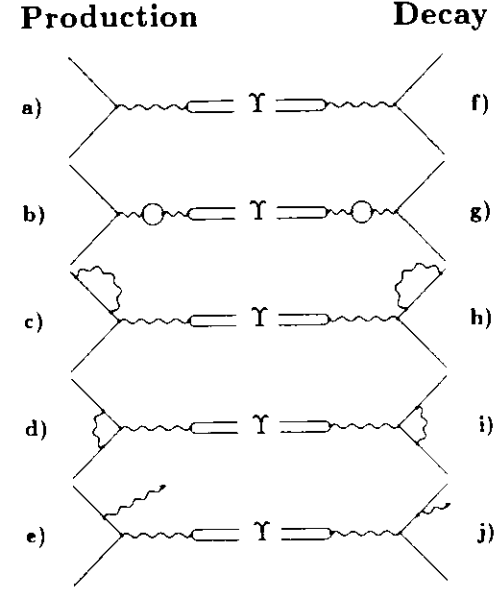


Figure 2.5: Feynman diagrams which contribute to $\mathcal{O}(\alpha^3)$ to $e^+e^- \rightarrow \Upsilon$ and $\Upsilon \rightarrow e^+e^-$. To this order the graphs b,c,d and g,h,i contribute only through their interference with the lowest order graphs a and f.

$\Pi \approx 0.038$ at our energy. In their original papers, Jackson and Scharre and Greco et al. ignored the μ , τ , and quark contributions. In eq. 2.28 we have corrected this by replacing δ_v by Π in their formulæ.

Both forms of $N(z)$ take into account the effect of the emission of many soft photons via "soft photon exponentiation", which leads to the $(2\Delta/W)^t$ factors in eq. 2.28. Jackson and Scharre apply it only to a part of the cross section, whereas Greco et al. correct the entire $\mathcal{O}(\alpha^3)$ expression. The difference is of $\mathcal{O}(\alpha^4)$, so that a definitive decision on which treatment is more accurate can only be made on the basis of a complete calculation to that order. Such a calculation has recently been done by Berends et al. [17], indicating good agreement with the form $N_{GPS}(z)$.

Thus $N_{GPS}(z)$ is suitable for use in connection with eq. 2.25 and 2.27 to measure $\Gamma_{ee}^\circ B_{had}$. However, we are interested in the physical Γ_{ee} , corresponding to a calculation to all orders in α . Γ_{ee} is defined as the partial width of the decay $\Upsilon \rightarrow e^+e^-$. In QED, $\Upsilon \rightarrow e^+e^-$ is always accompanied by an infinite number of low energy photons. To avoid specifying a photon energy cut-off in measurements of B_{ee} (or $B_{\mu\mu}$), it is conventional to include all decays with extra photons $\Upsilon \rightarrow e^+e^-n\gamma$ in the definition of Γ_{ee} . In order to relate Γ_{ee} to Γ_{ee}° , we assume that the $\mathcal{O}(\alpha^3)$ calculation is a good approximation to Γ_{ee} . The full set of diagrams

contributing to the decay to $\mathcal{O}(\alpha^3)$ is shown in fig. 2.5 f-j. Γ_{ee}^0 corresponds to the lowest order diagram 2.5 f only. By the Kinoshita-Lee-Nauenberg theorem [20], the mass singularities from the vertex correction and the bremsstrahlung graphs (i.e. the terms proportional to $\ln \frac{m}{m}$) cancel to each order in α , leaving a finite part which is negligible [15]. Thus the only radiative correction which makes a net $\mathcal{O}(\alpha^3)$ contribution to the decay comes from the vacuum polarization graph 2.5 g interfering with the lowest order graph 2.5 f. This leads to an increase of the partial width:

$$\Gamma_{ee} = (1 + \Pi) \Gamma_{ee}^0. \quad (2.29)$$

Lepton universality for Γ_{ii}^0 implies $\Gamma_{ee} \approx \Gamma_{\mu\mu} \approx \Gamma_{\tau\tau}$ to good approximation. Since $1 + \delta_v + \Pi = (1 + \delta_v)(1 + \Pi)$ to this order in α , we can remove the Π from $N(z)$ eq. 2.28 b and introduce $N'(z) = N(z)/(1 + \Pi)$. This yields

$$\sigma(W) = A \frac{\exp(-z^2/4)}{\Delta\sqrt{2\pi}} N'(z) \quad (2.30)$$

with

$$A = \frac{6\pi^2}{M^2} \Gamma_{ee} B_{had}. \quad (2.31)$$

More recent calculations of the radiative corrections use this convention. Tsai [15] and Kuraev and Fadin [16] find, respectively:

$$\begin{aligned} N'_T(z) &= \left(\frac{2\Delta}{W}\right)^T \Gamma(1+T) D_{-T}(-z) \times (1 - 1/2\Pi)^{-\delta_v/\Pi}, \quad (a) \\ N'_{KF}(z) &= \left(\frac{2\Delta}{W}\right)^t \Gamma(1+t) D_{-t}(-z) \times (1 + \delta_v). \quad (b) \end{aligned} \quad (2.32)$$

The $N'_{KF}(z)$ is exactly $N_{GPS}(z)$ with the Π removed. In the expression of Tsai $T = t_{ii}^2 \ln(\frac{z}{z-\Pi})$ is the equivalent radiator thickness corrected for pair production, which at $W = M_{T(1S)}$ differs from t by 0.32%. Some of the higher order corrections have also been calculated by Kuraev and Fadin, and differ from the renormalization group result of Tsai. However, the results agree to $\mathcal{O}(\alpha^3)$. The above formula for $N'_{KF}(z)$ omits the higher order terms.

Our results presented in section 5.1 are based on the formalism of Kuraev and Fadin [16], using eq. 2.30, 2.31, and 2.32 b to obtain $\Gamma_{ee} B_{had}$ directly. One could equally well use eq. 2.25, 2.27, and 2.28 b to obtain $\Gamma_{ee}^0 B_{had}$ and then apply eq. 2.29 to get $\Gamma_{ee} B_{had}$. However, most previous measurements have used the formalism of Jackson and Scharre with $\Pi = \delta_e$, resulting in something which is neither Γ_{ee} nor Γ_{ee}^0 . A comparison with the results obtained using the various formalisms is presented in section 5.2 to demonstrate the differences.

To obtain Γ_{ee} from $\Gamma_{ee} B_{had}$ we need the hadronic branching ratio B_{had} . With the assumption that the resonance only decays into hadrons and lepton pairs we can use the relation $B_{had} + 3B_{\mu\mu} = 1$. It is important to note that $B_{\mu\mu}$ is measured including all extra photons in the decay and contains the vacuum polarization term from graph g of fig. 2.5; otherwise the above equality would not hold. Also a determination of $\Gamma_{tot} = \Gamma_{ee}/B_{\mu\mu}$ requires the vacuum polarization term to be included in the leptonic width [21]. All above requirements are satisfied by the ansatz of Kuraev and Fadin [16], and this fact is the basis of the motivation of our choice.

3. Experimental Layout

The design of the Crystal Ball detector started in 1974. The detector went into operation at SPEAR at the end of 1978 taking data on the J/ψ and ψ' resonances. The operation at SPEAR ended in 1981. 4×10^6 hadronic events having recorded.

In the beginning of 1982 the Crystal Ball detector was moved to the DORIS-II e^+e^- storage ring to perform studies of the $b\bar{b}$ quarkonium. At DESY the Crystal Ball detector took data until summer 1986 with an accumulation of 1.5×10^6 hadronic events. The detector was shipped back to SLAC in September 1987.

The DORIS-II storage ring is described here only very briefly. Given details help in better understanding of the experimental problems that influence strongly our final results.

3.1 DORIS-II

The DORIS-II e^+e^- storage ring system at DESY is shown in fig. 3.1. Electrons are produced in hot filaments at the entries to the two linear accelerators. Electrons from the LINAC-II are directed onto a tungsten target to create positrons (a high Z target is needed due to the Z^2 -dependence of the cross section for pair production). The positron beam is accumulated in the small intermediate storage ring PIA (Positron Intensity Accumulator) to increase its intensity and cool down the beam.¹ Electrons from LINAC-I and positrons from PIA, accelerated up to about 450 MeV, are injected to the DESY synchrotron (Deutsches Elektronen SYNchrotron), which boosts their energy up to about 5 GeV. The electron and positron beams are then injected to the DORIS storage ring. DESY also serves as injector for the PETRA storage ring. The Crystal Ball and ARGUS detectors occupied the two interaction regions.

DORIS has been in operation since 1974. It was initially designed for a maximum beam energy of 3.5 GeV, with a double ring structure (DOppel RIng Speicher) and multibunch operation [22]. After the discovery of Υ resonances in 1978 DORIS was upgraded to reach the energy of the $\Upsilon(1S)$ and $\Upsilon(2S)$, namely 5.1 GeV per beam (DORIS-I storage ring) [23]. The two rings were combined into one ring, with single-bunch operation. The maximum luminosity (for the definition see Appendix B) was only $1 \times 10^{30} \text{ cm}^{-2} \text{ sec}^{-1}$ with high power consumption of 10.8 MW at 5.1 GeV. DORIS was upgraded again in 1982 [24]. The bending power of the magnets was increased allowing a maximal energy of 5.6 GeV. Several improvements brought the power consumption down to half of that of DORIS-I. High luminosity $\mathcal{L} > 10^{31} \text{ cm}^{-2} \text{ sec}^{-1}$

¹As synchrotron radiation occurs the beam momentum spread becomes smaller. In analogy to thermodynamics this process is called cooling.

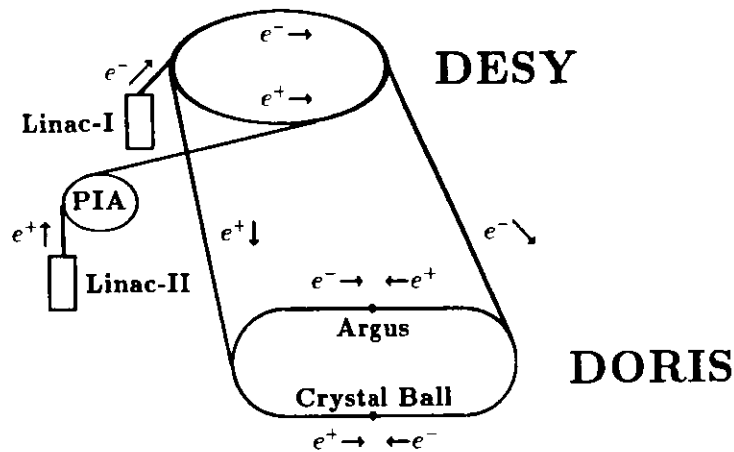


Figure 3.1: DORIS-II e^+e^- storage ring at DESY.

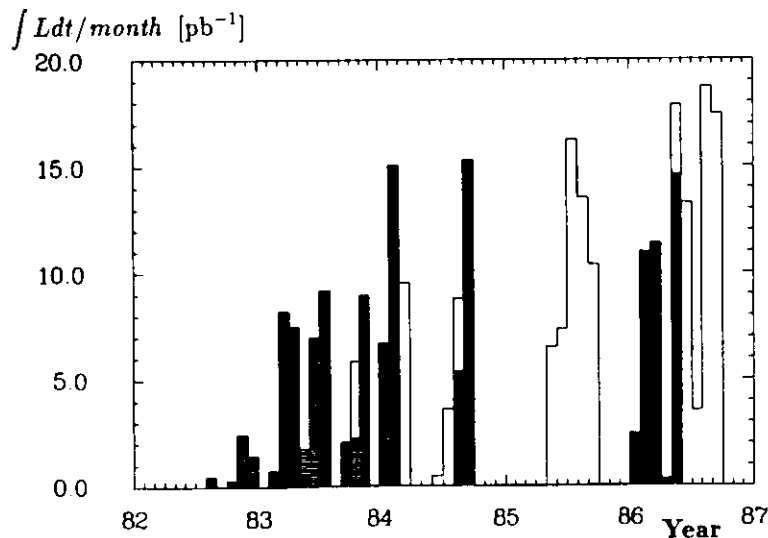


Figure 3.2: The integrated luminosity collected by the Crystal Ball detector at DORIS-II. The doubly hatched area represents the data taken around $\Upsilon(1S)$, hatched area $\Upsilon(2S)$ and hollow $\Upsilon(4S)$ data, respectively.

around a 5 GeV region was obtained by the installation of mini-beta quadrupoles close to the interaction region². Mini-beta quadrupoles improve beam focussing at the interaction points (see eq. B.2). The vacuum system of DORIS-II gives an average pressure of $2-8 \times 10^{-9}$ mbar depending on the beam current. Typical operation involves beams with lifetimes of 2-3 h, injected with currents of $2 > 30$ mA, resulting in an integrated luminosity delivered by the machine of roughly 600 nb^{-1} per day. A record accumulation of more than 1000 nb^{-1} per day was achieved. Figure 3.2 shows integrated luminosity per month accumulated for different resonances.

The longitudinal size of the electron (positron) bunches causes a spread of the interaction point along the beam axis. The spread is approximately Gaussian with σ of about 1.7 cm. The corresponding spread in the plane transverse to the beam axis is much smaller (high luminosity requirement) i.e. ~ 1 mm vertically and ~ 0.1 mm horizontally.

Electrons and positrons in the DORIS-II storage ring become polarized as a result of emission of synchrotron radiation according to the Sokolov-Ternov effect [25]. The beam energy measurement by depolarization techniques is the most precise one. The accurate measurement of the beam energy is crucial for the determination of Γ_{ee} and resonance masses. The polarization direction is parallel to the magnetic field of bending magnets, thus transverse to the beam direction. The maximum achievable polarization due to this mechanism is $\sim 92\%$. Beam polarization is limited by the synchrotron radiation itself. Sudden energy loss by photon emission causes a change of the particle orbit, which destroys the correlation between orbital and spin motion. Also, unavoidable vertical misalignment of the storage ring components causes beam particles to be influenced by the depolarizing radial field of the quadrupoles. Similarly, beam-beam forces at the interaction point cause depolarization. Finally, the solenoid field of the ARGUS magnet, which is only partially compensated (87%), acts to destroy the polarization. As a result of these depolarization effects, the beam polarization does not reach the theoretical limit. At certain beam energies, where depolarizing machine resonances occur, the beam polarization can be destroyed completely. Theoretical calculations for DORIS-II have shown that beam polarization at the $\Upsilon(2S)$ energy may be rather high. In fact, we measured an average beam polarization of $(78 \pm 7)\%$ for the $\Upsilon(2S)$ data using the process $e^+e^- \rightarrow \mu^+\mu^-$ [26].

3.2 The Crystal Ball Detector

The Crystal Ball detector [27] is a non-magnetic calorimeter designed to measure precisely the energies and directions of electromagnetically interacting particles. We describe here only those features that are important for the data selection. The experimental setup is shown

²The installation of the mini-beta magnets had a serious drawback. The endcaps as they were designed for SPEAR no longer fit because of space limitations. The Crystal Ball endcaps have been completely redesigned for DORIS-II but the fine granularity of this detector part was lost.

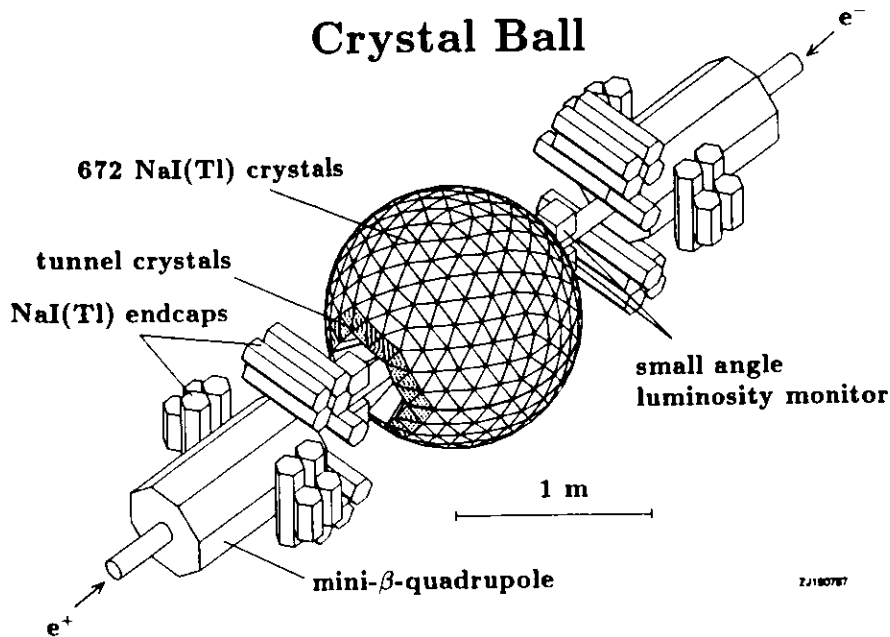


Figure 3.3: View of the Crystal Ball detector (as installed at DORIS-II)

in fig. 3.3. The main detector is a spherical shell of 672 optically isolated NaI(Tl) crystals covering 93% of the total solid angle. The remaining 7% are left free to allow room for the beam pipe. Each crystal, of truncated pyramidal shape, is ~ 15.7 radiation lengths deep (corresponding to about 1 nuclear interaction length), points to the interaction point and is read out by its own photomultiplier (see fig. 3.4). The 60 crystals immediately surrounding the beam pipe are called “tunnel crystals”. They cover the angular region of approximately $0.85 < |\cos\theta| < 0.93$, where θ is the angle with respect to the beam axis. NaI(Tl) endcaps increase the angular coverage to 98% of 4π , but are not used in this analysis.

The measured energy resolution for electromagnetically showering particles is $\sigma_E/E = (2.7 \pm 0.2)\% / \sqrt{E/\text{GeV}}$. The NaI(Tl) energy scale is set for each $\sim 3 \text{ pb}^{-1}$ of accumulated luminosity using large angle Bhabha scattering events. Minimum-ionizing particles deposit about 210 MeV. Approximately two thirds of the hadrons are expected to undergo nuclear interactions while traversing the NaI(Tl); the rest are minimum-ionizing if charged. The directions of electromagnetically showering particles are measured in the NaI(Tl) to an accuracy of $\sigma_\theta = 1^\circ$ to 2° , depending on their energy. For minimum-ionizing particles we have $\sigma_\theta \sim 3^\circ$. One can improve the angular resolution by use of the proportional tube chambers, which directly surround the beam pipe (see fig. 3.5). The shape of the chambers is dictated

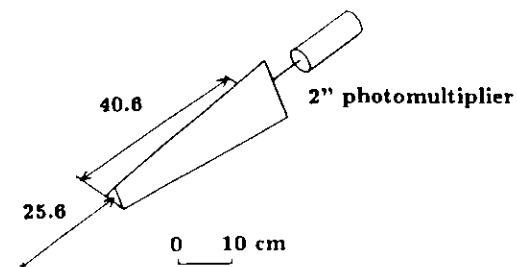


Figure 3.4: The size and shape of a single crystal. The interaction point is marked by a cross. The distances are given in centimeters.

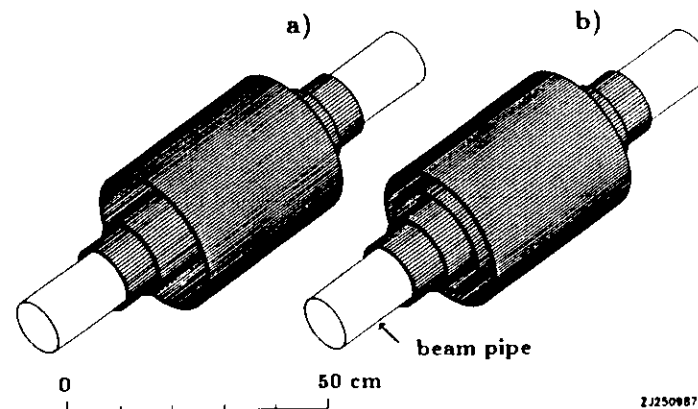


Figure 3.5: Tube chambers setup: a) 3 layers b) 4 layers. The Monte Carlo geometry was used to produce this drawing.

by the limited space between the beam pipe and the spherical inner detector shell. The configuration of this part of the apparatus depends on the data-taking period. Initially, it was a three double-layered setup flushed with magic gas (i.e. working in the streamer mode), which were later partially replaced by tubes flushed with $\text{Ar} + \text{CO}_2 + \text{CH}_4$ working in proportional mode (design as shown in fig. 3.5 a). Eventually, it was upgraded to four double-layers as shown in fig. 3.5 b. For our purposes we find it sufficient to use only the direction information deduced from the energy deposition in the crystals. Because this analysis spans various data taking periods, it was difficult to formulate common hadronic-event-selection-criteria for all chamber setups—thus the chamber information was not used in this analysis.

To measure Bhabha scattering $e^+e^-(\gamma) \rightarrow e^+e^-$ at small angles there are 4 shower counters located at $\theta \sim 8^\circ$ —see fig. 3.3. The method of the luminosity determination is discussed in detail in Appendix B.

3.3 Organization of the Data Acquisition

The interesting e^+e^- interactions have to be separated from a large background. We discuss here shortly the trigger design and our data quality monitoring system. A simple, stable in time trigger, and supported by a well designed data monitoring system, enabled us to reduce the systematic errors. The scheme of the Crystal Ball data acquisition system is shown in fig. 3.6. The signals from apparatus components after preamplification are carried to the electronics in the control room. The analog signals are stored temporarily on the capacitors inside so-called "I&H" (Integrate and Hold) modules. The various trigger conditions select the interesting class of events by simple "hard wired" criteria consisting mainly of the topology of the energy depositions and/or energy thresholds in the main ball within a 300 ns bunch crossing gate delivered by the DORIS control. The rate of the events to be registered ranges from kHz down to a few Hz. The data used in this analysis satisfy our total energy trigger which is fully efficient for events depositing at least 1.9 GeV in the NaI(Tl) crystals which lie within $|\cos\theta| < 0.85$. Our selected hadronic events (see section 4) have a minimum total energy of ~ 2.1 GeV. Fulfillment of any trigger condition freezes the information inside the I&H modules and starts the readout. Up to this moment we have dealt with analog information. The analog information is digitized sequentially by two ADC's and afterwards sent via CAMAC to a PDP-11. This process is controlled by a special processor called NEMO [28]. Collected data are stored on the 300 MB PDP-11 disc and sent to the DESY IBM via a link where they are stored on the disc buffer. Both discs are used as circular buffers. When the buffer at the IBM is 2/3 full a special job automatically starts (DUMP job) that copies the contents of the IBM disc to tape. Together with the DUMP job, selection and production jobs are initiated so that the preliminary data are immediately available for the analysis. More extensive checks of the data quality were done on the IBM.

The apparatus performance is monitored online by special programs. This routine check-up includes:

- linearity control of the energy readout system;
- temperature, crate voltages, humidity and pressure inside dry house, DORIS vacuum, beam currents etc. (Monitor ONLINE records that will be used in a section devoted to the background determination belong to this class);
- trigger logic.

This information is stored together with the data as special data records, so that it can be used afterwards to pinpoint the problems in the apparatus.

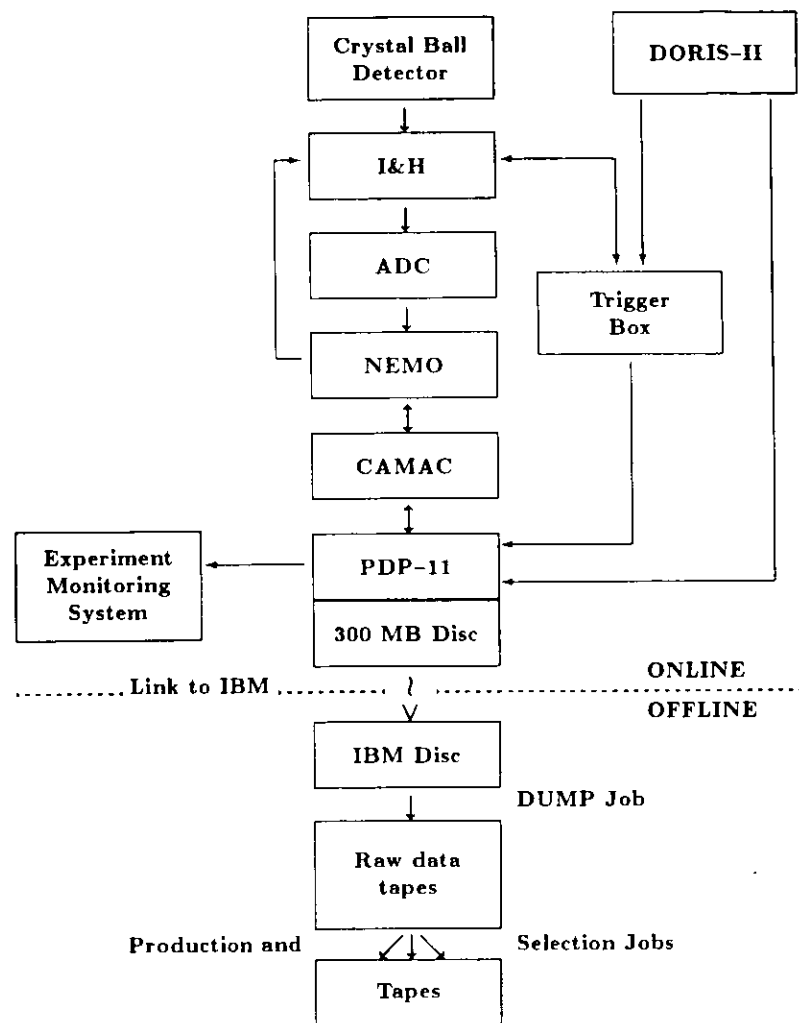


Figure 3.6: Organization of the data acquisition system.

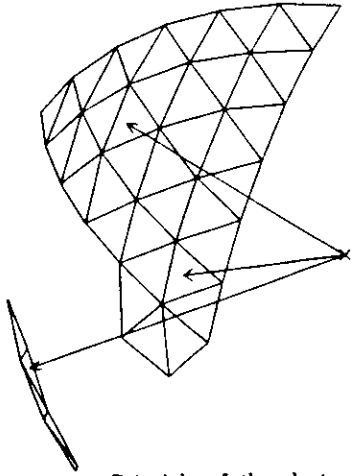


Figure 3.7: Principle of the cluster algorithm. Particles created at the interaction point (marked by a cross) enter the ball depositing energy in crystals (visible triangles). The illuminated crystals cluster around the direction of the incident particle. The clusters created by two particles can merge into a single one.

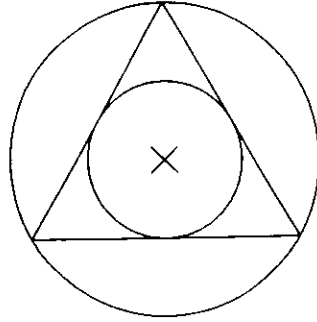


Figure 3.8: The geometry which determines angular resolution of the Crystal Ball calorimeter. The triangle represents a small crystal facet. The small circle corresponds to $\pm 3^\circ$, the large to $\pm 6^\circ$. The area ratio of the crystal surface and the inscribed circle is about 0.8 thus compatible with one standard deviation level (see text).

3.4 Interpretation of the Energy Deposited in the Crystals

Particles created at the interaction point traverse the chambers and enter the ball. The raw data then contain the information about the energy deposited in the NaI(Tl) crystals and the chamber hits. Our aim is to measure energy and momenta of created particles. Since the Crystal Ball is a non-magnetic detector we approximate momentum \vec{p} of a particle by its measured energy E :

$$\vec{p} = E \hat{n} \quad (3.1)$$

where \hat{n} is a unit vector representing the direction of the particle. The choice of E and \hat{n} is not unique. In the following we will try to discuss some of the possibilities. In the first step of data reconstruction crystals are grouped into clusters. The cluster is defined as a group of adjacent crystals each having at least 10 MeV deposited energy (see fig. 3.7). As the next step inside the clusters local maxima are found. The third step correlates the hits inside the chambers with the energy deposited in the ball. For the purpose of this analysis

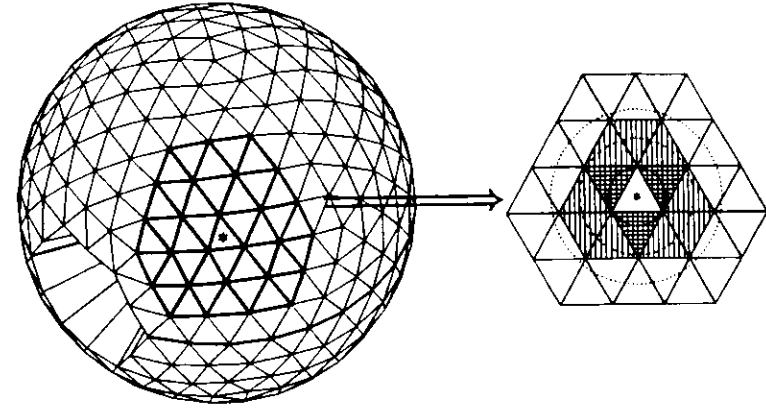


Figure 3.9: Direction reconstruction for electromagnetically showering particles. The electromagnetically showering particle hits the ball. The energy is deposited in a cluster of crystals with a visible maximum (marked by asterisk). For circles see text.

we will discuss the first two steps of the data reconstruction wherein no chamber information has been used.

The short edge of the crystal covers 12° . This implies that, using only the information from the crystals, we are able to reconstruct the directions of incident particles with a precision of at least $\pm 6^\circ$; in practice it is reconstructed two times more precisely, i.e. $\pm 3^\circ$, by assuming that the probability of hitting a particular point is constant over a crystal surface (see fig. 3.8).

For the electromagnetically showering particles (e^+ , e^- , γ) the lateral energy distribution is well-determined by the Monte Carlo studies. The characteristic energy pattern can be used for selecting e , γ and for getting their directions with better precision than determined by the geometric calorimeter resolution alone. The idea of the showering track reconstruction technique is shown in fig. 3.9. The deposited energy is shared among a symmetric group of 13 neighboring crystals. On average a photon, hitting the central crystal along its axis, deposits 70% of its energy in one crystal with $\sim 2\%$ outside the group of 13 neighboring crystals. This can be understood since the crystal size was chosen such that the circumscribed circle has a radius of one Molière unit. Sometimes more particles enter the same cluster, for example, a decay of a fast π^0 (energy $E_\pi \gtrsim 500$ MeV) into photons creates such a situation. Of course, there is a probability that shower fluctuation can create a second local maximum. The criteria allowing discrimination between local maxima of the energy deposition and shower energy fluctuations are also well defined and can be found by Monte Carlo studies (for details see [26]). As the first approximation for the direction of electromagnetically showering particles we use a local energy maximum within the cluster (direction \hat{n} is then

found as the crystal axis of the crystal with maximum energy deposition). This direction is then corrected using the known lateral shower distribution. The energy contained in 13 neighboring crystals serves as a reliable energy estimate for these particles.

In case of hadronically interacting particles we do not have such a straightforward direction and energy definition. The discrimination function is not known; it depends on the type of the showering particle. There are basically two methods that can be used to estimate the energy and direction for showering hadrons. In the first method we use the crystal energy and crystal axis, i.e. we assume that every illuminated crystal was hit by a particle carrying energy equal to deposited energy and in the direction of the crystal axis. This is physically equivalent to the replacement of incident particles by a beam of particles. Experience shows that such an approximation works well. The other possibility is to use energy clusters and correlate them directly to particles. The energy E is then the total energy of the cluster (referred to afterwards as $E_{cluster}$) while the direction might be estimated as the energy-weighted average of the crystal axis \hat{n}_i , involved in the cluster:

$$\hat{n} = \frac{\sum_{cluster} E_i \hat{n}_i}{E_{cluster}}. \quad (3.2)$$

As will be discussed later, experience shows that the first method carries information not only about the created particles but also about their interactions in the calorimeter.

4. Selection of Hadronic Events

The subtle effects we would like to measure require high experimental accuracy. We are primarily interested in suppressing the systematic error. The detailed analysis of our aim, i.e. the measurement of R and the determination of Γ_{ee} , shows that the systematic errors of the final results will be fully dominated by the errors on: i) the selection efficiency, ii) the background subtraction, and iii) the luminosity determination. Good design of the cuts for data selection can reduce the first two contributions. For the determination of Γ_{ee} and R we have to select the hadronic events originating from $e^+e^- \rightarrow q\bar{q}$ and/or $e^+e^- \rightarrow 3g$ alone. As background we have to consider both, the hadronic events coming from the other processes and misidentified non-hadronic events. Background events originate from: 1) QED processes, 2) two photon interactions, and 3) collisions of beam particles with residual gas and the vacuum beam pipe. Since 1978 the selection of the hadronic events was a subject of a continuous development. We start with the motivation for the experimental cuts. In the following sections we will discuss the efficiency resulting from our selection criteria and give the estimate of accepted backgrounds.

4.1 Selection Criteria

There are two extreme different approaches to the data selection problem. The first way is to select the interesting events without loss of efficiency by accepting a rather high background. This method is applicable when we are not dependent on the absolute normalization or when the background source is known theoretically and/or we are able to subtract it without increasing the systematic errors. A typical example for application of this method is searching for P -states in the inclusive hadronic spectra where the background is subtracted afterwards with help of a polynomial fit. The second method of approaching the selection problem is to lose some selection efficiency (in a manner which could be checked by Monte Carlo calculation) by suppressing background of unknown origin as much as possible. Both methods were used in the Crystal Ball Collaboration to select hadronic events. A selection program using the first philosophy was written at SLAC by W. Lockman [29] (referred to from now on as the "BILL" selector). Quiet running conditions at SPEAR allow for loose selection criteria. The other independent selection program was written at DESY by H.J. Trost (referred to as "HAJO" selector). The reason was that the running conditions at DORIS were completely different, for instance the beam-gas background was significantly higher. The quick scan through the background processes shows that there is a substantial background arising from $\gamma\gamma$ interactions. As it will be shown later the cross sections for

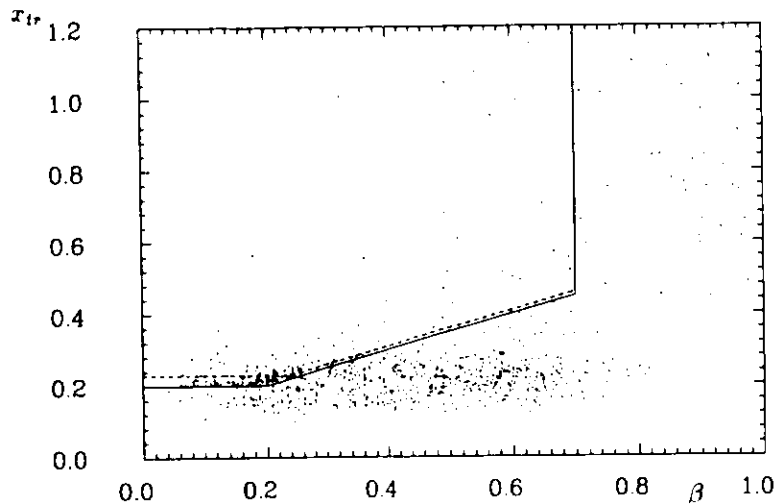


Figure 4.2: Single beam data passing the BILL selector on (β, x_{tr}) plane. The continuous line shows the HAJO original cut, the broken one the suggested modification.

rest frame. The relatively high acceptance of $\tau^+\tau^-$ events for hadronic selection criteria can be understood as a result of τ leptons having relatively large hadronic branching ratios. Events with both τ 's decaying hadronically will have a two jet topology, indistinguishable from the hadron production in the continuum. The low acceptance for the hadrons produced in two photon collisions can be explained by their low transverse momentum with respect to the beam axis. The high transverse momentum cut suppresses this class of events almost completely. This is shown in figs. 4.10 and 4.11, where we show the correlation discussed earlier for $e^+e^-(\gamma) \rightarrow \tau^+\tau^-$ and two-photon hadronic Monte Carlo events.

Cut 1 and 6 were designed to suppress QED and cosmic type events. Cut 1 is a moderately weak cut on multiplicity. Cut 6 from this group turned out to be 100% correlated with the other cuts and thus was not used.

Cuts 7 and 8 are designed to further suppress Bhabha events. Fig. 4.12 shows the distribution of the visible energy for unselected Bhabha Monte Carlo events while fig. 4.13 gives the same events on the (β, x_{tr}) plane. The large number of produced Bhabha events although not rejected by our main selection cut (cut 4), is rejected by the combination of a typical high energy deposition correlated with low multiplicity. To reduce further the background from the Bhabha events and achieve agreement between this cut and the requirements for Bhabha candidates, the threshold on cluster energy was lowered to $E_{cluster} > 0.35W$. Fig. 4.14 shows the correlation between visible energy deposited in the ball and cluster energy for Bhabha Monte Carlo events. The strong correlation (indicated by the arrow) occurs when we have measured only one electron and thus $E_{Ball} = E_{cluster}$. For comparison the same correlation for $\Upsilon(1S) \rightarrow 3g$ Monte Carlo is shown in fig. 4.15.

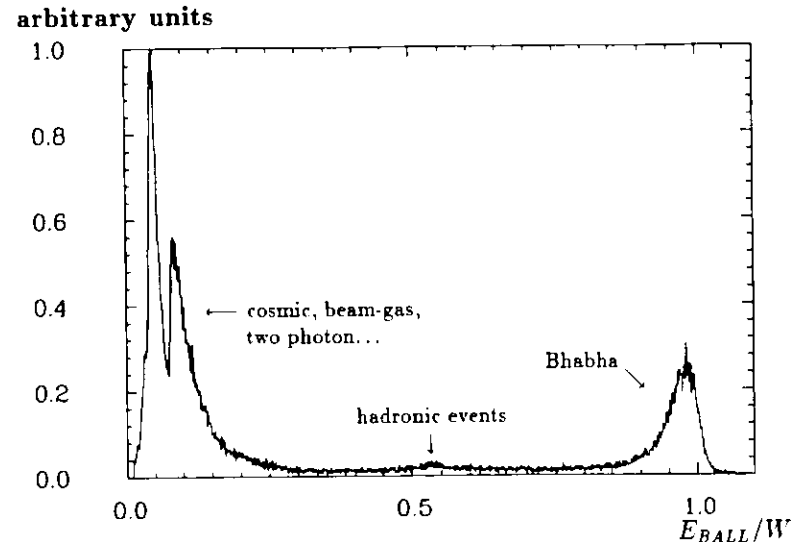


Figure 4.3: Visible energy distribution for the raw data. The doubly-peaked structure at the low energy end of the spectrum reflects our trigger setting.

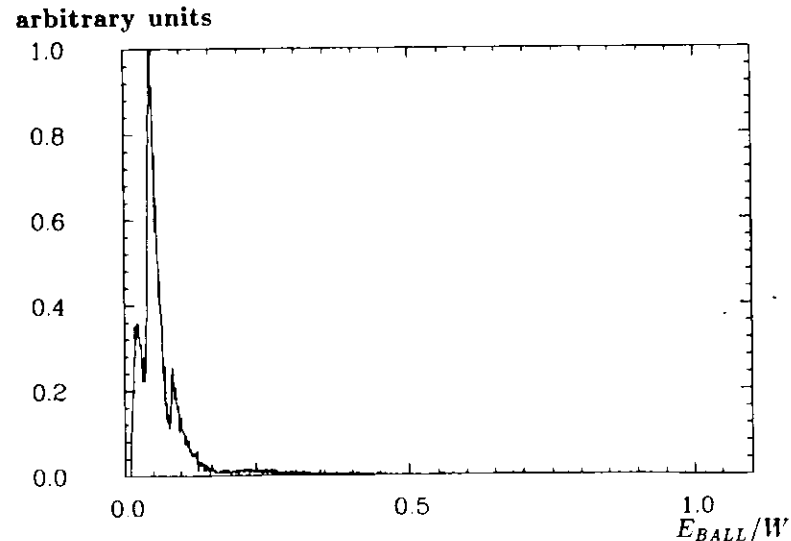


Figure 4.4: Visible energy distribution for the single beam data.

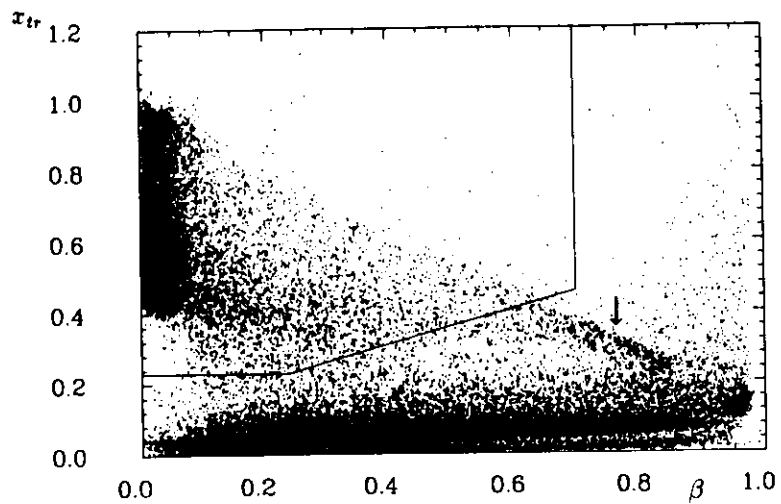


Figure 4.5: (β, x_{tr}) plane for unselected data. The accepted events are in the upper left corner, separated from the rejected events by the solid line. For the arrow see text.

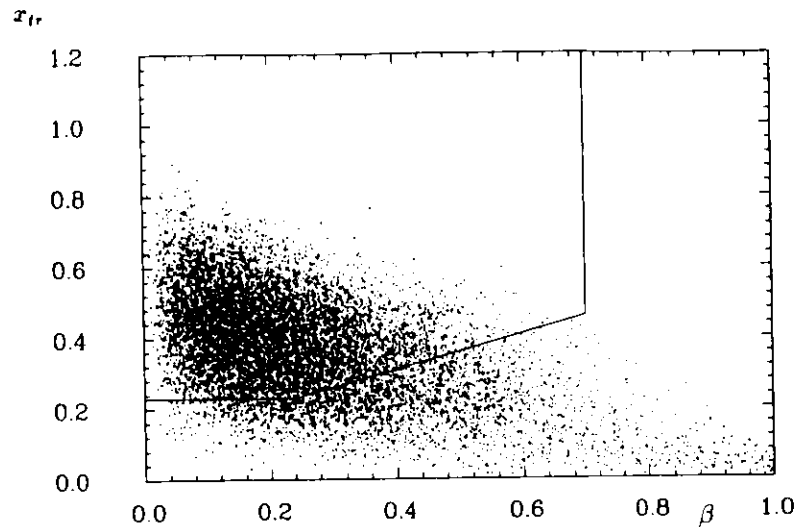


Figure 4.7: (β, x_{tr}) plane for unselected $e^+e^- \rightarrow q\bar{q}$ Monte Carlo events.

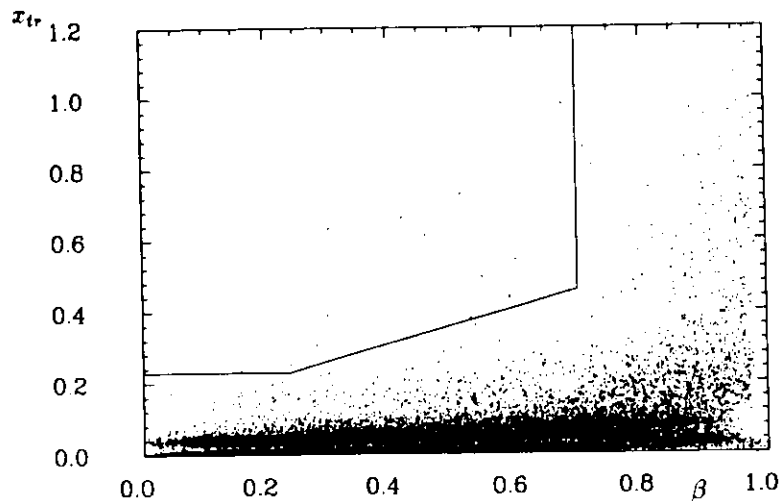


Figure 4.6: (β, x_{tr}) plane for unselected single beam data.

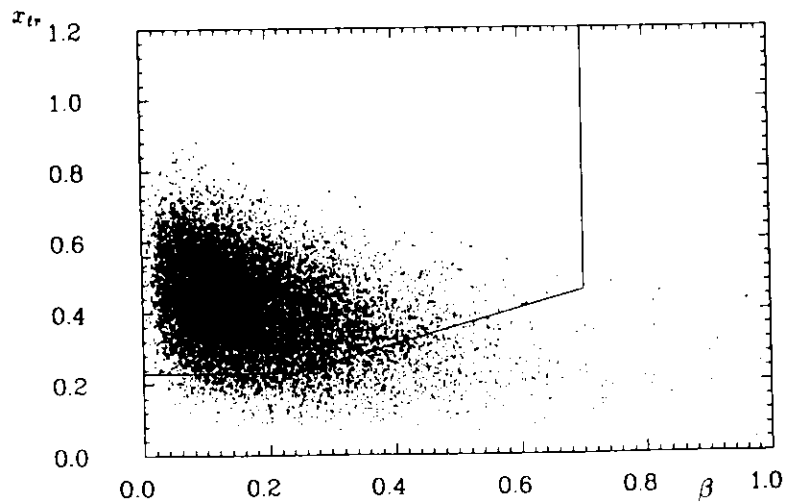


Figure 4.8: (β, x_{tr}) plane for unselected $Y(1S) \rightarrow 3g$ Monte Carlo events.

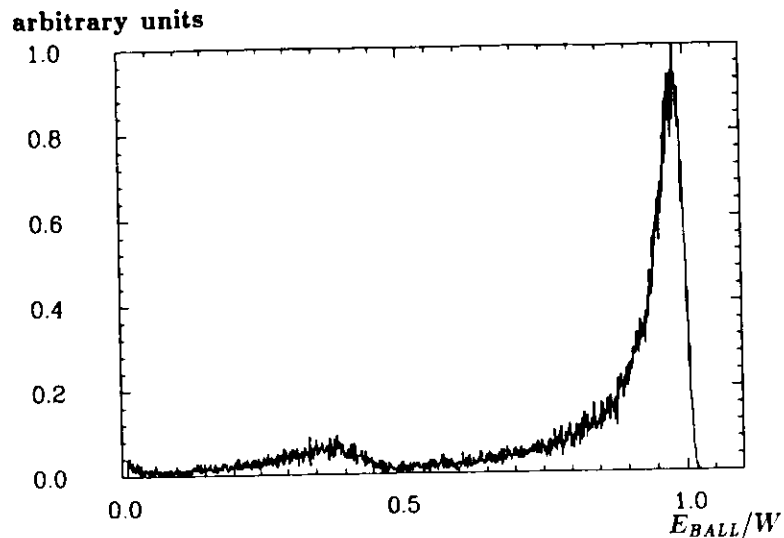


Figure 4.12: The distribution of the visible energy for unselected Bhabha Monte Carlo events.

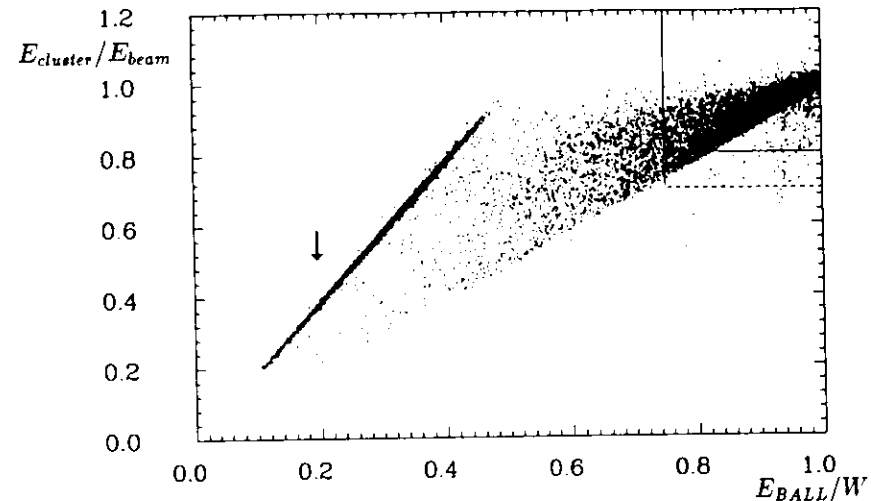


Figure 4.14: Bhabha Monte Carlo events. The dotted line shows the original cut, the continuous one show the modification suggested (see text).

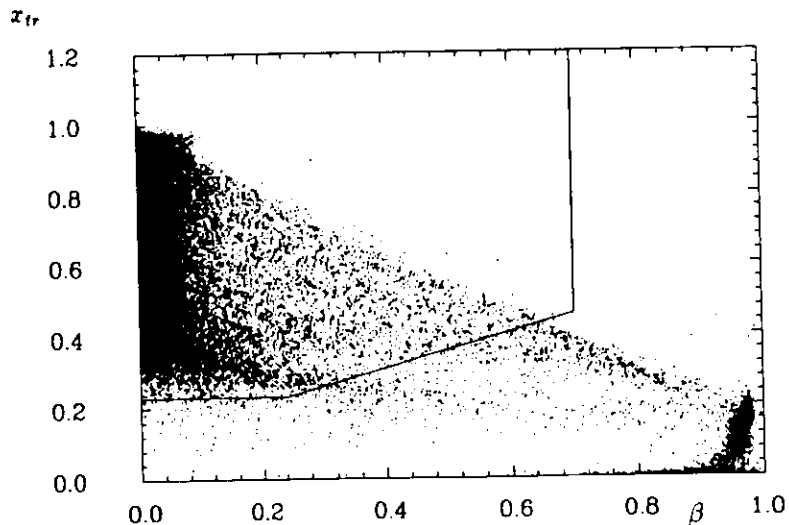


Figure 4.13: (β, x_{tr}) plane for mixture of unselected Monte Carlo Bhabha and $e^+e^- \rightarrow \gamma\gamma$ events.

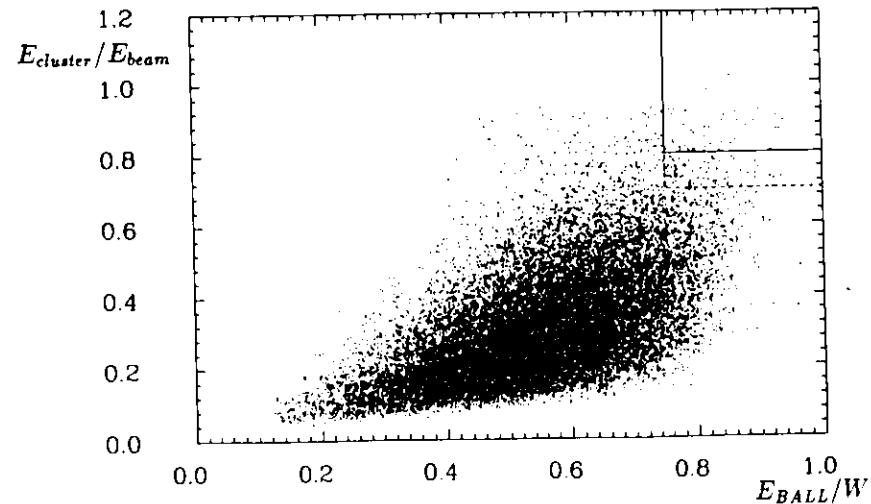


Figure 4.15: $\Upsilon(1S) \rightarrow 3g$ Monte Carlo events. The dotted line shows the original cut, the continuous one suggested modification.

Let us summarize our final selection criteria:

- i. $0.2W \leq E_{Ball} \leq 1.2W$;
- ii. $E_{tunnels}/E_{Ball} < 0.5$;
- iii. $x_{tr} > 0.23$, $\beta < 0.7$ and $x_{tr} > 0.5\beta + 0.11$;
- iv. there should be at least 3 energy clusters with an energy $E_{cluster} > 100$ MeV each;
- v. events should not have more than one energy cluster with $E_{cluster} > 0.35W$;
- vi. events should not have any energy cluster with $E_{cluster} > 0.35W$ if $E_{Ball} > 0.75W$.

The selection presented above allows us to select a relatively background free hadronic data sample using a minimal number of well-tuned cuts. The conversion of the number of observed hadronic events into the number of produced hadronic events still requires determination of our selection efficiency and estimation of the background remaining in our hadronic data sample.

4.2 Efficiency Determination

The detection efficiencies for hadronic events from $\Upsilon(1S)$ and $\Upsilon(2S)$ decays, continuum $q\bar{q}$ production events and background events are calculated using the Monte Carlo technique. Hadronic events from $\Upsilon(1S)$ and $\Upsilon(2S)$ decays and from continuum $q\bar{q}$ production are generated with the standard LUND string fragmentation program version 6.2 [30]. As an alternative hadronization scheme we use the coherent parton shower model offered in the same program. This scheme is based on the QCD cascade model by Marchesini and Webber [31], and has only been implemented for $q\bar{q}$ states, not for 3 gluon states. In sections 5.1 and 6 we estimate our sensitivity to the hadronization scheme from the difference in the efficiency for $e^+e^- \rightarrow q\bar{q}$ obtained with the two models.

The generated events are passed through a complete detector simulation. This simulation includes the following steps:

1. Electromagnetically interacting particles are handled by the electromagnetic shower development program EGS [32].
2. The interactions of hadrons are simulated with the GHEISHA 6 program [33]. To achieve a reasonable description of the experimental data we have modified the original GHEISHA program as discussed in appendix A.
3. Extra energy deposited in the crystals by beam-related background is taken into account by adding special background events to the Monte Carlo events. These background events are obtained by triggering on every 10⁷th beam crossing, with no other condition.

Table 4.2: Summary of various hadronic detection efficiencies. The errors are the Monte Carlo statistical errors only. Superscripts R denote resonance efficiencies; C , continuum efficiencies.

efficiency symbol	Process	W [GeV]	ϵ [%]	Comments
$\Upsilon(1S)$				
ϵ_{3g}^R	$\Upsilon(1S) \rightarrow 3g, \gamma g g$	9.46	91.0 ± 0.1	LUND string
$\epsilon_{q\bar{q}}^R$	$\Upsilon(1S) \rightarrow q\bar{q}$	9.46	78.9 ± 0.4	LUND string
$\epsilon_{\tau^+\tau^-}^R$	$\Upsilon(1S) \rightarrow \tau^+\tau^-$	9.46	15.8 ± 0.5	
ϵ_H^R	$\Upsilon(1S) \rightarrow hadrons$	9.46	83.1 ± 0.1	
$\Upsilon(2S)$				
ϵ_H^R	$\Upsilon(2S) \rightarrow hadrons$	10.02	85.4 ± 0.2	80% beam pol.
Continuum				
$\epsilon_{q\bar{q}}^C$	$e^+e^- \rightarrow q\bar{q}$	9.39	72.7 ± 0.2	LUND string
$\epsilon_{q\bar{q}}^C$	$e^+e^- \rightarrow q\bar{q}$	9.39	71.3 ± 0.2	coherent shower

4. The events are then reconstructed using our standard software and subjected to the same cuts as the data.

The efficiency calculations are described in more detail in sections 4.3, 5.1, and 6. For completeness we give the expression for calculating the efficiency of the process $\Upsilon \rightarrow hadrons$

$$\epsilon_H^R = \epsilon_{3g}^R \{1 - (R + 3) B_{\mu\mu}\} + \epsilon_{q\bar{q}}^R R B_{\mu\mu} + \epsilon_{\tau\tau}^R B_{\mu\mu} \quad (4.1)$$

where $\ell\bar{\ell}$ are e^+e^- , $\mu^+\mu^-$ and $\tau^+\tau^-$. Table 4.2 summarizes our hadronic efficiencies. The typical Monte Carlo sample consists of 50k events.

4.3 Background

The estimates of the background magnitudes are obtained with use of Monte Carlo techniques and single beam data. The specific method used depends on the origin of the background events as will now be discussed. The resulting background estimates will be used in sections 5.1 and 6 in the determination of Γ_{tr} and R , respectively, and in the estimate of the systematic error.

4.3.1 QED Processes

To estimate the background from the QED processes $e^+e^- \rightarrow e^+e^-(\gamma)$, $\gamma\gamma(\gamma)$, $\mu^+\mu^-(\gamma)$, and $e^+e^- \rightarrow \tau\bar{\tau}(\gamma)$ from the continuum, we generate events of these types with the programs of refs. [34] and [35]. The symbol (γ) indicates that photon emission and other QED processes to $\mathcal{O}(\alpha^3)$ are included. The production cross sections and their products with the efficiencies

Table 4.3: Summary of Monte Carlo generated continuum QED and two photon cross sections σ and observed cross sections $\epsilon\sigma$. The errors in $\epsilon\sigma$ originate from Monte Carlo statistics.

Process	W [GeV]	σ [nb]	$\epsilon\sigma$ [pb]
$e^+e^- \rightarrow e^+e^-(\gamma)$	9.39	103.9	14.6 ± 4.1
$e^+e^- \rightarrow \gamma\gamma(\gamma)$	9.39	31.3	1.3 ± 0.3
$e^+e^- \rightarrow \mu^+\mu^-(\gamma)$	9.39	1.4	< 1
$e^+e^- \rightarrow \tau^+\tau^-(\gamma)$	9.39	1.1	171.3 ± 4.3
$\gamma\gamma \rightarrow \text{hadrons}$	9.39	7.1	19.8 ± 5.6

to pass our hadronic selection cuts, determined as described in section 4.2, are presented in table 4.3. The largest source of background, as can be expected, is the $e^+e^- \rightarrow \tau\bar{\tau}(\gamma)$ channel because the events with both τ 's decaying hadronically are physically indistinguishable from the continuum 2-jet hadron production. The values of $\sigma\epsilon$ listed in table 4.3 are to be compared to $\sigma\epsilon \sim 3000$ pb for $e^+e^- \rightarrow \text{hadrons}$ at $W = 9.46$ GeV.

4.3.2 Two-Photon Collisions

According to ref. [36] a good description of the total cross section data of the process $\gamma\gamma \rightarrow \text{hadrons}$ is obtained by adding the predictions of the Generalized Vector-Meson Dominance Model (GVDM) and the Quark Parton Model (QPM). The appropriate lowest order Feynman diagrams for these processes are shown in fig. 4.16. Since we expect only small background contributions from two photon interactions we follow the procedure suggested by ref. [36]. For the QPM part we generate $q\bar{q}$ pairs with a Monte Carlo program following ref. [37] with subsequent hadronization by the standard LUND program version 6.2 [30]. The cross section at given c.m.s. energy W and quark composition was generated according to

$$\sigma(W) = 3 \sum_{i=u,d,s,c} \sigma_i(W, m_i) q_i^4 \quad (4.2)$$

where σ_i are the partial cross sections and q_i denote the charges for a given quark flavor. The quark masses m_i are those used in the LUND fragmentation scheme. Eq. 4.2 stems from the diagram in fig. 4.16a and is valid only to this order. Two photon events with a GVDM cross section, parametrized according to ref. [36] as

$$\sigma_{\text{tot}}(\gamma\gamma \rightarrow \text{hadrons}) = [(240 \pm 29) + (394 \pm 110)\text{GeV}/W_{\gamma\gamma}] \text{nb} \quad (4.3)$$

are generated by a Monte Carlo program using the Equivalent Photon Approximation [38]. The sum of the generated QPM and GVDM cross sections and the resulting visible cross section are presented in table 4.3. The small acceptance for this class of hadronic events is fully understandable. Our main selection cut is the cut on τ_{tr} —we reject events with small $p_{T\tau}$; such restricted $p_{T\tau}$ range is one of the most characteristic features of events originating

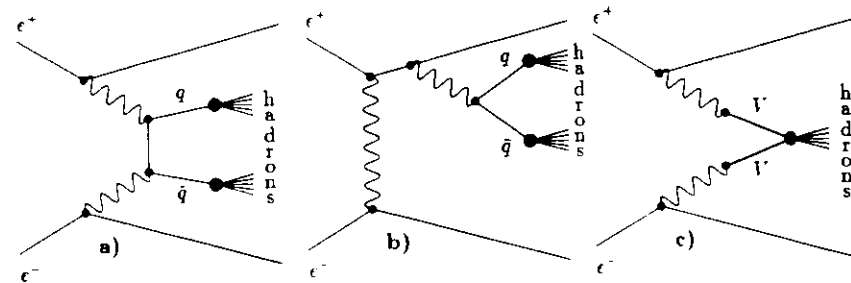


Figure 4.16: The lowest order Feynman diagrams leading to hadron production in $\gamma\gamma$ interaction: a) and b) pointlike interaction (graph (a) is dominating (b)), c) VDM mechanism.

from two photon interactions. The above method to estimate the two-photon contribution to the total cross section is very crude: for example the QCD corrections to graphs a) and b) in fig. 4.16 might be very large [36]. Therefore we set a 100% systematic error on the two-photon contribution to the total hadronic cross section.

4.3.3 Beam-gas Background

Events from collisions of beam particles with residual gas or with the vacuum pipe can be misidentified as hadronic by the selection procedure. They are referred to as “beam-gas” events. The contamination from beam-gas events in our hadronic sample is determined from single-beam runs taken close in time to our energy scans. We assume that all of the single-beam data are beam-gas events. The following quantities may serve (for normalization purposes) for the ratio of the time spent with single or separated-beam running conditions compared to that with colliding beams:

1. $\int Idt$ —current integral, to account for the beam lifetimes.
2. $\int pIdt$ —current-pressure product integral. This method accounts not only for beam lifetimes but also for different vacuum conditions. Intuitively the beam-gas collision rate should be proportional to the gas density, i.e. to the pressure read in the vacuum monitors.
3. The actual data—the idea is to subtract the theoretical predictions from data.

The differences between background estimates obtained using these quantities will serve as the measure of the systematic effects.

The number of beam-gas events in the colliding beam sample is calculated in two independent ways. In the first approach we normalize the single-beam data to the colliding-beam data by integrating the product of the total beam current and the gas pressure (or current only) over the running time. This method is model-independent, but sensitive to any difference in

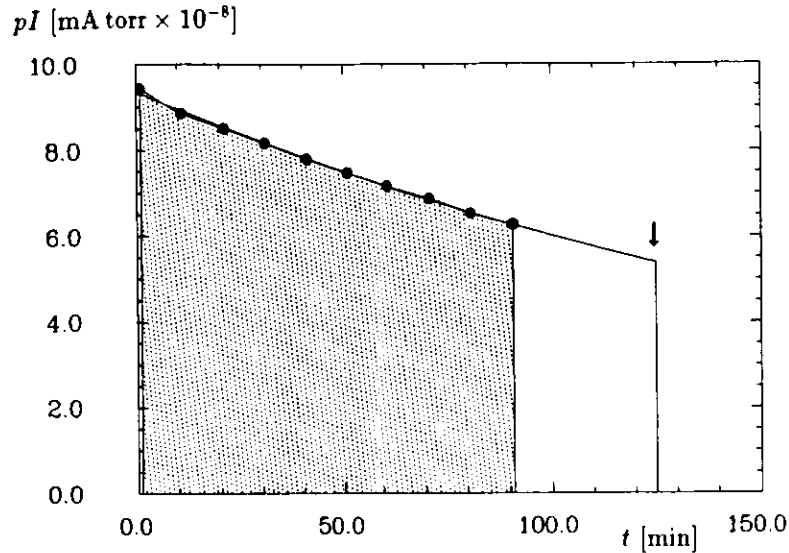


Figure 4.17: The principle of finding the $pI dt$ (or $I dt$) normalization factors. Shaded area is the one obtained directly from experimental points. Three records at the end of the run# 18886 were missing. The arrow indicates the end of run. Extrapolation results in big correction (hollow area under the fitted curve).

beam optics between single beam and colliding beam runs. We have not measured either $I dt$ nor $pI dt$ directly. We did record so-called "MON events" (Monitor ONLINE), approximately every 10 min. These events contain, among other informations, time, beam currents, and pressure near the interaction region. As a result, the application of methods 1 and 2 was possible. We used:

1. Start of run records—for the start time of a run;
2. MON records—for current and pressure readout; for the time within a run;
3. end of run records—for the end time of a run.

The resulting data are thus composed of discrete points rather than the continuous information we are interested in. We now have to find the analytic approximation of the data, allowing us to extrapolate outside beyond the measured points (i.e. to the beginning and the end of run). The following procedure was used:

1. take the runs with at least 4 MON records;
2. assume the accuracy of 0.1 mA for current readout and 1% for vacuum readout;¹

¹The 1% error is by far too small if one uses the absolute vacuum readout. For the fit purposes we will be interested in relative errors.

3. fit the time dependence of the data ($I(t)$ or $pI(t)$) to

$$f(t) = N \cdot \exp \frac{-t}{a \cdot t + b} \quad (4.4)$$

where N , a and b are free fit parameters (a is small). Such a choice of the fit function was dictated by its flexibility. The parameter a accounts for the change of the beam lifetime due to the beams getting "cooled down".

4. if a is compatible with 0, set $a = 0$ and repeat the fit with a fixed (i.e. two parameter fit);
5. if two runs are on the same DORIS fill, fit the runs together.²

The principle of this method is shown in fig. 4.17. In this case the extrapolation stability can be checked since we have continued running with the old beams. The stability was found to be good at a level of $\sim 0.7\%$. Figs. 4.18 and 4.19 show the data points with the fitted curves. Despite the small experimental errors generally the χ^2 of all fits was reasonable, giving typically a value of $\chi^2 / N_{DOF} \sim 1$. Now, to estimate the background in the hadronic sample, we ran the selector program on the single- or separated-beam runs, finding N_{SB} events passing our selection criteria and $(\int pI dt)_{SB}$ for these runs. Repeating this procedure for colliding beam data, we find $N_{hadrons}$ and $(\int pI dt)_{data}$, respectively. For any run the fraction of background events due to beam-gas interactions, f_{BG} , can be found as:

$$f_{BG} = \left[\frac{N_{SB}}{\int pI dt} \right]_{single\ beam} \times \left[\frac{\int pI dt}{N_{hadrons}} \right]_{data} \quad (4.5)$$

Due to limited statistics of single beam runs taken in the $\Upsilon(1S)$ mass region the statistical errors of this method are large and dominated by the statistics of $N_{SB} = 5_{-1}^{+3}$ (this figure corresponds to ~ 10 hours of single beam running). For the discussion of asymmetric errors see appendix C. Table 4.4 gives the values of different normalization factors using the above-mentioned methods. Double entry for current integrals is caused by the fact that we record the e^+ and e^- current reading, and their sum measured by a different meter, while for the pressure we get the vacuum read at both sides of the interaction region. The beam-gas background reaching the experiment is always produced upstream. Taking this into account we can create only one pI product. Values of the f_{BG} factors found for the data taken close in time to single beam runs are given in a separate row. A systematic uncertainty of $\pm 10\%$ for the f_{BG} stems from the maximal difference between f_{BG} values found in this manner. This method is quite general and the normalization factors can be applied to any selection.

The second method makes use of Monte Carlo simulations. For a given hadronic event selector

$$N_{hadrons} = \mathcal{L} \sum_i \sigma_i \epsilon_i + N_{BG} \quad (4.6)$$

²It sometimes happened, for technical reason, that DORIS was not able to get a new injection. The beams then were not dumped and the new run was started with the same beams.

Table 4.4: Normalization and f_{BG} factors obtained by using different methods

Run#	Different normalization factors			N_{SB}
	Fit result			
	$\int I dt$ [mAmin]	$\int I dt$ [mAmin]	$\int pI dt$ [mAmin torr 10^{-8}]	
18881	3772.0	3739.0	743.6	3
18882	1445.3	1441.2	405.8	1
18885	4429.5	4367.1	685.3	1
18886†	4014.7	3984.5	892.8	0
18887†	3475.9	3422.2	487.3	0
†Same DORIS run - see text				
	f_{BG} factors			$N_{hadrons}$
$f_{BG}[\%]$	0.77	0.84	0.87	1288

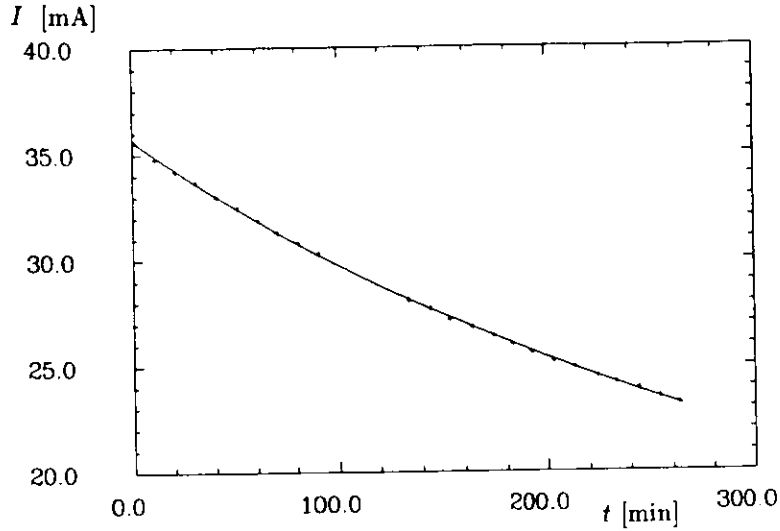


Figure 4.18: The total current for runs# 18886 and 18887 as a function of time. For the line see text.

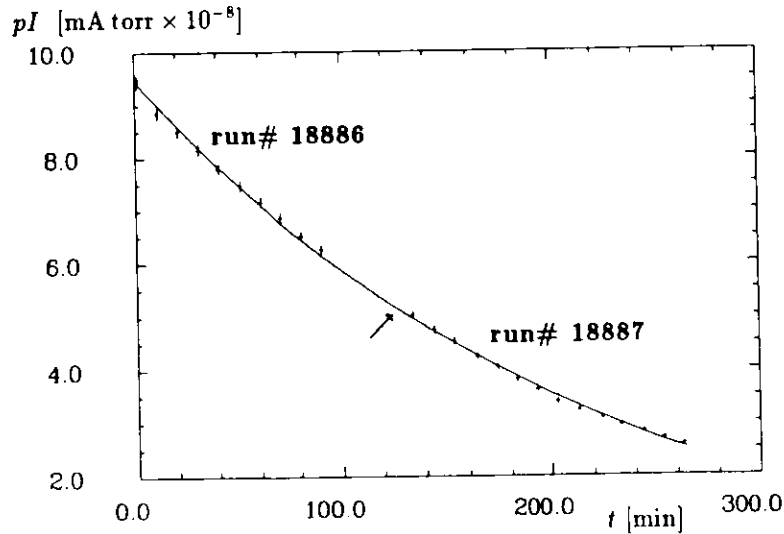


Figure 4.19: Current pressure pI product for runs# 18886 and 18887 as a function of time. The arrow indicates end of run# 18886. For the line see text.

where $N_{hadrons}$ is the number of accepted hadronic events, N_{BG} the number of beam-gas events, \mathcal{L} the integrated luminosity, σ_i and ϵ_i cross sections and corresponding efficiencies for processes leading to hadrons in the final state. The latter two are determined by Monte Carlo simulations of the relevant processes. By varying our cuts we can obtain a substantially larger fraction of beam-gas events in our hadronic data sample without dramatic changes in the efficiencies. For the modified selection criteria then

$$N'_{hadrons} = \mathcal{L} \sum_i \sigma_i \epsilon'_i + c N_{BG} \quad (4.7)$$

The factor c is the relative acceptance of the two sets of cuts for beam-gas events, and is determined using single-beam data. Subtracting eq. 4.6 from 4.7 we get

$$\Delta N_{hadrons} = \mathcal{L} \sum_i \sigma_i \Delta \epsilon_i + (c - 1) N_{BG} \quad (4.8)$$

Since $c \approx 21$ and the efficiencies are not very different, $\Delta \epsilon_i \ll 1$ (typically $< 5\%$), $\Delta N_{hadrons}$ is fairly insensitive to the cross sections used. Solving eq. 4.8 for N_{BG} gives the desired number of beam-gas events.

Both methods gave similar results. The f_{BG} factor as a function of run number is shown in fig. 4.20. As we have already shown, finding f_{BG} with use of $I dt$ or $pI dt$ suffers from small statistics. The background used was found following the second method (using data). A systematic error of 10% was found as the maximal variation of the mean values given by different methods. Taking the luminosity-weighted average we find that beam-gas background contributes only a very small fraction to our hadronic scan data sample compared to the continuum $e^+e^- \rightarrow hadrons$.³

$$f_{BG} \equiv N_{BG}/N_{hadrons} = (0.60 \pm 0.01 + 0.06)\% \quad (4.9)$$

³We do not find any resonant background behavior

Fig. 4.20 supports the hypothesis that background is machine-condition-dependent and thus we cannot include the other single beam runs (not taken closely in time to our data-taking period) for the background calculation within the first method. The lines show the background variation over three scan periods. The continuous solid line shows the average background for all scan data used in the analysis. The continuum data at $W = 9.39$ GeV used for the R determination were taken soon before and after the May'86 scan and have a background level compatible with it:

$$f_{BG} \equiv N_{BG}/N_{hadrons} = (0.30 \pm 0.01 \pm 0.03)\% . \quad (4.10)$$

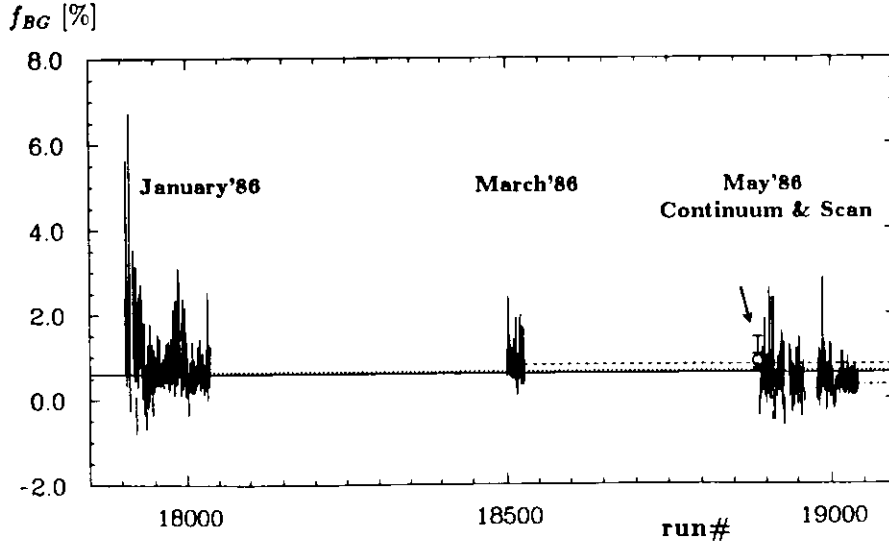


Figure 4.20: The f_{BG} factor obtained from data as a function of the run number. The fact that for different run periods we obtain different background levels reflects the fact that background is connected with the machine conditions. The open point shows the measurement obtained by $\int pI dt$ method (the small error bars are systematical, large statistical). For the lines see text.

5. Determination of Γ_{ee}

5.1 Γ_{ee} Measurements

As outlined in section 2.4, the resonance parameters M and Γ_{ee} are determined by fitting the following function to the observed hadronic cross section:

$$\sigma^{obs}(W) = A^{obs} \frac{\exp(-z^2/4)}{\Delta\sqrt{2\pi}} N'_{KF}(z) + \frac{C}{W^2} . \quad (5.1)$$

The first term accounts for the decays $\Upsilon \rightarrow hadrons$. $A^{obs} = A\epsilon_H^R$ is the area of the Breit-Wigner multiplied by our hadronic detection efficiency for resonance decays. The resonance mass M enters through the variable $z \equiv (W - M)/\Delta$. Radiative corrections are treated according to the prescription of Kuraev and Fadin [16], using $N'_{KF}(z)$ from eq. 2.32 b. The second term reflects hadron production from the continuum, which to lowest order scales as $1/W^2$. Over the narrow energy region used in the fits, the C/W^2 continuum part of $\sigma^{obs}(W)$ will include nearly all contributions from the background sources discussed in section 4.3.

The data samples of hadronic events used for our Γ_{ee} determinations are summarized in table 5.1. We have performed four scans over the $\Upsilon(1S)$ resonance and one scan over the $\Upsilon(2S)$. Each scan has approximately 100 nb^{-1} per point. The value of Γ_{ee} determined from the scans is insensitive to small overall changes (of the order of ± 10 MeV) in the absolute energy scale. It is, however, sensitive to the point-to-point error of the energy measurement.

The most precise beam energy measurement at e^+e^- storage rings can be made by us-

Table 5.1: Data samples for the $\Upsilon(1S)$ and $\Upsilon(2S)$ scans and continuum data: energy range, number of hadronic events, total luminosity with statistical error, and number of data points.

Scan	W range GeV	# hadrons	$\Sigma \mathcal{L}$ $[\text{nb}^{-1}]$	# points
$\Upsilon(1S)$ scans				
1	9.388-9.506	12195	2204 ± 12	21
2	9.445-9.477	6032	690 ± 7	9
3	9.436-9.481	4008	567 ± 6	7
4	9.444-9.479	5139	670 ± 7	8
Total		27374	4131 ± 17	45
$\Upsilon(2S)$ scan				
	9.966 - 10.039	4367	994 ± 9	10
Continuum data				
	9.39	25825	7135 ± 22	

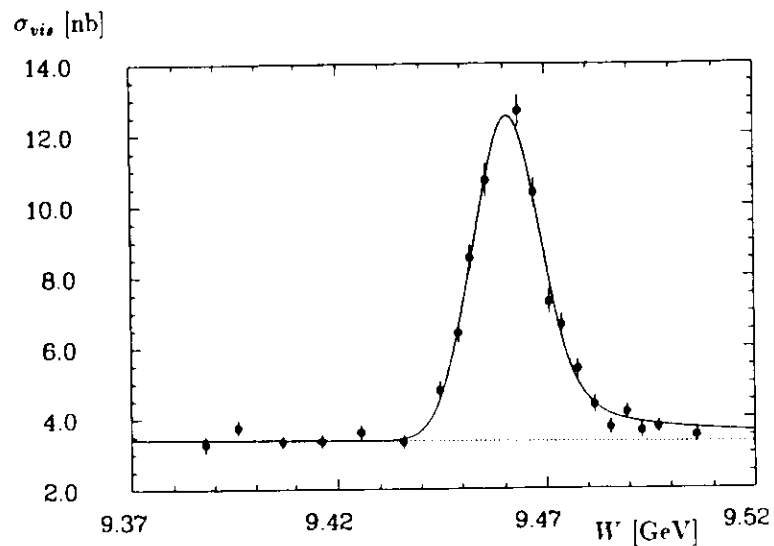


Figure 5.1: Scan #1: visible cross section vs. energy.

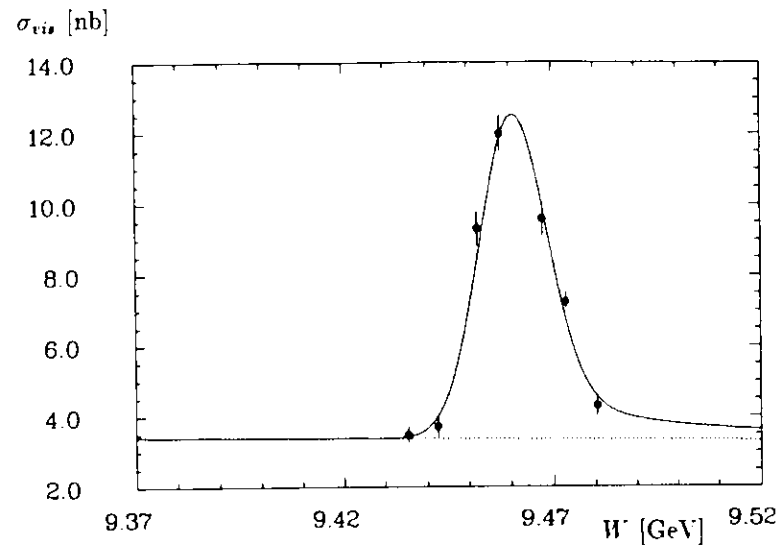


Figure 5.3: Scan #3: visible cross section vs. energy.

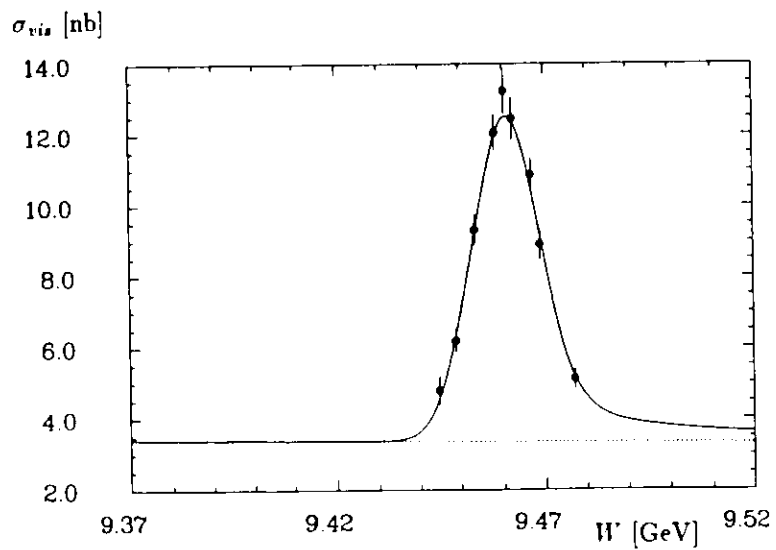


Figure 5.2: Scan #2: visible cross section vs. energy.

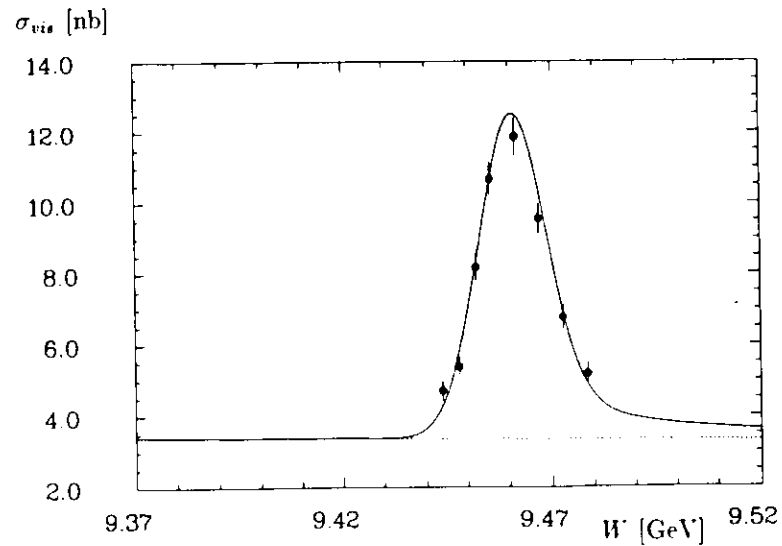


Figure 5.4: Scan #4: visible cross section vs. energy.

ing the depolarization technique [39], if the beams are polarized. Due to the emission of synchrotron radiation electron and positron beams become polarized via the Sokolov-Ternov effect [25]. DORIS-II provides a beam polarization of up to 80% in the $\Upsilon(2S)$ energy region thus allowing a very precise energy determination for our $\Upsilon(2S)$ scan data: $\sigma_E/E \sim 2 \times 10^{-5}$. Details of this measurement can be found in [40].

In the $\Upsilon(1S)$ energy region the beam polarization is destroyed completely by storage ring resonances specific to the DORIS-II machine configuration. Here the most precise measure of the relative beam energy comes from the determination of the magnetic field B at the beam position of a storage ring bending magnet using the nuclear-magnetic-resonance effect. The accuracy achieved here is $\sigma_B/B \sim 5 \times 10^{-5}$.

The determination of the beam energy from the magnetic field measurement depends on the machine parameters, which change with time, and on the degree of saturation of the magnets, which depends on the history of energy changes. We observe shifts of order 10 MeV between different run periods and smaller shifts between successive scans. In order to achieve as much stability as possible during a scan we always scanned with monotonically increasing beam energy and completed each scan within a period of a few days, during which the machine parameters were held as constant as possible. The point-to-point error on the c.m. energy is taken from $\sigma_B/B = 5 \times 10^{-5}$ to be 0.5 MeV. Although Γ_{ee} is nearly unaffected by small uncertainties in the absolute energy scale (of order ± 10 MeV), we avoid any systematic influence from this effect by choosing the normalization factor between energy and magnetic field so that the fitted resonance mass is equal to the nominal mass $M_{\Upsilon(1S)} = (9460.0 \pm 0.2)$ MeV [5]. For the limited energy range of our scans the beam energy is a linear function of the magnetic field B .

5.1.1 Γ_{ee} of the $\Upsilon(1S)$

We first fit each scan individually to the function eq. 5.1 with four free parameters: A^{obs} , Δ , M , and C . Only scan number 1 covers a wide enough W range for a good determination of the continuum constant C . Then we fit scans 2 to 4 with C fixed to the result obtained from scan 1. This results in the A^{obs} values labeled "fixed" in table 5.2. They agree within errors, but are not statistically independent and cannot simply be averaged to improve the statistical accuracy.

For our final result we fit the four scans simultaneously, allowing relative energy shifts between them as three additional free parameters. This makes maximum use of the continuum information and gives a statistically correct average of A^{obs} . The result of this fit, with the data of each scan corrected for its relative energy shift, is shown in fig. 5.5. The χ^2 of 45.4 for 37 degrees of freedom corresponds to a confidence level of 16.1%. The parameter values are: $A^{obs} = (286 \pm 6)$ nb MeV, $\Delta = (7.8 \pm 0.2)$ MeV, and $C = (300 \pm 6)$ nb GeV². Scans 2, 3 and 4 are shifted in nominal c.m. energy from scan 1 by (-4.0 ± 0.4) MeV, (-8.6 ± 0.4) MeV,

Table 5.2: Results of fits to $\Upsilon(1S)$ scans. Errors are statistical only. CL is the confidence level of the particular fit.

Scan	A^{obs} [nb MeV]	Δ [MeV]	C [nb GeV ²]	CL [%]
1	289 ± 8	7.7 ± 0.3	300 ± 6	14.2
2	269 ± 32	7.2 ± 0.6	327 ± 48	74.3
3	312 ± 19	8.3 ± 0.5	280 ± 20	4.0
4	221 ± 21	6.8 ± 0.6	374 ± 31	32.9
2	288 ± 9	7.5 ± 0.3	fixed at 300	81.6
3	298 ± 11	7.9 ± 0.3	fixed at 300	6.2
4	271 ± 9	8.0 ± 0.3	fixed at 300	12.8

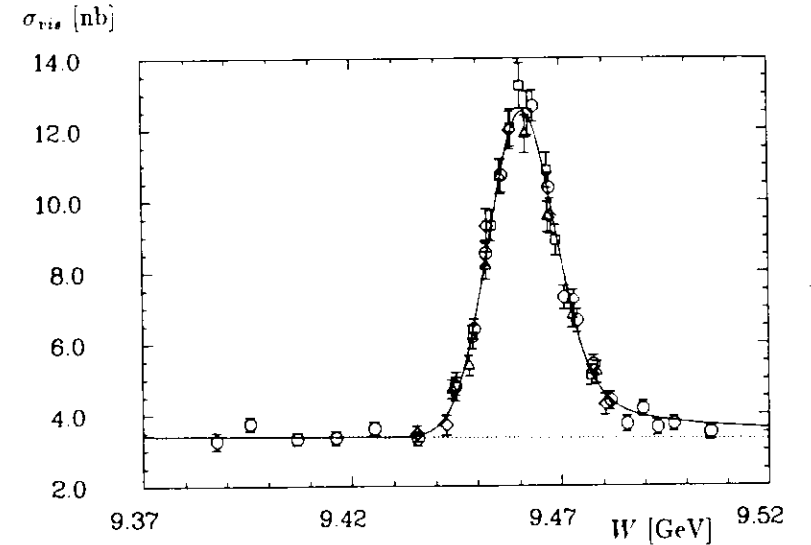


Figure 5.5: Observed cross section vs. c.m. energy W for the four $\Upsilon(1S)$ scans. Circles represent scan 1, squares scan 2, triangles scan 3, and diamonds scan 4. The full line is the fit result; the dotted line shows the fitted background.

(-7.8 ± 0.4) MeV, respectively. The machine resolution Δ is compatible with the expected value of 7.6 MeV.

$\Gamma_{ee} B_{had}$ is calculated from eq. 2.31 and $A = A^{obs}/\epsilon_H^R$ where ϵ_H^R is the probability that a resonance decay is accepted in our hadronic sample. To obtain ϵ_H^R we use the Monte Carlo techniques described in section 4.2. With the standard LUND program version 6.2 [30] we generate the following $\Upsilon(1S)$ decay modes with branching ratios according to the Particle Data Group values [5]: a) decays into 3 gluons and γgg ; b) direct decays to $q\bar{q}$; c) decays

Table 5.3: Compilation of $B_{\mu\mu}$ values (in%) for $\Upsilon(1S)$ and $\Upsilon(2S)$.

Reaction	$B_{\mu\mu}$ [%]	Experiment
$\Upsilon(1S)$		
$\Upsilon \rightarrow \mu\mu$	2.2 ± 2.0	PLUTO [41]
$\Upsilon \rightarrow \mu\mu$	$1.4^{+3.4}_{-1.4}$	DESY-Heid. [42]
$\Upsilon \rightarrow \mu\mu$	$3.2 \pm 1.3 \pm 0.3$	DASP II [43]
$\Upsilon \rightarrow \mu\mu$	$3.8 \pm 1.5 \pm 0.2$	LENA [44]
$\Upsilon \rightarrow \mu\mu$	$2.7 \pm 0.3 \pm 0.3$	CLEO [53]
$\Upsilon \rightarrow \mu\mu$	$2.7 \pm 0.3 \pm 0.1$	CUSB [45]
$\Upsilon \rightarrow ee$	5.1 ± 3.0	PLUTO [46]
$\Upsilon(2S) \rightarrow \pi^+\pi^-\Upsilon, \Upsilon \rightarrow \mu^+\mu^-, e^+e^-$	$2.84 \pm 0.18 \pm 0.20$	CLEO [47]
$\Upsilon(2S) \rightarrow \pi^+\pi^-\Upsilon, \Upsilon \rightarrow \mu^+\mu^-, e^+e^-$	$2.39 \pm 0.12 \pm 0.14$	ARGUS [48]
$\Upsilon \rightarrow \tau\tau$	$3.4 \pm 0.4 \pm 0.4$	CLEO [49]
	2.63 ± 0.12	average
$\Upsilon(2S)$		
$\Upsilon(2S) \rightarrow \mu\mu$	$1.8 \pm 0.8 \pm 0.5$	CLEO [50]
$\Upsilon(2S) \rightarrow \mu\mu$	$1.4 \pm 0.3 \pm 0.2$	CUSB [45]
$\Upsilon(2S) \rightarrow \mu\mu$	$1.0 \pm 0.6 \pm 0.5^*$	ARGUS [51]
$\Upsilon(2S) \rightarrow \tau\tau$	$1.7 \pm 1.5 \pm 0.6$	CLEO [50]
	1.4 ± 0.3	average

* The ARGUS $\Upsilon(2S)$ value is scaled from the average $\Upsilon(1S)$ value with $B_{\mu\mu}(2S) = 1.57 \pm 0.59 \pm 0.53 + 2.1(B_{\mu\mu}(1S) - 2.9)$ (in %) [51].

into two leptons. Typical detection efficiencies for the Υ resonances are a) $\epsilon_{3p}^{\Upsilon} = 90\%$, b) $\epsilon_{e\bar{q}}^{\Upsilon} = 80\%$, c) $\epsilon_{\pi^+\pi^-}^{\Upsilon} = 15\%$, whereas $\epsilon_{e^+e^-}^{\Upsilon}$ and $\epsilon_{\mu^+\mu^-}^{\Upsilon}$ are negligibly small. We get as total detection efficiency $\epsilon_H^{\Upsilon(1S)} = (83.1 \pm 0.1 \pm 2.4)\%$ (see table 4.2). The first error results from Monte Carlo statistics, whereas the second systematic error originates from the hadronization model used and the detector response. We find a 1.4% difference in the efficiency using the standard LUND string fragmentation and a coherent parton shower model. In addition we estimate a 2.5% systematic error to account for uncertainties in modeling the detector response.

Using the measured value of A^{obs} and $\epsilon_H^{\Upsilon(1S)}$ we obtain

$$\Gamma_{ee} B_{had} = (1.23 \pm 0.02 \pm 0.05) \text{ keV}. \quad (5.2)$$

The 4.1% systematic error is explained in section 5.1.3. Division by $B_{had} = 1 - 3B_{\mu\mu}$ using the world average of $B_{\mu\mu}(\Upsilon(1S)) = (2.63 \pm 0.12)\%$ from table 5.3 yields

$$\Gamma_{ee} = (1.34 \pm 0.03 \pm 0.06) \text{ keV}. \quad (5.3)$$

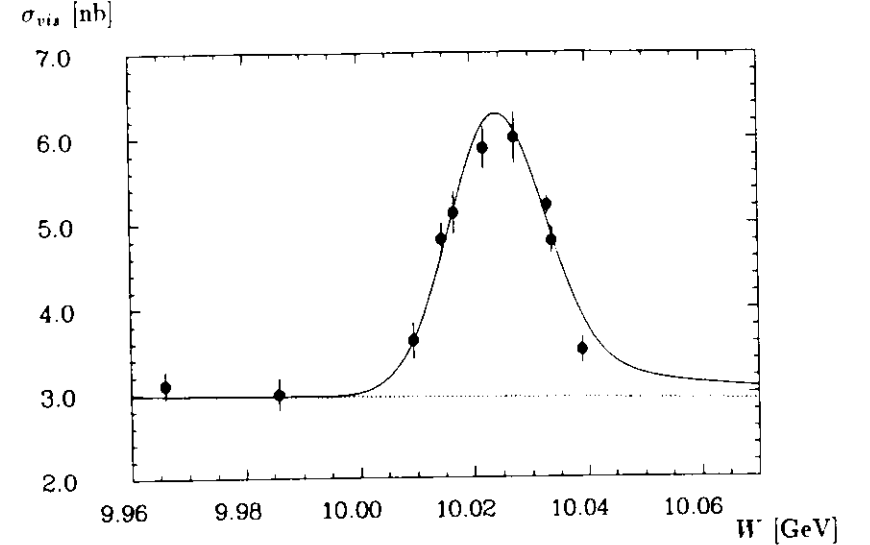


Figure 5.6: Observed cross section vs. c.m. energy W for the $\Upsilon(2S)$ scan. The full line is the fit result, the dotted line shows the fitted background.

5.1.2 Γ_{ee} of the $\Upsilon(2S)$

For the scan over the $\Upsilon(2S)$ we have the $\sigma_E \approx 0.2$ MeV energy determination for each scan point from depolarization measurements. Fitting our data as a function of energy to the expression of eq. 5.1 gives the following results for the parameters: $M = (10023.5 \pm 0.4)$ MeV; in agreement with our published value [40] and that of ref. [5]; $A^{obs} = (110 \pm 8)$ nb MeV; $\Delta = (8.2 \pm 0.5)$ MeV, which agrees with the expected machine resolution of 8.5 MeV at $M_{\Upsilon(2S)}$; $C = (296 \pm 12)$ nb GeV², compatible with the value found at the $\Upsilon(1S)$. The fit has a χ^2 of 12.5 for five degrees of freedom corresponding to a 2.8% confidence level. The data and the resulting fit curve are shown in fig. 5.6.

The Monte Carlo event sample used to determine the hadronic detection efficiency for the $\Upsilon(2S)$ includes (in addition to the decay channels considered for the $\Upsilon(1S)$) the following decay modes: d) radiative decays to the three $^3P_{0,1,2}$ states, which in turn either decay radiatively to the $\Upsilon(1S)$ or via 2 gluons ($^3P_0, ^3P_2$) or 3 gluons (3P_1); e) $\pi^+\pi^-$ and $\pi^0\pi^0$ transitions to the $\Upsilon(1S)$. The events were generated with a beam polarization of 80% as observed in our data. We obtain a detection efficiency (see table 4.2) of $\epsilon_H^{\Upsilon(2S)} = (85.4 \pm 0.2 \pm 2.5)\%$ with statistical and systematic errors as discussed for the $\Upsilon(1S)$ in section 5.1.1. Using this value, the measured value of A^{obs} and $B_{\mu\mu} = (1.4 \pm 0.3)\%$ from table 5.3, we obtain

$$\Gamma_{ee} B_{had} = (0.54 \pm 0.04 \pm 0.02) \text{ keV} \quad (5.4)$$

and

$$\Gamma_{ee} = (0.56 \pm 0.04 \pm 0.02) \text{ keV}. \quad (5.5)$$

The formula for rescaling the ARGUS $B_{\mu\mu}(2S)$ value used in the table 5.3 contains a factor stemming from the luminosity, number of observed events, acceptances etc. and thus is not generally valid. The term 2.9 is the world average $B_{\mu\mu}(2S)$ at the time when the ARGUS publication was written.

5.1.3 Systematic errors for Γ_{ee}

One of the largest contributions to the systematic error comes from the 2.5% uncertainty in the luminosity determination.

A 2.8% systematic error on the detection efficiencies for the $\Upsilon(1S)$ and the $\Upsilon(2S)$ is the quadratic sum of the contributions already discussed in section 5.1.1.

We allow a 1.5% error for the dependence on cuts, found by varying them within acceptable limits and by using an alternative hadron selection method described in ref. [29].

Next we consider the effect of backgrounds in our data sample. Background contributions from the continuum QED processes $e^+e^- \rightarrow e^+e^-, \gamma\gamma, \mu^+\mu^-,$ and $\tau^+\tau^-$ are already suppressed by our event selection. Moreover, the lowest order cross sections for these processes all scale like $1/W^2$, so that events of this type are mostly included in the C/W^2 term. The determination of the area A^{obs} under the resonance curve is not affected by background contributions. In section 4.3.3 we estimate the beam-gas contamination to be 0.6%. This background has a flat distribution as a function of energy and is almost completely absorbed in the continuum term C/W^2 of eq. 5.1. Two photon reactions have a cross section proportional to $\ln W^2$, as do higher-order corrections to the continuum QED background. To check for any such background we also perform fits to the data adding a second background term $C' \ln W^2$ to eq. 5.1. These fits give $C' = (0 \pm 3) \text{ nb}$, $C = (300 \pm 10) \text{ nb GeV}^2$. The latter value is the same as obtained in section 5.1 without the $\ln W^2$ term. Also all other fitted parameters are completely unaffected by adding such a term. Over the scanned energy range, the value found for C' , which is highly anticorrelated with C , would result in a 0.3% change (at the 1 S.D. level) of the background, if there were contributions from processes with energy dependence proportional to $\ln W^2$.

To test for possible c.m. energy shifts within each individual scan, we make several additional fits to them. Between any two scan points we split each scan into two periods, allowing as an additional fit parameter an energy shift in one period with respect to the other. Within errors the fitted single shifts are always compatible with zero. The probability that all shifts together are zero is as high as 31%. Again within errors the fitted A^{obs} does not deviate from the values given in section 5.1 obtained without any shift.

Combining the errors quadratically we obtain a 4.1% systematic error on our $\Gamma_{ee} B_{had}$ values. Dividing by $1 - 3B_{\mu\mu}$ to obtain Γ_{ee} introduces an additional systematic error of 0.4%

Table 5.4: Measurements of $\Gamma_{ee} B_{had}$ (in keV). The type of radiative correction that was used in each published value is listed, and the rescaled value is given. KF: Kuraev and Fadin, JS: Jackson and Scharre, GPS: Greco et al.

Published $\Gamma_{ee} B_{had}$	Rad. corr.	Rescaled value	Experiment
$\Upsilon(1S)$			
1.00 ± 0.23	JS	1.09 ± 0.25	DESY-Heidelberg [42]
$1.10 \pm 0.07 \pm 0.11$	GPS	1.13 ± 0.13	LENA [44]
$1.12 \pm 0.07 \pm 0.04$	JS	1.23 ± 0.09	DASP II [43]
$1.17 \pm 0.05 \pm 0.08$	JS, full Π	1.37 ± 0.11	CLEO [52]
$1.04 \pm 0.05 \pm 0.09$	JS	1.17 ± 0.11	CUSB [54] (unpub.)
		$\overline{1.22 \pm 0.05}$	prev. average
	KF	$1.23 \pm 0.02 \pm 0.05$	this experiment
		1.23 ± 0.04	new average
$\Upsilon(2S)$			
0.37 ± 0.16	JS	0.41 ± 0.18	DESY-Heidelberg [42]
$0.53 \pm 0.07^{+0.09}_{-0.06}$	GPS	0.54 ± 0.12	LENA [44]
$0.55 \pm 0.11 \pm 0.06$	JS	0.60 ± 0.14	DASP II [43]
$0.49 \pm 0.03 \pm 0.04$	JS, full Π	0.58 ± 0.06	CLEO [52]
$0.53 \pm 0.03 \pm 0.05$	JS	0.59 ± 0.06	CUSB [54] (unpub.)
		$\overline{0.57 \pm 0.04}$	prev. average
	KF	$0.54 \pm 0.04 \pm 0.02$	this experiment
		0.56 ± 0.03	new average

for the $\Upsilon(1S)$ and of 1.3% for the $\Upsilon(2S)$.

5.2 Discussion of Γ_{ee} Results

Previous measurements of Γ_{ee} of the Υ 's used either the Jackson-Scharre or the Greco et al. formulation of radiative corrections, which differ from the Kuraev-Fadin form we used, as discussed in section 2.4. However, all of the forms in eqs. 2.28 and 2.32 give very similar shapes with differences appearing in the normalization. Thus previous measurements can be renormalized to correspond to the Kuraev-Fadin formulation by comparing the values of $N(z=0)$ in eqs. 2.28 and 2.32. This is done in table 5.4 and the rescaled measurements are compared to our values. Here we compare $\Gamma_{ee} B_{had}$ rather than Γ_{ee} to remove the dependence on $B_{\mu\mu}$, which was not very well known at the time of the earliest Γ_{ee} measurements. Adding the statistical and systematic errors in quadrature shows our result to be the most precise single measurement for the $\Upsilon(1S)$ as well as for the $\Upsilon(2S)$. Agreement with the world averages, which were calculated without our values, is excellent.

Based on our data we give a comparison of Γ_{ee} values for the $\Upsilon(1S)$ obtained applying the four different radiative corrections according to eqs. 2.28 and 2.32 in fig. 5.7, the errors

Table 5.5: Rescaling factors for Γ_{ee} . Ratios of $N(z=0)$ compared to Γ_{ee} ratios from fits to our $\Upsilon(1S)$ scans using different prescriptions for radiative corrections. The smallness of the errors on the measured ratios arises from the positive correlation of individual Γ_{ee} values. KF: Kuraev and Fadin, JS: Jackson and Scharre, GPS: Greco et al., T: Tsai.

Radiative corrections	Ratio from Γ_{ee}	Ratio from $N(z=0)$
KF/JS	1.08655 ± 0.00010	1.09340
KF/GPS	1.02600 ± 0.00002	1.02600
KF/T	0.99955 ± 0.00003	0.99911

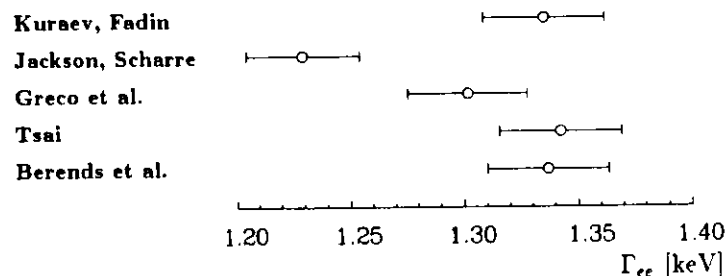


Figure 5.7: Compilation of our Γ_{ee} results for the $\Upsilon(1S)$ obtained using different radiative corrections: Kuraev and Fadin [16], Jackson and Scharre [13], Greco et al. [14], Tsai [15], full $\mathcal{O}(\alpha^4)$ calculation by Berends et al. [17]. The errors are statistical only.

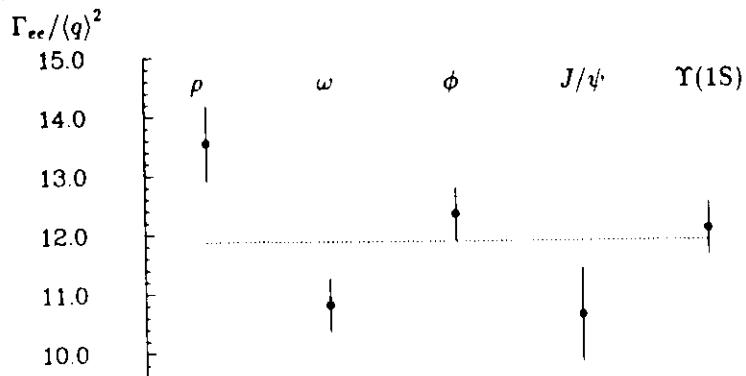


Figure 5.8: The ratio of Γ_{ee} to the square mean of quark charge for vector mesons. The result for $\Upsilon(1S)$ agrees with the value expected from the Van Royen-Weisskopf formula if one assumes a charge $q = 1/3$ for b -quarks.

shown are statistical only. Although Tsai's ansatz [15] has been criticized by Kuraev and Fadin, both prescriptions give nearly the same Γ_{ee} result, since they are equal to the order of corrections considered here. The point marked as "Berends et al." shows the result using their $\mathcal{O}(\alpha^4)$ calculation [17]. Using the expressions of Jackson and Scharre [13], eq. 2.28 a, and of Greco et al. [14], eq. 2.28 b, the Γ_{ee} values are lower than all others due to the inclusion of δ_e , the electronic vacuum polarization contribution. In table 5.5 we compare ratios of $N(z=0)$ to the corresponding ratios of Γ_{ee} values extracted from our $\Upsilon(1S)$ scans using the various prescriptions. The agreement to better than 1% supports the applicability of the rescaling procedure.

We thus arrive at one of the most precise experimental results on $\Gamma_{ee}(\Upsilon(1S))$ and $\Gamma_{ee}(\Upsilon(2S))$. Γ_{ee} and $B_{\mu\mu}$ together with the relations

$$\begin{aligned} B_{had} + 3B_{\mu\mu} &= 1 \\ \Gamma_{tot} &= \Gamma_{ee}/B_{\mu\mu} \end{aligned} \quad (5.6)$$

determine the basic resonance decay parameters. However, eqs. 5.6 require a consistent treatment of the radiative corrections.

With this drastically changed value of Γ_{ee} (data from ref. [55] have to be compared with [5]) and a substantial reduction in the experimental errors it is interesting to reinspect the implications of the van Royen-Weisskopf formula 2.20. Figure 5.8 shows the ratio of Γ_{ee} to the square mean of quark charge for vector mesons using the data from [55]. The result for $\Upsilon(1S)$ agrees with the value expected from the Van Royen-Weisskopf formula if one assumes a charge $q = 1/3$ for b -quarks.

6. Determination of R at $W = 9.39$ GeV

6.1 Measurement of R

We have $\sim 7.1 \text{ pb}^{-1}$ of data (see table 5.1) taken in the continuum below the $\Upsilon(1S)$ at c.m. energy $W = 9.39$ GeV. The observed hadronic cross section σ^{obs} is given by N_{hadrons} , the number of selected hadronic events, and the luminosity \mathcal{L} :

$$\sigma^{\text{obs}} = \frac{N_{\text{hadrons}}}{\mathcal{L}}. \quad (6.1)$$

To compare with the continuum contribution found in our $\Upsilon(1S)$ scans we again use the quantity C (see eq. 5.1):

$$C = \sigma^{\text{obs}} W^2. \quad (6.2)$$

C was determined run by run (see fig. 6.1). Taking the weighted average we obtain $C = (300.38 \pm 2.86) \text{ nb GeV}^2$. Combining eq. 2.7 with eq. 6.2 gives the observed R^{obs} :

$$R^{\text{obs}} = \frac{C}{86.9 \text{ nb GeV}^2}. \quad (6.3)$$

The method to obtain R from R^{obs} is discussed in detail in refs. [2] and [7]. Combining eq. 2.11 with eq. 6.3 we obtain the following formula:

$$R = \frac{R^{\text{obs}}(1 - f_{BG}) - \Delta R_{QED} - \Delta R_{\gamma\gamma}}{\epsilon_{q\bar{q}}^C (1 + \delta_R)}. \quad (6.4)$$

δ_R accounts for the initial state radiative corrections, $\delta_R = 0.29$ [7] at $W = 9.39$ GeV. Here a cut-off at 1% of the beam energy has been applied for the energy of bremsstrahlung photons in the Monte Carlo program. $f_{BG} = 0.3\%$ is the percentage beam-gas contamination (see section 4.3.3). $\Delta R_{QED} = 0.187 \pm 0.005$ is the background at $W = 9.39$ GeV from the continuum QED processes $e^+e^- \rightarrow e^+e^-, \gamma\gamma, \mu^+\mu^-,$ and $\tau^+\tau^-$ which pass our hadron selection criteria. $\Delta R_{\gamma\gamma} = 0.020 \pm 0.006$ is the background from two-photon collisions. The ΔR are calculated from $\epsilon\sigma$ of table 4.3 as $\Delta R = \epsilon\sigma W^2 / (86.9 \text{ nb GeV}^2)$. $\epsilon_{q\bar{q}}^C$ is the detection efficiency for continuum hadron production. We use the average of the $e^+e^- \rightarrow q\bar{q}$ efficiencies obtained with the standard LUND string fragmentation and the coherent parton shower model (labelled as ‘‘LUND string’’ and ‘‘coherent shower’’ in table 4.2).

6.2 Systematic Error on R

The systematic error on R receives contributions from the following sources: The 1.4% difference of the efficiencies for the ‘‘LUND string’’ and the ‘‘coherent shower’’ models is

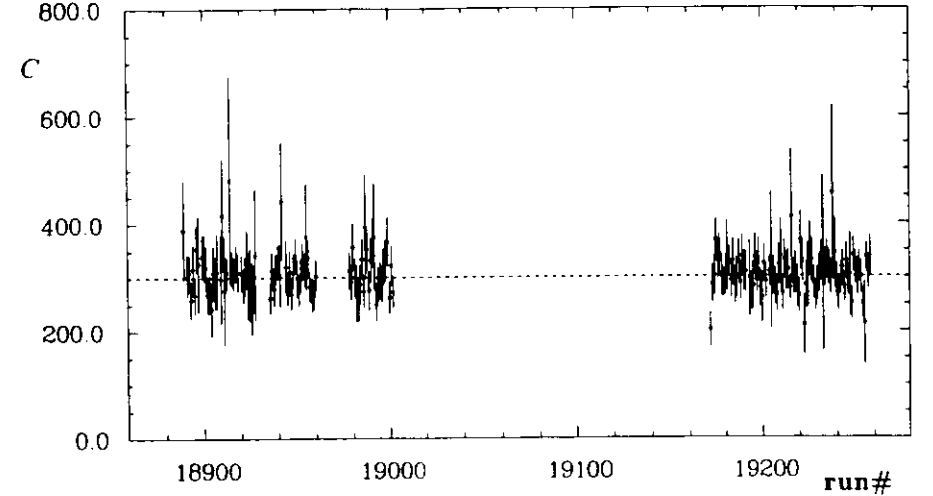


Figure 6.1: C value as a function of run number. The line shows the average value of $C = (300.38 \pm 2.86) \text{ nb GeV}^2$.

taken as systematic uncertainty resulting from the hadronization model used. The error on the luminosity determination is 2.5%. The backgrounds which have to be subtracted are already small because of our selection cuts. The systematic error on the beam-gas fraction is $\Delta f_{BG}/f_{BG} = 10\%$. If we conservatively allow for a 5% systematic uncertainty in ΔR_{QED} , and if we assume that for two-photon background the cross sections of both, the GVDM and QPM contributions, are known only within a factor of 2, then the background subtraction affects our R by less than 0.6%. The dependence on hadron selection is determined as described in section 5.1.3 and contributes 2.5%. Finally, according to ref. [7], δ_R is known to 1%. The factor $(1 + \delta_R)^{-1}$ thus gives another 0.1% systematic uncertainty. Adding the different contributions quadratically we assign a 3.9% systematic error to the measured R value. We then obtain

$$R = 3.49 \pm 0.04 \pm 0.14$$

at $W = 9.39$ GeV, where the errors are statistical and systematic, respectively.

As a cross check of this result we also determine R from the continuum contribution in our scan data by the same method as discussed above. Here C is the value of the continuum parameter C found in the fit to our $\Upsilon(1S)$ scans. We obtain

$$R = 3.47 \pm 0.07 \pm 0.14$$

at $W = 9.46$ GeV. Both R values agree within statistical errors. The statistical error on the latter value is larger, a consequence of the smaller data sample used in finding it. The

Crystal Ball

CLEO

CUSB

LENA

DESY-Heidelberg

DASP-II

PLUTO

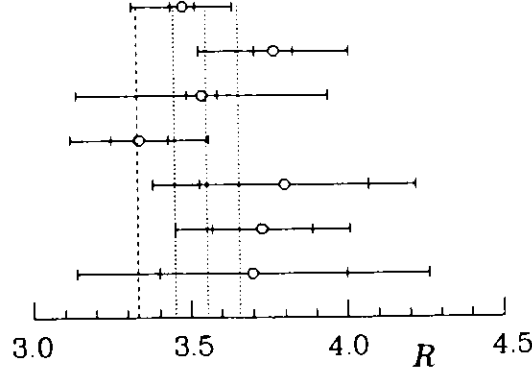


Figure 6.2: Compilation of R values. The small error bars represent statistical, the large error bars systematic errors, separately. The quoted values are measured at the following c.m. energies: Crystal Ball (this work) $W = 9.39$ GeV; CLEO [52] $W = 10.4$ GeV; CUSB [56] $W = 10.4$ GeV; LENA [3] $W = 9.30$ GeV; DESY-Heidelberg [42] $W = 9.45$ GeV; DASP II [57] $W = 9.5$ GeV; PLUTO [58] $W = 9.4$ GeV. For the lines see text.

systematic error is the same as discussed above.

The expected change in R when changing W from 9.39 GeV to 9.46 GeV, assuming a commonly used value for the QCD scale parameter $\Lambda = 300$ MeV, is of the order of $\Delta R/R \sim 10^{-4}$ and is thus not observable within our accuracy (the entire effect is caused by the running of α_s as can be seen from eqs. 6.3 and 6.6). So taking the weighted average of the two measurements we obtain

$$R = 3.48 \pm 0.03 \pm 0.14.$$

6.3 Discussion of the Results on R

A compilation of R values in the energy range $W = 9.3$ to 10.4 GeV is given in fig. 6.2. In this energy range no flavor threshold is crossed and changes in R due to the energy dependence of the strong coupling constant are unobservable within present statistics. Our result agrees with most of the published values within statistical errors. Our systematic uncertainty is considerably smaller than for the other measurements. The broken line shows the QCD prediction, assuming $\alpha_s = 0$, while dotted ones indicate the error-weighted average of R (including our point) and its error. We find for this average value of R

$$\langle R \rangle = 3.55 \pm 0.10. \quad (6.5)$$

The value of R is commonly thought to be a number from which QCD effects might be ideally deducted. The QCD corrections to the R value can be expanded as follows

$$R = R^0 \left(1 + A \frac{\alpha_s}{\pi} + B \frac{\alpha_s^2}{\pi^2} + C \frac{\alpha_s^3}{\pi^3} + \dots \right) \quad (6.6)$$

where we keep the convention that R^0 is the lowest order QCD prediction. The size of the QCD effect ϵ_{QCD} is then

$$\epsilon_{QCD} = \left(\frac{R}{R^0} - 1 \right) = A \frac{\alpha_s}{\pi} + B \frac{\alpha_s^2}{\pi^2} + C \frac{\alpha_s^3}{\pi^3} + \dots \quad (6.7)$$

Unluckily the effect is very small. Using our R value we get $\epsilon_{QCD} = 4.4\%$, while our systematic error is 3.9%. The effect is then on the limit of experimental sensitivity.

Unlike QED, QCD does not have a unique energy scale. The definition of the QCD scale depends on the renormalization scheme. In the following we will discuss the theoretical results calculated in the so-called \overline{MS} scheme. In this scheme the coefficient A of the expansion 6.6 is 1. In the lowest order α_s in the \overline{MS} scheme is given by

$$\alpha_s = \frac{12\pi}{(33 - 2n_f) \ln W^2/\Lambda_{\overline{MS}}^2} \quad (6.8)$$

with $\Lambda_{\overline{MS}}$ being a scale parameter. The choice of this parameter is not trivial. Note that in eq. 6.8 n_f is taken differently than for R (see eq. 2.8): in R the step in n_f occurs at $Q^2 = s = 4m_q^2$, where m_q is the quark mass, while in the \overline{MS} scheme the step occurs at $Q^2 = m_q^2$. Thus for the following calculations we have to take $n_f = 5$.

Ref. [11] suggests a procedure for scale fixing, such that the best convergence for a given process is achieved. The authors give a value of $B = 0.08$. Using their expansion for α_s in $\mathcal{O}(\alpha_s^3)$ we get

$$\alpha_s(Q^* = 0.71 M_T) = 0.138 \pm 0.037 \pm 0.131. \quad (6.9)$$

Higher order corrections $\mathcal{O}(\alpha_s^3)$ have been calculated [59] and turned out to be large. As given in [60] the coefficients B and C for $n_f = 5$ are

$$B = 1.411 \quad (6.10)$$

$$C = 64.86. \quad (6.11)$$

Inserting those values into eq. 6.6 we obtain

$$\alpha_s(Q^2 = M_T^2) = 0.120_{-0.029-0.114}^{+0.025-0.079}. \quad (6.12)$$

As stated before both results in eqs. 6.9 and 6.12 are completely dominated by the systematics although our measurement is the most precise one. Joining of data from different experiments diminishes the statistical errors, however, the systematic error estimation still remains a problem. Inserting eq. 6.5 into $\mathcal{O}(\alpha_s^3)$ formula we obtain

$$\alpha_s(Q^2 = M_T^2) = 0.163_{-0.064}^{+0.050}. \quad (6.13)$$

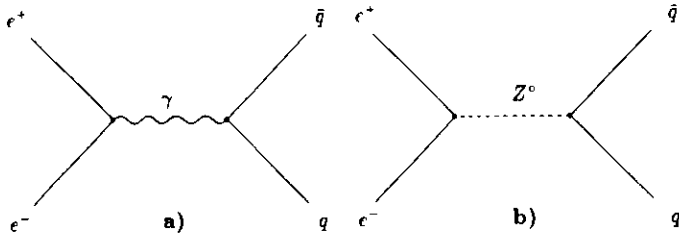


Figure 6.3: At high enough energies we will observe interference of diagrams (a) and (b).

The above result, although obtained by combining the data from several experiments, carries very large errors.

Recently, the precise measurement of R has become of interest [60,61]. The “desert”¹ found at PETRA and TRISTAN triggered physicists to search for prompt signals of particles predicted by electroweak theory. As we mentioned, R will be sensitive to any process leading to observed hadrons in the final state, i.e. any new particles coupling to hadrons will change the R value. At energies sufficiently large, the e^+e^- annihilation may lead to Z^0 production, with subsequent coupling to a quark pair as shown in fig. 6.3. Already at PETRA energies the electro-weak corrections to the total hadronic cross section caused by Z^0 exchange and/or due to production of the new particles should be observable, under the constraint that we are able to reduce the systematic errors. Recently two ideas have appeared which are of help in overcoming systematic problems. W. de Boer suggested that correlations between the experiments be included by means of off-diagonal elements in the correlation matrix [61]. A 1% correlation between different experiments was allowed. This is supposed to account, for example, for correlated systematics inferred by using the same prescription for radiative corrections etc.. The systematic and statistical errors were added in quadrature. The result is shown in fig. 6.4. Recently an update of this analysis appeared quoting a value of $\alpha_s(Q^2 = (34 \text{ GeV})^2) = 0.169 \pm 0.020$ [62]. A completely different procedure was used by R. Marshall [60]. The normalization of the experiments was allowed to change within their systematic errors, giving the fit function another degree of freedom. The result of this prescription is shown in fig. 6.5. Our result on R was included in both compilations.

¹Both PETRA and TRISTAN were built with the main purpose of finding and studying the toponium resonance. Instead the broad continuum with slowly-varying cross section was found.

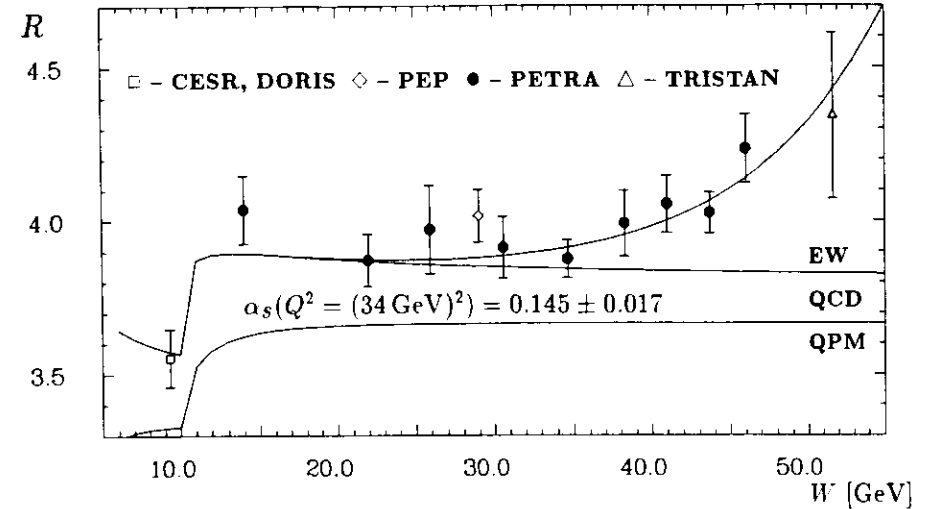


Figure 6.4: The ratio R measured at CESR, DORIS, PEP, PETRA and TRISTAN as a function of W . The errors shown include statistical and correlated normalization errors. The areas under theoretical curves correspond to using Quark Parton Model, QCD only and QCD plus electroweak effects (EW). The best fit to the data gives $\alpha_s(Q^2 = (34 \text{ GeV})^2) = 0.145 \pm 0.017$ for an assumed value $\sin^2 \theta_W = 0.23$. (from ref. [61]).

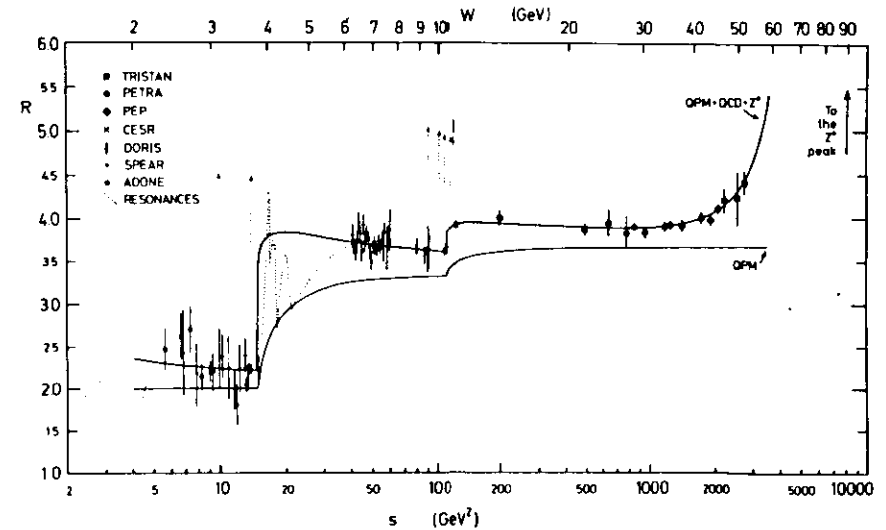


Figure 6.5: The ratio R measured at ADONE, CESR, DORIS, PEP, PETRA, SPEAR and TRISTAN as a function of W . The best fit gives $\alpha_s(Q^2 = (34 \text{ GeV})^2) = 0.135 \pm 0.012 \pm 0.010$ (from ref. [60]).

7. Summary

Using the data taken by the Crystal Ball Collaboration in the continuum below $\Upsilon(1S)$, we have determined the value of R —the ratio of the hadronic cross section to the Born cross section of μ pair production—at the c.m. energy $W = 9.39$ GeV, and find

$$R = 3.48 \pm 0.04 \pm 0.14.$$

Our value of R agrees within statistical errors with published results, and has the smallest systematic uncertainty. In spite of this precise result, we are not able to totally exclude the hypothesis $\alpha_s = 0$. The single experimental measurements of R are not able to deliver useful information about α_s . The results of such measurements are completely dominated by systematic effects given the smallness of the predicted QCD correction. The best way to determine α_s from measured R values is not yet agreed upon, resulting in a large spread of published α_s values; however, the simultaneous fit of the available R measurements allows the observation of the tail of the Z^0 in the total hadronic cross section at the highest PETRA and TRISTAN energies.

We also measured the leptonic partial widths Γ_{ee} of the $\Upsilon(1S)$ and $\Upsilon(2S)$ resonances. Using the prescription of Kuraev and Fadin [16] to correct for initial state radiation we find

$$\Gamma_{ee}(\Upsilon(1S)) = 1.34 \pm 0.03 \pm 0.06 \text{ keV},$$

$$\Gamma_{ee}(\Upsilon(2S)) = 0.56 \pm 0.04 \pm 0.02 \text{ keV}.$$

These values are the most precise single measurements yet obtained, and agree well with the averages of previous measurements rescaled to the radiative corrections of Kuraev and Fadin. Our results are $\sim 10\%$ higher than those already published mainly due to an internally consistent treatment of the radiative corrections. With these corrections the new world averages are

$$\Gamma_{ee}(\Upsilon(1S)) = 1.34 \pm 0.05 \text{ keV},$$

$$\Gamma_{ee}(\Upsilon(2S)) = 0.58 \pm 0.03 \text{ keV}.$$

To compare with theoretical predictions, the experimental Γ_{ee} values should be divided by 1.07 to factor out vacuum polarization. Using the current world averages for $B_{\mu\mu}$ (see table 5.3) we obtain the total widths

$$\Gamma_{tot}(\Upsilon(1S)) = 51 \pm 4 \text{ keV},$$

$$\Gamma_{tot}(\Upsilon(2S)) = 40 \pm 9 \text{ keV}.$$

Acknowledgements

The Crystal Ball experiment at DORIS-II, as all other high energy experiments, was possible only due to the joint effort of many people. I would like to thank all members of the Crystal Ball Collaboration for this effort and for years of friendly cooperation.

I will never forget the hospitality and help of Prof. J.K. Bienlein during my stays at DESY. He was always willing to discuss my physics problems. The same appreciation goes to Mrs. M. Bienlein.

I appreciate the assistance in writing up this thesis I have received from Prof. K. Rybicki.

The discussions with Drs. W. Koch and G. Nowak have resulted in many changes and general clarification of the text.

I would like to thank M. Reidenbach for a close collaboration and real friendship over these years.

Miss U. Rehder should receive special thanks for careful proof-reading.

I would like to thank the DESY directorate for its hospitality and financial support during the work on this thesis.

I am thankful to all my colleagues from High Energy Laboratory of the Cracow Institute of Nuclear Physics for friendship and support.

Finally, I would like to express appreciation to my wife, Malgosia, who continuously brought the sunshine and warmth into my everyday life.

Appendices

A. Monte Carlo Techniques

We measure physical processes only in a limited sensitive volume of the detector and only with some finite accuracy and efficiency. To get an apparatus-independent cross section σ (differential or total) we have to correct our measured results $\bar{\sigma}$ for the apparatus effects. These measured results can be expressed as the convolution of σ with the apparatus function G which depends on the arbitrary set of the observables $\Omega = (\omega_1, \dots, \omega_n)$

$$\bar{\sigma} = \sigma \otimes G(\Omega). \quad (\text{A.1})$$

The particular choice of G and Ω is of course problem-dependent. In principle it is possible to calculate the analytical formula for the function G ; however, in practice the complication of such an approach makes it unreasonable. A different approach to calculate the convolution integral is based on the Monte Carlo technique. We know the basic processes, for example phenomena leading to energy deposition, particle production and their corresponding probabilities. The Monte Carlo program uses this input to simulate the complex processes by selecting the basic processes with their given probabilities.

A.1 Event Simulation

The organization of the Crystal Ball Monte Carlo is shown in fig. A.1. We subdivide the process of the event generation into two steps: modeling of the physical process (referred to as STEP1) and simulation of the detector response (referred to as STEP2). The models used for the simulation of physical processes are described already in sect. 4.2. A convenient feature is the compatibility of STEP1 and STEP2 files—the output of the STEP2 contains still STEP1 information and can be used again as input in case one wants to test different assumptions for the detector response.

The detector response for the electromagnetically showering particles is simulated by the EGS 3 code [32] while the hadronic interactions are simulated with use of the GHEISHA 6 [33] program. The author was involved in the initial implementation of GHEISHA into the framework of the Crystal Ball Monte Carlo [63]; later he became responsible for this simulation. It is worth mentioning here that we use a common geometry for EGS and GHEISHA. We have rewritten the GHEISHA geometry routines in order to use the EGS style geometry for reasons discussed later in section A.3.1.

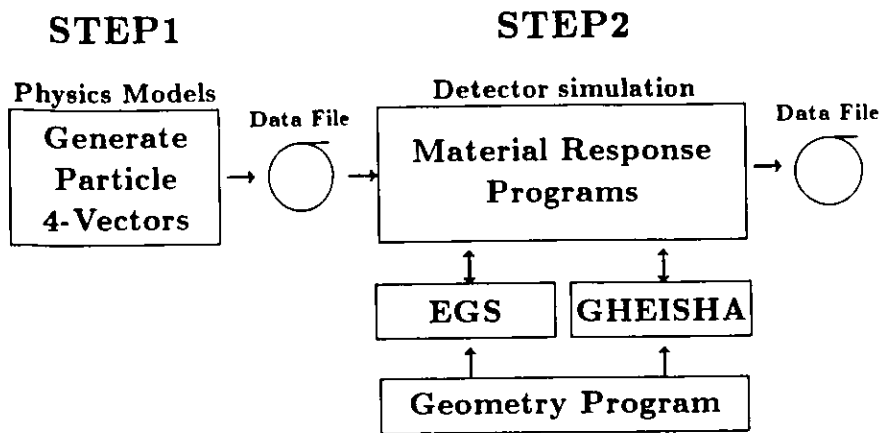


Figure A.1: The organization chart of Crystal Ball Monte Carlo.

A.2 On Monte Carlo Testing Techniques

The testing of the detector Monte Carlo for most experiments causes difficulties because of the complexity and usually large size of the simulation program. An additional problem comes from the computer time needed for the simulation. The time necessary to simulate a single event is large, approaching several seconds of CPU time on an IBM series 3000 processor.

Let us start from the detector geometry, i.e. the part of the code supplied normally by the user. It helps to start with a simple check such as plotting the input geometry. This is a reassuring method with which one can find inconsistencies. Means for this purpose are available in the GEANT [64] apparatus Monte Carlo program, in the form of the ZEBRA graphic package. The GHEISHA program alone, however, does not support this feature. The author has written a simple program allowing for 3-D images. The plots like 3.3, 3.5 or A.2 were produced using this program with geometry input of the Monte Carlo.

It is worthwhile to mention here two other ideas which can be useful.

The first one is the application of computer graphics in debugging the geometry code. Both GHEISHA and EGS are based on a stepping principle. The step size is limited to a certain percentage of radiation or interaction lengths in order to guarantee a proper simulation of the secondary processes. Additionally, one has to reduce the step size so that the step does not pass the boundary of the medium. Plotting the points where the program asks geometry routines for new input should then provide a clear image of the apparatus. This is demonstrated in figs. A.2 and A.3. The example of a debugging output is shown in fig. A.4. Points outside the images of the crystals or places appearing particularly "dirty" indicate the

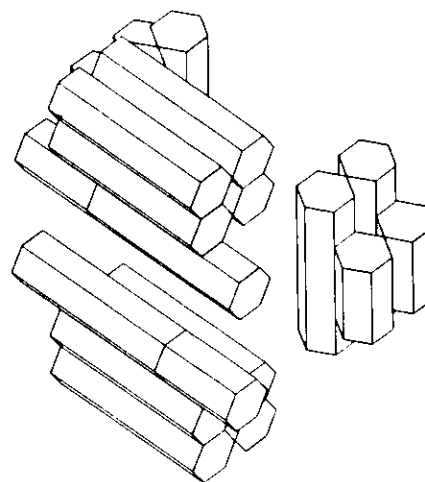


Figure A.2: 3-D view of the +z endcaps.

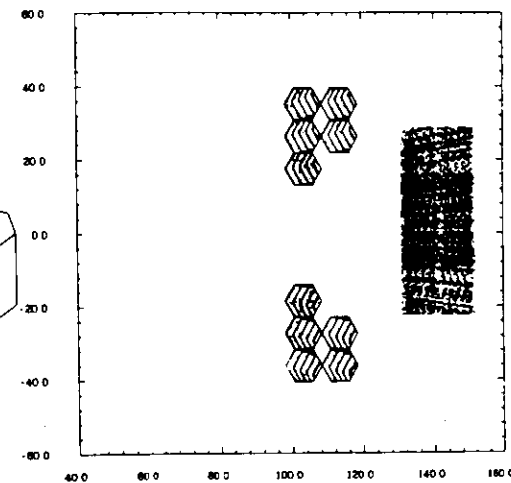


Figure A.3: The projection of fig. A.2. For the details see text.

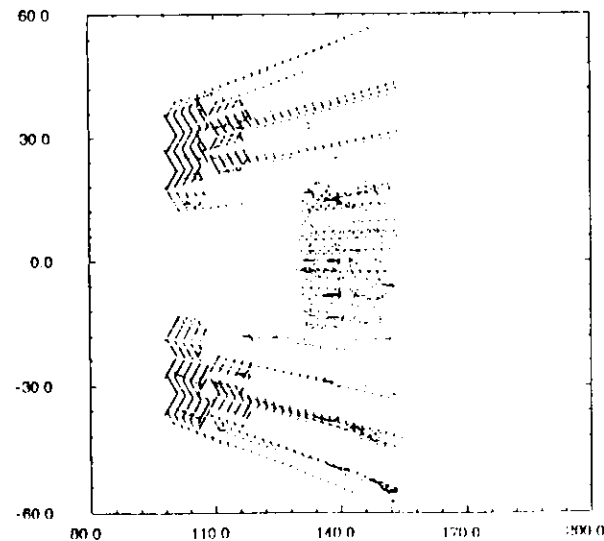


Figure A.4: Debugging example. The picture shows exactly the same part of apparatus as A.3. Points leaking outside the shape of crystals or places appearing particularly "dirty" indicate the problems in the geometry routines.

problems in the geometry routines. The regular structure reflects the step size limitations. The boundaries produced directly by GHEISHA will be fuzzy, reflecting the effects of the way multiple scattering is simulated (see section A.3.3).

The second idea is also presented in fig. A.3. It was produced without EGS/GHEISHA, just using a "stepping simulator". The idea is to have a small program that simulates stepping, i.e. offers step size and direction to the geometry routine which is to be tested. The program is very fast and allows working with large samples, thus allowing the detection of even subtle effects in a reasonable amount of time.

Because the Crystal Ball does not have a particle identification system, we can perform only a few tests of simulation of particle interactions. Luckily, nature offers us one well suited tool for detector tests—muons. They have an easily distinguishable experimental signature, deposit their energy mainly by pure ionization loss and, moreover, are generally available as a main component of cosmic rays. Due to the saturation effects in the energy deposition for highly relativistic particles (i.e. for $\beta\gamma \geq 50$ the dE/dx changes very slowly) we were able to use cosmic μ 's sample for the early tests. In the following we have used muons produced in the process $e^+e^- \rightarrow \mu^+\mu^-(\gamma)$. We also obtained results from test measurements performed on pion beams (both π^+ and π^-) at CERN, done with a test setup built of exactly the same NaI(Tl) crystals as the Crystal Ball detector [65]. With help of these measurements we were able to trace differences observed in variables describing multihadronic events globally back to problems in the simulation of hadronic interactions.

A.3 Changes of the GHEISHA Code

The standard version of the GHEISHA code fails to describe our data [63,66]. Figs. A.5–A.8 show the most striking disagreements. Fig. A.5 shows the simulated detector response to monoenergetic 5 GeV muons. The shape of the energy deposition is purely Gaussian although the Landau shape of the energy deposition in each step was used in simulation. Let us now define the momentum tensor $Q^{\alpha\beta}$

$$Q^{\alpha\beta} = \sum_{i=1}^N \vec{p}_i^2 \xi^{\alpha\beta} - p_i^\alpha p_i^\beta \quad (\text{A.2})$$

where $\vec{p} = (p^x, p^y, p^z)$ is the momentum vector found as the product of the energy deposited in the crystal and the unit vector of the crystal axis. The sum runs over all illuminated ball crystals (N). For discussion of this procedure see sect. 3.4. The smallest eigenvalue obtained by diagonalizing the tensor $Q^{\alpha\beta}$ is called in our plots p_{T-jet}^2 . The Monte Carlo prediction for p_{T-jet}^2 is shown in fig. A.6 together with the one found for the hadronic data taken in the continuum at $W = 9.39$ GeV. We also present the input distribution calculated after fragmentation using the momenta of generated particles. We started by investigating the input p_T distribution, used for the event generation, that seems to be most naturally

correlated with our definition of p_{T-jet}^2 . In order to obtain agreement with the data we would have to shift the input width σ of p_T^2 ($2\sigma^2 = \langle p_T^2 \rangle$) used in the LUND fragmentation scheme from 400 MeV to 150 MeV. To get a similar agreement for the Y(1S) resonance data we have to make an even more dramatic change—to the level of 50 MeV. Such dramatic disagreement suggests severe problems.

Fig. A.7 shows the distribution of the cluster energy of multihadronic events at $W = 9.39$ GeV. The Monte Carlo distribution is shifted towards higher energies.

These two facts suggest that the energy deposited away from the jet axis is overestimated. Fig. A.8 gives a hint where the main problem lies. It shows the distribution of the cluster energy, subject to the condition that the negative pions are not allowed to interact strongly after stopping. A much better agreement between the data and the Monte Carlo is observed.

To obtain agreement with the data we have inspected and modified the GHEISHA code. The Crystal Ball calorimeter is somehow special, consisting only of an *active medium*. The inspection of the particle spectra generated by the physical models shows that it is very important for us to treat stopping particles correctly; this was not the case in the standard GHEISHA. Below we will inspect the changes made to the standard GHEISHA. The sections on dE/dx and multiple scattering modifications are given here to complete the overview. The recent work on these subjects was done by M. Kobel [67].

A.3.1 Geometry Routines

Let us start by considering the requirements our geometry program should fulfill. The Crystal Ball measures the energy deposited in the calorimeter down to $\mathcal{O}(1$ MeV) (crystals with energy above 0.35 MeV are used in the analysis). The minimum-ionizing particles deposit typically ~ 5 MeV/cm in NaI. From this it follows that for a single minimum-ionizing track a precision (in finding the step size) of $\epsilon \sim 1-2$ mm of the geometry program will suffice. The situation changes dramatically if the particle showers and/or the energy loss becomes large. If an average of $\langle n_{sh} \rangle$ particles in a shower are produced, the precision should be increased by $\langle n_{sh} \rangle$ i.e.

$$\tilde{\epsilon} = \frac{\epsilon}{\langle n_{sh} \rangle}. \quad (\text{A.3})$$

Note that in case of large variation of n_{sh} one has to pursue the maximum possible number of shower branches in order to avoid trouble with the energy resolution. An increase of the precision should be considered also in case of heavily ionizing particles or those which traverse dense media. The geometrical precision gains additional importance for finely segmented calorimeters. It will be very convenient and elegant to have the same geometry input for all kinds of particles. All this reinforces the requirement that the speed of the geometry routines must be as high as possible since this part of code is most heavily used—small inefficiencies produce big waste of CPU time. Summarizing, we can formulate our requirements as follows:

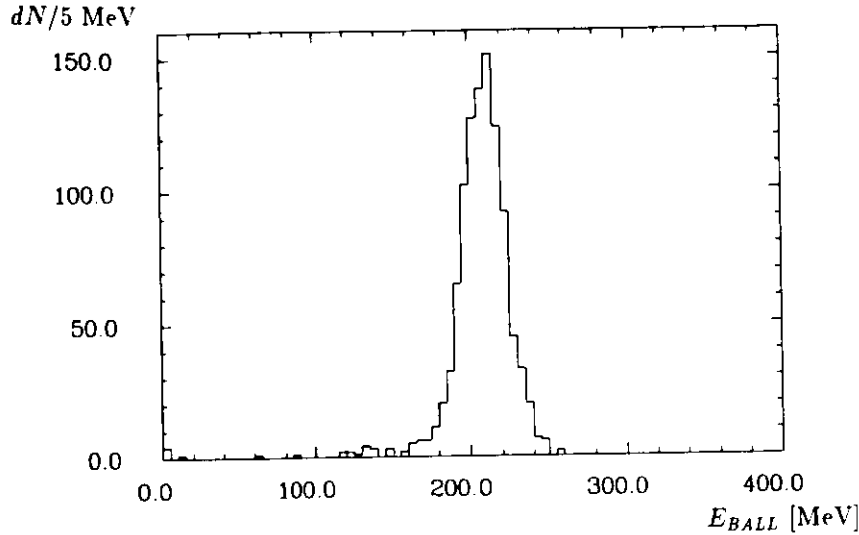


Figure A.5: The total energy spectrum of 5 GeV/c μ^- generated by the default Monte Carlo simulation. The shape of the energy deposition is purely Gaussian (to be compared with A.11).

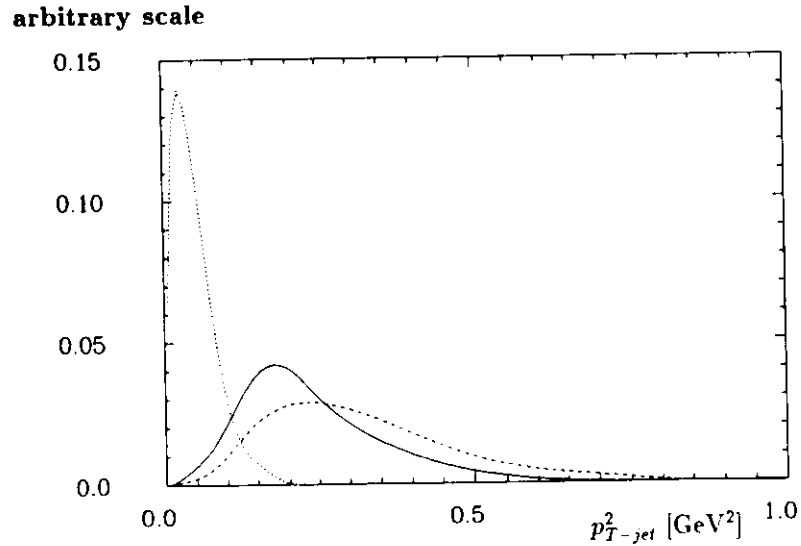


Figure A.6: The p_{T-jet}^2 distribution for the continuum data. Continuous curve shows the data, the dotted one the input distribution after fragmentation, and the dashed line marks the default Monte Carlo prediction.

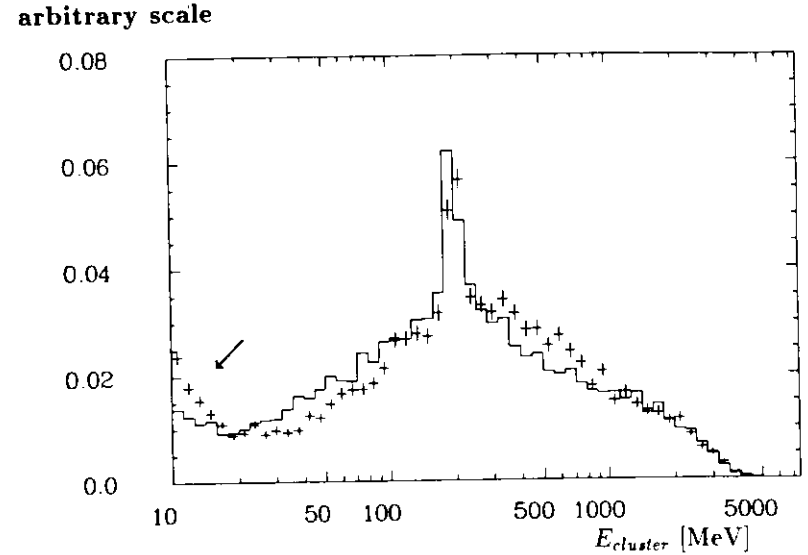


Figure A.7: The distribution of $E_{cluster}$. The data are represented by the histogram. The crosses are the result of the Monte Carlo simulation. The peak at ~ 200 MeV is due to the purely ionizing particles. For the arrow see text.

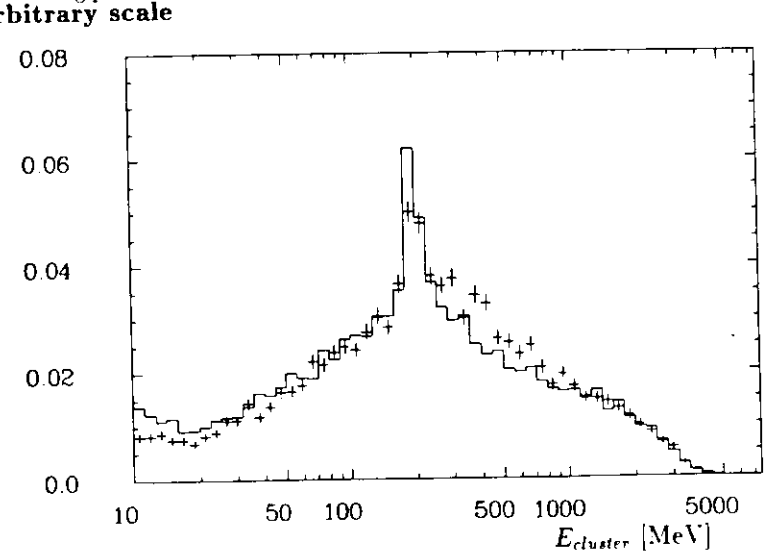


Figure A.8: The distribution of $E_{cluster}$. The data are represented by the histogram. The crosses are the result of Monte Carlo simulation. Negative pions are not allowed to interact strongly after stopping.

1. the geometry routines should be as precise as possible to avoid systematic problems;
2. the geometry input should be common for EGS and GHEISHA;
3. these parts of the code should be as fast as possible and the information delivered by the geometry routines should be handled very efficiently.

Let us now show how in practice the coordinates inside the calorimeter are mapped into symbolic "calorimeter cells". The geometry routines of GHEISHA deliver the number of the "calorimeter cell" or find the number of the "neighboring cell", using the actual coordinates as a starting point. This essentially "hit or miss" information is then used to find using the Newton method "how far we can go" i.e. how far the particle can be transported without crossing the medium boundary. EGS requests more detailed information since we have not only to answer "how far we can go" but also what is the distance to the closest medium boundary ("cell"). Our experiences with the simple geometry in the GHEISHA treatment revealed a large computing inefficiency in this approach. We gain a factor of ~ 2 in the CPU time by using the EGS style geometry. This can be understood from the fact that the typical step sizes requested by the EGS are ~ 2.5 cm (in our case the total time of the simulation is dominated by the time spent inside the EGS). Requiring an accuracy of only $\bar{\epsilon} = 0.01$ cm, we have to make ~ 8 iterations in order to achieve the desired accuracy. An extra inefficiency is imposed by multiple scattering because we have to repeat the iteration process once again. This inefficiency is connected with the discontinuous approximation of the multiple scattering. After these experiences we have rewritten the GHEISHA geometry routine so that we can use the EGS style geometry interface. (This also saved much manpower as we already had the geometry interface to EGS.) Our changes essentially agree with the recommendation of the authors of the EGS, i.e. use of the geometry input should be reduced as much as possible. After making sure that the geometry routines are working correctly we can start further tests.

A.3.2 Checking of the dE/dx Constants

The ionization losses are taken into account using the Bethe-Bloch formula with the Sternheimer density correction [68]. The mean value of the dE/dx energy loss is given by

$$-\frac{dE}{dx} = \left(\frac{2\pi e^4}{m_e}\right) n Z_{inc}^2 \frac{1}{\beta^2} \left(\ln \frac{2m_e w_{max}}{I^2} + \ln \frac{\beta^2}{1-\beta^2} - 2\beta^2 - \delta \right) \quad (A.4)$$

$$= D \left[\ln \left(\frac{2m_e w_{max}}{I^2} \beta^2 \gamma^2 \right) - 2\beta^2 - \delta \right] \quad (A.5)$$

where w_{max} is the maximum kinetic energy for δ -rays, Z_{inc} the charge of the incident particle, I the mean ionization potential of the material traversed, and δ the density effect correction as described later. The w_{max} is given by [55]

$$w_{max} = \frac{2m_e \beta^2 \gamma^2}{1 + 2\gamma m_e / m_{inc} + (m_e / m_{inc})^2} \quad (A.6)$$

where m_{inc} is the mass of the incident projectile. The electron density n is defined as

$$n = N_A \rho \frac{Z}{A} \quad (A.7)$$

with N_A being the Avogadro number, ρ , Z and A the density, the charge and atomic number of the traversed medium. This correction δ was expressed by Sternheimer [69] as follows

$$\begin{aligned} \delta &= 0 & X < X_0 \\ \delta &= \ln(\beta^2 \gamma^2) + C + a(X_1 - X)^m & X_0 < X < X_1 \\ \delta &= \ln(\beta^2 \gamma^2) + C & X_1 < X \end{aligned} \quad (A.8)$$

with $X = \log \beta^2 \gamma^2$ and C , a , m , X_0 , X_1 the Sternheimer parameters. The number of parameters can be reduced. The parameters a , m , X_0 , and X_1 can be expressed as a function of C and the state of the medium [68]. The parameter C can be calculated from the experimentally measured value of I . The parameter a can be found using the boundary conditions from eq. A.8.

In practice we measure the energy deposition in some material layer. Traversing thickness t we expect that the most probable energy loss dE will be:

$$-dE = Dt \left[\ln \left(\frac{2m_e Dt}{I^2} \beta^2 \gamma^2 \right) - \beta^2 + 0.198 - \delta \right] \quad (A.9)$$

The above formula is valid for $dE \ll E$. Fig. A.9 shows the theoretical predictions for the most probable energy deposition in the Ball crystal in case when a muon traverses a NaI(Tl) crystal along its long axis (see fig. 3.4). Muons with $\beta\gamma \lesssim 3$ will range out and deposit their total kinetic energy (solid curve in the first region of fig. A.9). Within the 300 ns Crystal Ball trigger gate we also see the energy from muon decay in $\sim 13\%$ of the cases, and in case of negatively charged muons the absorption on a nucleus followed by soft γ emission. In the second region we start to punch through the ball. The formula A.9 is not valid in this region (dashed-dotted line). We can use the formula A.4 instead. In this case the mean energy loss (dashed line) will be a good approximation to the most probable energy loss because the w_{max} value is very low. Thus no high-energy tail will be present in the dE distribution. In the third region the formula A.9 can be safely used.

The application of eq. A.9 directly in the simulation leads to problems. The energy in the Monte Carlo is deposited in many small steps. The central limit theorem tells us that this will lead to a Gaussian shape of the energy deposits as the final simulation result (for a large enough number of steps). The long high-energy tail of the dE/dx distribution is caused by δ -ray production. Use of Landau distribution in each step might give a correct numerical value but will not reproduce the lateral behavior of energy deposition. The problem was resolved as follows: We used the restricted energy loss according to the formula:

$$-dE/dx = D \left[\ln \left(\frac{2m_e w_{cut}}{I^2} \beta^2 \gamma^2 \right) - \beta^2 - \delta \right] \quad (A.10)$$

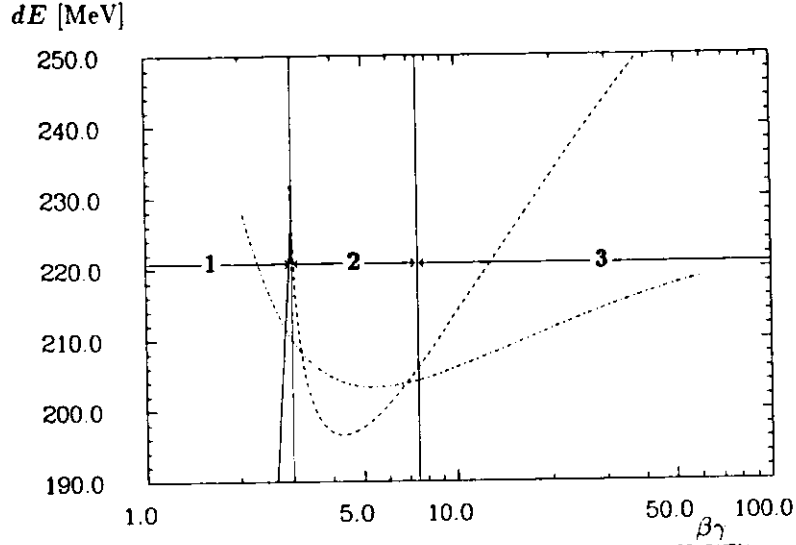


Figure A.9: The theoretical prediction for the energy deposited by muons in NaI(Tl) assuming that the muon passes through the crystal along its axis. For the detailed description see text.

valid for $w_{cut} \ll w_{max}$. The δ -rays are produced when $dE > w_{cut}$. The ejection angle of the δ -ray is given by:

$$\cos \theta = \frac{(E_{inc} + m_e)(E_e - m_e)}{p_{inc} p_e} = \left(1 + \frac{1}{\gamma} \frac{m_e}{m_{inc}}\right) \frac{1}{\beta} \sqrt{\frac{w_e}{w_e + 2m_e^2}}. \quad (\text{A.11})$$

In this formula w and E are kinetic and total energy, respectively. The subscripts 'e' refer to the δ -rays and 'inc' to the incoming projectile. Standard GHEISHA uses the following formula:

$$\cos \theta = \sqrt{\frac{w_e}{w_{max}}} \quad (\text{A.12})$$

with:

$$w_{max} = 2m_e \beta^2 \gamma^2 \quad (\text{A.13})$$

rather than the value according to A.6. With the substitution of A.13, A.12 approaches the exact value A.11 in the non-relativistic limit.

Our strategy was to check the theoretical predictions using data. The initial GHEISHA 6 code produces an energy deposition of essentially Gaussian shape because of the already mentioned limitations imposed by the central limit theorem. The δ -rays were produced only for liquid argon and not for NaI. The code was changed so that it produces the δ -rays for all media and the material constants were replaced by the published Sternheimer values. The comparison of the selected muon data sample with the default and the improved Monte Carlo code is shown in figs. A.10 and A.11, respectively. The best agreement between data and

Monte Carlo is achieved when we use the value of the Sternheimer parameter $C = -6.057$ as given in ref. [70].

A.3.3 Multiple Scattering

Muons can also serve as test data for the optimization of multiple scattering parameters, just as they did for the Sternheimer parameters. The fine detector granularity allows measurement of the lateral energy distribution. This energy pattern is sensitive to multiple scattering, but unluckily, also to δ -ray production.

There are two important observations: (a) it is not necessary to simulate single scattering in order to describe the data; (b) the particular method of simulating multiple scattering is a source of large CPU inefficiencies in GHEISHA. The simulation of the multiple scattering by imposing an angular spread of the particle momentum and the displacement in plane perpendicular to the particle momentum is not well suited for the Monte Carlo simulation. This creates a discontinuous particle path. EGS uses a continuous approach to this problem [32]. To our knowledge, a similar approach for the particles other than electrons has not been developed. For completeness let us here review briefly the formulas as used in the GHEISHA program.

Multiple scattering is usually described by the scattering angle projected on two perpendicular planes (each referred to as projected angle) and the positional shift in the plane perpendicular to the particle momentum. The root mean square projected scattering angle for the particle with momentum p traversing the path t in the medium with the radiation length X_0 is [55]:

$$\theta_0 = \frac{14.1 \text{ MeV}/c}{p\beta} Z_{inc} \sqrt{\frac{t}{X_0}} \left(1 + \frac{1}{9} \log(t/X_0)\right) \quad [\text{radians}]. \quad (\text{A.14})$$

The multiple scattering probability is Gaussian in the reduced projected angle $\alpha = \theta/\theta_0$ thus given by

$$p(\alpha) d\alpha = \frac{1}{\sqrt{2\pi}} e^{-\alpha^2/2} d\alpha. \quad (\text{A.15})$$

Additionally, in order to obtain a better description of the data, we have simulated a single scattering (not simulated in standard GHEISHA) with the probability given by [71]

$$p(\alpha) d\alpha = \frac{1}{4 \ln(210Z^{-1.75})} \frac{d\alpha}{\alpha^3}. \quad (\text{A.16})$$

The displacement in the plane perpendicular to the momentum of the incident particle is also Gaussian with the spread y : [55]:

$$y_0 = \frac{1}{\sqrt{3}} t \theta_0. \quad (\text{A.17})$$

Ref. [55] gives the following formulas, under the assumption that z_1 and z_2 are independent Gaussian random variables with mean zero and unit variance, used to obtain the actual values

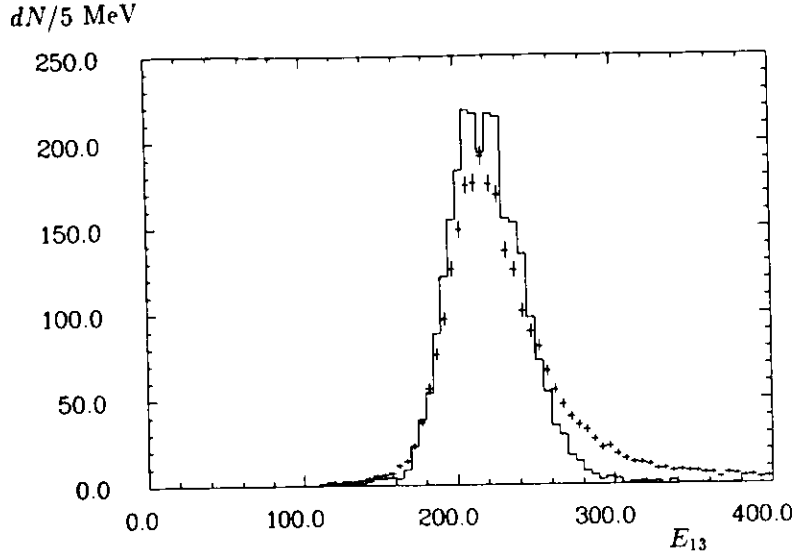


Figure A.10: The comparison of the energy deposited in the Ball by μ 's produced in the reaction $e^+e^- \rightarrow \mu^+\mu^-(\gamma)$. The crosses represent the data, and the histogram the default Monte Carlo (here: width and peak position adjusted to fit the data), normalized to the number of data entries.

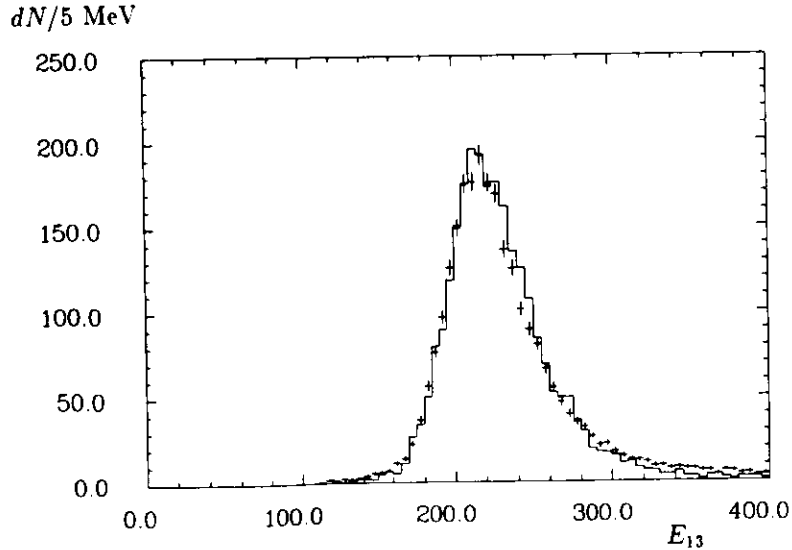


Figure A.11: The comparison of the energy deposited in the Ball by μ 's produced in the reaction $e^+e^- \rightarrow \mu^+\mu^-(\gamma)$. The crosses represent the data, and the histogram the corrected Monte Carlo normalized to the number of data entries.

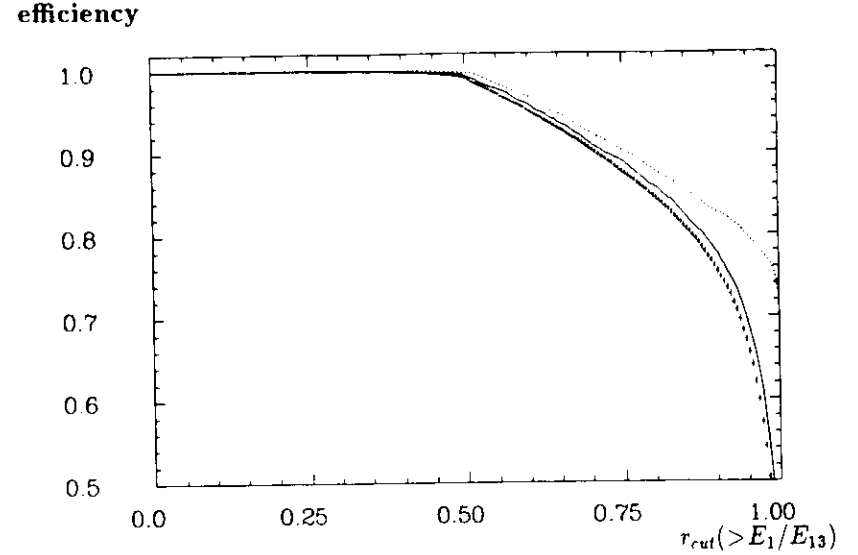


Figure A.12: Muon identification probability as a function of the acceptance cut $r_{cut} > \tau = E_1/E_{13}$. The crosses show the data, the dotted line shows the standard GHEISHA simulation and the continuous line the effect of our changes.

of scattering angle θ and the displacement y :

$$\theta = z_1\theta_0 \quad (\text{A.18})$$

$$y = \frac{1}{2}z_1t\theta_0 + \frac{1}{\sqrt{12}}z_2t\theta_0 \quad (\text{A.19})$$

GHEISHA does not account properly for the correlation between the generated scattering angle and the displacement because the second term of A.19 is omitted in the generation.

The effect of the changes on the lateral energy pattern is shown in fig. A.12. There we show the reduction in the efficiency for finding a muon when the cut on energy ratio E_1/E_{13} is tightened (see section 3.4). The agreement between data and Monte Carlo has improved with our modifications, stemming mainly from the proper simulation of δ -rays. Multiple scattering has only a weak influence on the lateral energy pattern.

A.3.4 Absorption of Negatively Charged Particles

Positively charged particles stopping in matter simply decay because the Coulomb barrier between the particle and the nucleus prevents nuclear interactions. For slow negatively charged particles (π^- , K^- , Σ^- , ... etc.) the dominant process is the absorption by nuclei. The Crystal Ball detector response simulation is particularly sensitive to the pion and kaon

absorption, as these are the most frequently produced particles. We expect to find on average about eight charged pions and one charged kaon in a multihadron event at c.m. energies around 10 GeV.

Data from a test setup [65] built of exactly the same NaI crystals as the Crystal Ball detector were used for a comparison with the GHEISHA simulation. The test module was exposed to 200 MeV/c positively and negatively charged pions which stop in the detector. The experimental data of figs. A.13 and A.14 show a large disagreement with the GHEISHA simulation (figs. A.15 and A.16) for negative pions while the positive pions agree reasonably. Although the scales differ (MeV and "ADC channels"), the comparison contains an important message: For π^+ and π^- the measured energy depositions peak at the kinetic energy of the incident particles, whereas the Monte Carlo predicts for stopping π^- mesons a peak at the total energy of the incident particle. This indicates a serious shortcoming in the simulation code. For a proper simulation we need precise experimental data including not only the measurement of the total energy deposition but also of particle multiplicities and energy spectra in π^- absorption processes. Such a measurement was done in connection with a recent cancer therapy study [72] at SIN in Switzerland. The experimental results can be summarized as follows:

1. only $\sim 75\%$ of the pion mass is available for the kinetic energy of the particles emitted after the absorption process. The rest goes into binding energy.
2. most of the energy is carried away by neutrons (see table A.1).
3. the momentum spectra can be parametrized approximately by an exponential function: $\sim \exp(-pc/200 \text{ MeV})$.

An important number is the ratio 5 : 1 between the number of neutrons and protons. The GHEISHA parametrization assumes this ratio to be $\sim 1 : 1$. Additionally, the ratio of protons to heavy fragments was overestimated and the entire mass of the π^- was assumed to be available for the kinetic energy of the produced particles.

This allows for a qualitative understanding of the discrepancies between our data and the GHEISHA predictions for the p_{T-jet}^2 distributions. Particles with large p_T^2 usually have lower energy and are stopping. GHEISHA releases a too large fraction of their energy to too many charged secondary particles. This overestimates our measured $\langle p_{T-jet}^2 \rangle$ in the Monte Carlo simulation. The effect is enhanced by the missing simulation of light quenching in NaI (see sect. A.3.5 below).

The absorption routine PIMABS was completely rewritten using the measured experimental input. Due to the hermetic structure of the GHEISHA program, allowing for production of fragments heavier than He, is not trivial. We decided to generate all fragments as given in table A.1 but afterwards to exclude fragments heavier than He from further tracking. This

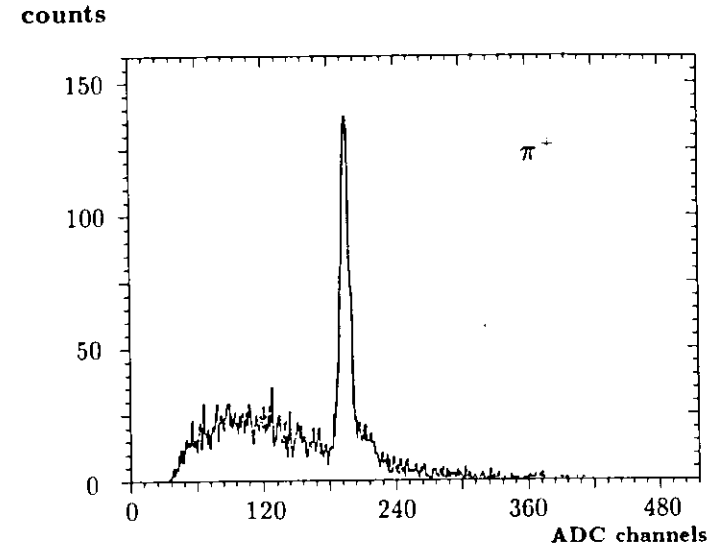


Figure A.13: The pulse height spectrum for 200 MeV/c π^+ in a NaI(Tl) crystal test setup as measured by [65].

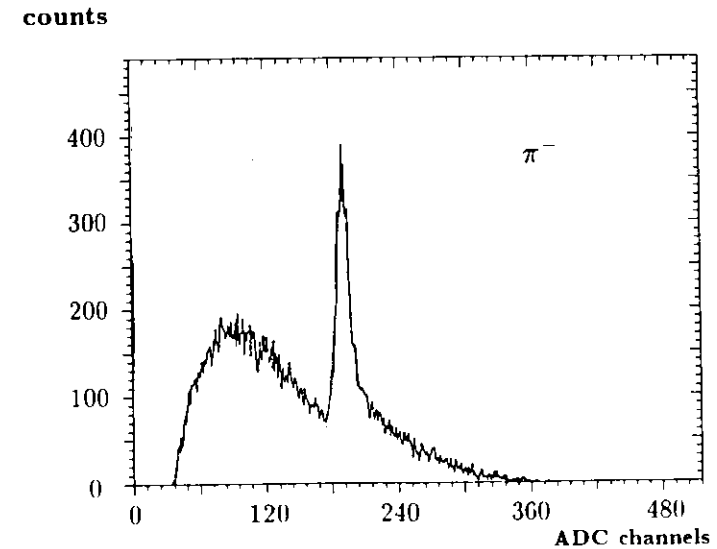


Figure A.14: The pulse height spectrum for 200 MeV/c π^- in a NaI(Tl) crystal test setup as measured by [65].

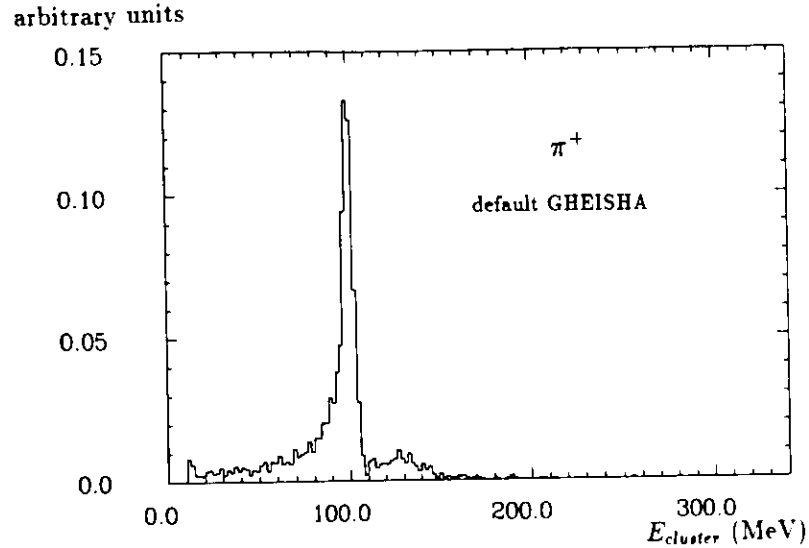


Figure A.15: Default Monte Carlo prediction for the energy distribution of all clusters created by 200 MeV/c π^+ stopping in the Crystal Ball. One pion may give more than one entry.

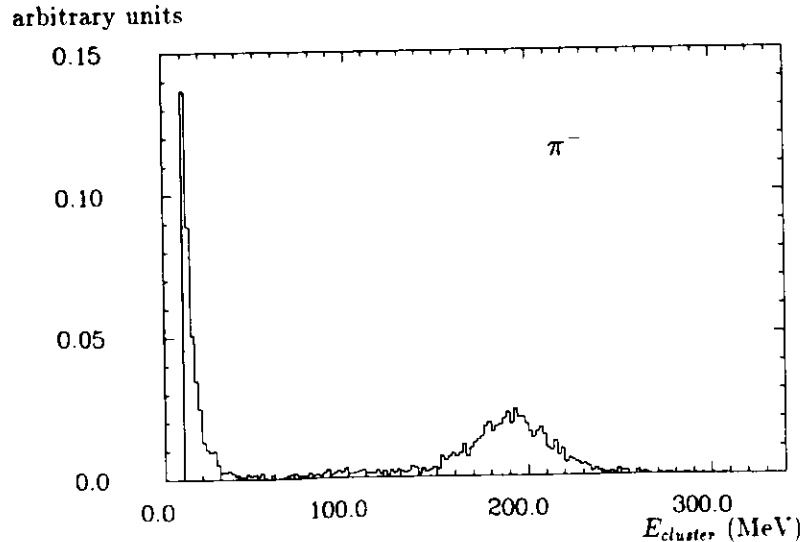


Figure A.16: Default Monte Carlo prediction for the energy distribution of all clusters created by 200 MeV/c π^- stopping in the Crystal Ball. One pion may give more than one entry.

Table A.1: Features of particle production in the process of π^- absorption on ^{12}C according to ref. [72].

Particle type	Average multiplicity per π^- stop	Average released kinetic energy per π^- stop [MeV]
n	2.5	76.0
p	0.485	10.4
d	0.356	6.3
t	0.249	3.0
He	0.84	6.2
Li ⁶	0.12	0.8
Li ⁷	0.12	0.8

decision is motivated by the low abundances of the heavy fragments and the observation that the measured energy deposition of heavy fragments will be suppressed by light quenching in the scintillator. To our knowledge the dependence of the absorption process on the mass of the nucleus was studied neither experimentally nor theoretically. We decided to use directly the results on ^{12}C [72].

The comparison of the visible energy spectrum obtained with the modified π^- absorption routine with the test measurement [65] is shown in fig. A.17. The distributions have been normalized to each other to agree in peak height. The energy scale of the test data has been set with the help of the π^- peak positions. The continuous line shows the shape of the experimental distribution (the same as in fig. A.14), while the crosses indicate the results of the simulation. It now gives the peak in the π^- spectrum at the expected position.

However, we still observe clear differences above and below the peak region. As will be discussed in more detail in sect. A.3.6, the simulated range of neutrons is underestimated, and the photons emitted in neutron capture are too energetic in GHEISHA. Thus the neutrons contribute more energy to the π^- clusters than in reality. In addition those neutrons, which leave the π^- cluster region, may create additional low energy clusters when they are captured further away. Those additional clusters clearly show up as a peak at low cluster energies in figs. A.16 and A.17. As a first test of this assumptions we excluded the neutrons from tracking, which results in fig. A.18. Now also the energy depositions above the peak are well described. The broad enhancement below the peak in the measured distribution cannot be explained. It might well be due to beam impurities since muons from the decay of 200 MeV/c pions have a kinetic energy of several 10 MeV.

Similar problems occur in the treatment of stopping K^- . Negative kaons can form hypernuclei or produce other strange particles. The assumption of GHEISHA, to perform only $K^-p \rightarrow \Lambda\pi^0$ and $K^-p \rightarrow \Lambda\gamma$ in K^- absorption, is again too crude. Table A.2 (from [73]) shows the complexity of the processes following negative kaon absorption. We used these

arbitrary units

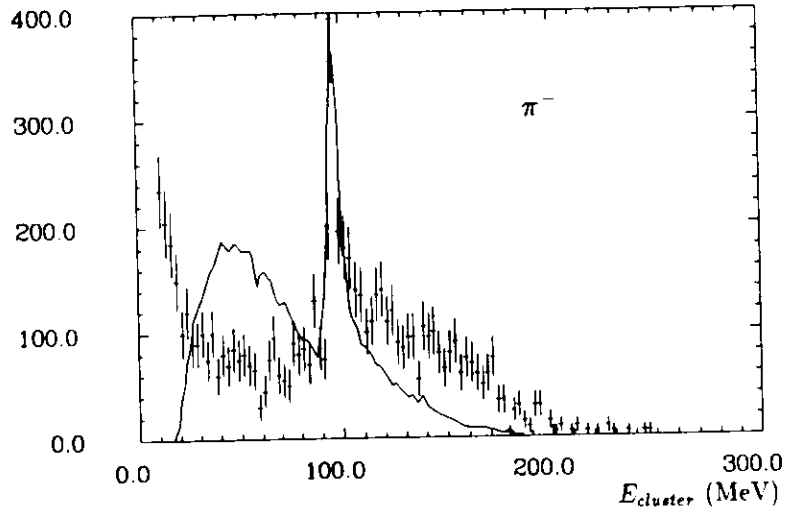


Figure A.17: Comparison of the simulated cluster energy spectrum for stopping π^- (crosses), obtained with the modified absorption routine PIMABS and default neutron tracking, with the measured one from [65] (solid curve).

arbitrary units

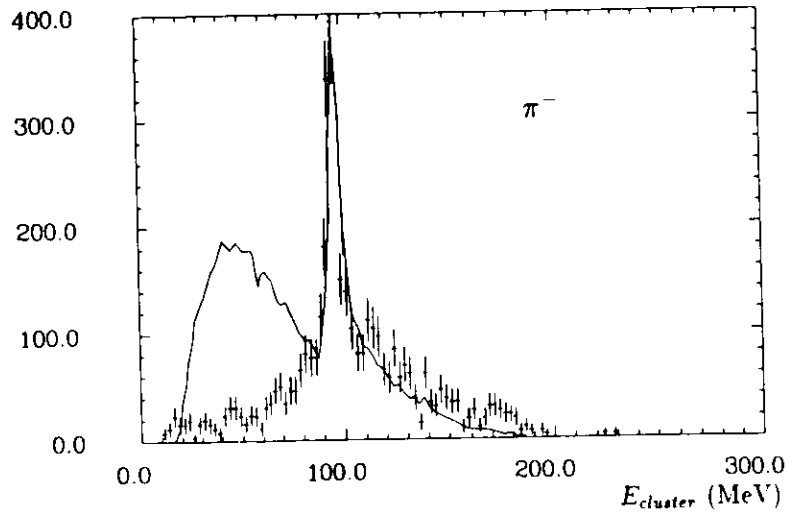


Figure A.18: Comparison of the simulated cluster energy spectrum for stopping π^- (crosses), obtained with the modified absorption routine PIMABS and neutrons excluded from tracking, with the measured one from [65] (solid curve).

Table A.2: Elementary processes for pion and hyperon production from K^- absorption [73].

	Initial state	Final state	Branching ratio in %
Production	$K^- + p$	$\Sigma^+ + \pi^-$	22
		$\Sigma^0 + \pi^0$	28
		$\Sigma^- + \pi^+$	44
		$\Lambda + \pi^0$	6
	$K^- + n$	$\Sigma^0 + \pi^-$	30
		$\Sigma^- + \pi^0$	30
		$\Lambda + \pi^-$	40
	$K^- + NN$	$\Sigma^+ + N$	33
		$\Sigma^0 + N$	33
$\Sigma^- + N$		33	
Decay	Free Σ^+	$n + \pi^+$	48
		$p + \pi^0$	52
	Free Σ^0	$\Lambda + \gamma$	100
	Free Σ^-	$n + \pi^-$	60
		absorption	40
	Free Λ	$n + \pi^0$	36
		$p + \pi^-$	64

probabilities to simulate negative kaon absorption in the routine KMABS, assuming that the absorption process takes place as on free p , n , and two-nucleon aggregates (NN). The numbers are normalized such that the branching ratios for $K^- p$, $K^- NN$, and $K^- n$ add up to 100% each. The process of K^- absorption on two-nucleon aggregates has a probability rather independent of the target used and contributes about 20% to the total absorption rate for targets heavier than deuterium [73]. The relative probability for the absorption taking place on a single neutron or proton within the nucleus is taken to be equal to the $(A - Z)/Z$ ratio. Formation of hypernuclei was not simulated.

The main result of this treatment is that not only neutral but also charged pions are directly produced in K^- absorption, and that the pion energies now vary from about 170 MeV for the processes involving Λ production to about 500 MeV in those cases where the absorption takes place on two-nucleon aggregates. As an example let us mention, that the mean visible energy for 400 MeV, c stopping K^- in the Crystal Ball is reduced from 500 MeV to 380 MeV through our changes and that the visible energy distribution is broadened.

arbitrary units

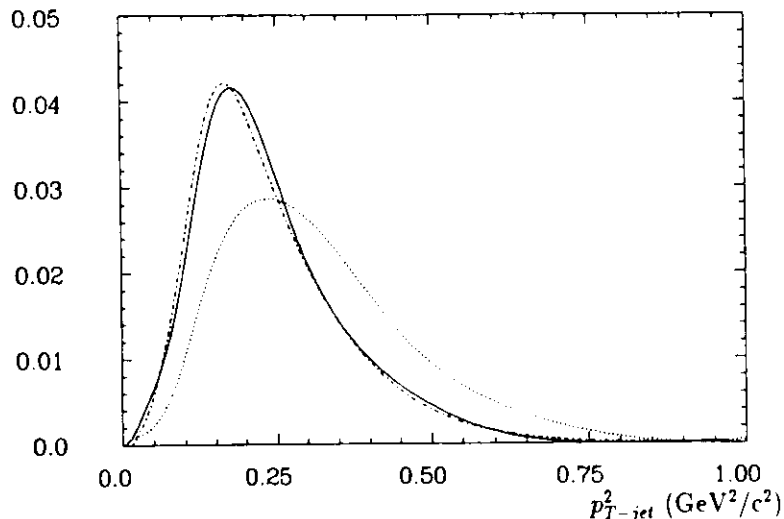


Figure A.19: The p_{T-jet}^2 distribution for the continuum data before accounting for light quenching (dotted) and after all changes (dashed-dotted) compared to the data (solid).

A.3.5 Light Saturation Problem

The standard GHEISHA code does not account for light saturation (light quenching) in the scintillator. The only way this can be effected is an explicit change in the GHEISHA code. With the parametrization used in GHEISHA, the effect of light saturation is described by [74]

$$\frac{\Delta E_{seen}}{\Delta x} = \frac{\frac{\Delta E}{\Delta x}}{1 + \epsilon \frac{\Delta E}{\Delta x}}, \quad (\text{A.20})$$

where E_{seen} , E_{calc} are the observed and calculated energy depositions, ϵ is the quenching factor, and Δx the path length inside the scintillator. The above formula is valid only for particles of unit charge. GHEISHA uses for particles with charge Q greater than unity:

$$\tilde{\epsilon} = 0.8 \epsilon Q. \quad (\text{A.21})$$

The formula A.20 is the expansion of the formula A.22 given in [75] in case of small $\epsilon dE/dx$. We decided to use the original formula

$$\frac{\Delta E_{seen}}{\Delta x} = \frac{\ln \left(1 + 2 \epsilon \frac{\Delta E}{\Delta x} \right)}{2 \epsilon} \quad (\text{A.22})$$

because we encounter large $\epsilon dE/dx$ values. The ϵ values were measured for BGO and some scintillators. We assumed scaling by the density relative to NaI [33]. The effect of light saturation is in our case non-negligible. For minimum ionizing particles assuming 5 MeV/cm as the average energy loss the change is of the order of 3%.

Because we are using the energy depositions from the crystals to define the p_{T-jet}^2 variable, quenching changes the p_{T-jet}^2 distribution dramatically, as it lowers the observed “off jet-axis” energy depositions emerging mainly from the nuclear interactions in the calorimeter. The energy deposited “on jet-axis” is much less affected by the light quenching effect because the particles produced close to the jet-axis are usually energetic. After accounting for light quenching the simulated p_{T-jet}^2 distribution of multihadron events in the Crystal Ball nicely agrees with the data (see figure A.19).

A.3.6 Neutron Transport

As was noticed by various authors [76,77] neutron absorption and transport is extremely difficult to simulate correctly. Compared to neutron energies in the MeV range, the cross section for capture is large for neutron energies of several keV, but very large for energies below the eV level and for thermal neutrons. In our case the energies of secondary produced neutrons are of the order of MeV. The GHEISHA 6 code treats them as thermal as soon as their energies fall below a cutoff value of 1 MeV. In this way we get only a very crude picture of neutron interactions: As they lose their energy slowly—mainly by elastic scattering—neutrons with few MeV can travel far inside the detector before being captured by nuclei. The neutron absorption process can be described as a (n, γ) -reaction where the γ quantum has a well-defined energy typical for the nucleus in which the absorption takes place. GHEISHA 6/7 assumes that the absorption leads to emission of gamma quanta with a total energy of 8 MeV, a typical nucleon binding energy. The energy is emitted in two bursts: one gamma is generated with its energy taken from a Gaussian distribution with a mean of 6.5 MeV and 1 MeV spread, then a second gamma is generated to reach the 8 MeV deexcitation energy. This approximation is only sufficient for applications where high accuracy down to deposited energies of a few MeV is not required. Because of the 10 MeV threshold for the Crystal Ball cluster energy we have to simulate the absorption process with more care, as can be seen in figs. A.7 and A.8. In fact, the mean energy released in the capture process of neutrons in NaI is much lower than 8 MeV [78]. We have modified the GHEISHA routine CAPTUR so that γ lines with a total energy of about 3 MeV are emitted for NaI, whereas we use the default GHEISHA procedure for the other inactive materials in the Crystal Ball detector. These changes were necessary to describe the data just above the threshold of $E_{cluster}$ as can be seen in figs. A.7 and A.8.

The cutoff value for the neutron transport was not changed. An improvement is readily available through the routine NSLDGW in GHEISHA 7, which simulates the moderation down

to thermal energies. However, our studies of neutron simulation were done with GHEISHA 6 only.

A.4 General Remarks on Monte Carlo Techniques

The growing sizes of the Monte Carlo programs require a new look at the entire technique of simulating high energy physics experiments. A scan through the available publications on Monte Carlo shows that no one is really happy with the present state-of-the-art. Huge programs like GHEISHA [33], GEANT [64], FLUKA [79] or HERMES [80] are consuming much of computer time and delivering results of uncertain accuracy. Programs are rather complicated and very hard to debug. Nonetheless, with a large investment of time studying and modifying the Monte Carlo simulation, we are able to report improvement in the description of data, though not complete agreement with measurement.

Because the geometrical routines are the most heavily-used parts of code in the Monte Carlo programs, we spent some time on this subject. It seems that somehow physicists are just now discovering techniques that have been invented for application in CAD/CAM¹ systems. A first step in that direction was done in GEANT, where the graphics interface was made an integral part of the whole package. This saved much time making the debugging of the geometry very much faster. The authors of HERMES report a speed-up factor of 8 as a result of the special geometry package and simultaneous vectorization of the code. The author would like to suggest that the progress referred to in the area of computer graphics should also apply to the problems we are faced with in the Monte Carlo simulation. Moreover the progress in this field is very rapid and gratifyingly there are certain standards which can also be used for physical applications. The "ray tracing" technique is a common method of obtaining high-quality computer graphics with an almost natural appearance. The idea hidden behind this name is purely physical: backtracing of the rays from the eye of the observer to the object in question, subject to all rules of optics. Our Monte Carlo method has a one-to-one correspondence to the case of transparent solids—the progress made in this field can be measured as a reduction from hours of computer time for a single picture down to real time of plotting. The progress in this field is also connected to the progress in storage of the geometrical input and its minimization.

In this respect we must make a few observations. The geometrical interface of the GHEISHA program is particularly ineffective. The geometry routines were previously completely user-contributed. GEANT was a real breakthrough as it requires only the description of the detector as a set of solids, i.e. creates a lattice in space, while the movements inside the lattice are rather done by GEANT itself rather than a users routine. Further progress is made in HERMES where the entire geometry code is prepared using a preprocessor. Another

¹Computer Aided Design, Computer Aided Machining

problem is the flexibility of the program as for example in the decay routines of GHEISHA. All the decays are written as separate routines, so changes require intervention of the users in the source code of the program. Again there is a readily available modification—the decays done as in the LUND Monte Carlo; in such a code new particle decay data can be easily incorporated.

Finally, we would like to discuss the meaning of Monte Carlo accuracy. As already mentioned, the complexity of the strong interactions causes the troubles. In EGS one can choose the simulation accuracy by a momentum cut-off value. An attempt to apply a similar method to the hadronic Monte Carlo will produce unpredictable results as for example in the case of π^- absorption. We would like to note here also the implication of "rare" particle decay modes. In case of high statistics Monte Carlo data sets these can make an important contribution.

Concluding we can say that there are many things that can and have to be done in the field of the modeling of the detector response for hadronic showers. The performance of the Monte Carlo code depends both, on high- and low-energy shower modeling. There is no universal Monte Carlo for all detectors—the particular application of the existing programs has to be done with care.

B. Luminosity Measurement

The luminosity $\tilde{\mathcal{L}}$ is the proportionality factor between the number of events produced per unit time and the cross section for a given process

$$\frac{dN}{dt} = \tilde{\mathcal{L}}\sigma. \quad (\text{B.1})$$

For storage rings the luminosity in one interaction region can be found from the formulae

$$\tilde{\mathcal{L}} = \frac{n^+ n^- \nu N_{\text{bunch}}}{\sigma^+ \sigma^-} \quad (\text{B.2})$$

where n^+ , n^- are the numbers of particles per bunch, ν the revolution frequency, N_{bunch} the number of bunches per beam, σ^+ , σ^- the crossing areas of beams. Eq. B.2 does not have practical application since the quantities used in it for luminosity evaluation are difficult to measure. The luminosity can be found directly from B.1 in the case when we are able to calculate theoretically the cross section for some process having reasonably high counting rate. In the case of e^+e^- storage rings we normally use Bhabha scattering $e^+e^- \rightarrow e^+e^- (\gamma)$ to determine the luminosity. Because of the absence of reliable charge information, we have also had to include the process $e^+e^- \rightarrow \gamma\gamma(\gamma)$ into the calculation of the luminosity. This leads to $\sim 10\%$ increase in the counting rate of the luminosity events (within our selection cuts).

The Crystal Ball measured luminosity at small and large angles with respect to the beam direction. The luminosity measurement at small scattering angles profits from higher statistics, but suffers from systematic uncertainties caused by the extreme sensitivity to small detector misalignments and radiation damage. The small angle luminosity monitor is shown in fig. 3.3, while fig. B.1 shows it in more detail. It consists of four counters located at $\theta \sim 8^\circ$. The measurement at large scattering angles results in smaller statistics, but systematic effects are much less pronounced.

The luminosity is measured from the $e^+e^- \rightarrow e^+e^- (\gamma)$ and $e^+e^- \rightarrow \gamma\gamma(\gamma)$ events observed in the main NaI(Tl) detector. The corresponding graphs (in lowest order QED) are shown in fig. B.2. The measurement at small angles was used for a fast luminosity determination and also as a cross check for large angle luminosity determination. Events with exactly two energy clusters with $E_{\text{cluster}} > 0.35W$ inside $|\cos\theta| < 0.75$ are selected as luminosity events [81]. The integrated luminosity \mathcal{L} is calculated from the number of luminosity events N_{Lumi} using

$$\int \tilde{\mathcal{L}} dt = \mathcal{L} = N_{\text{Lumi}} W^2 / \eta \quad (\text{B.3})$$

where W is the center-of-mass energy. The explicit factor W^2 removes the leading $1/W^2$ cross section dependence, allowing use of a constant conversion factor η within our limited

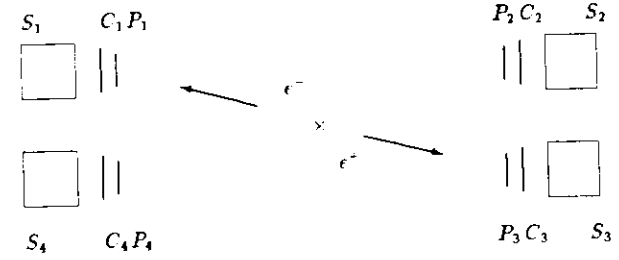


Figure B.1: Small angle luminosity monitor. C , P are scintillation counters, S the lead-scintillator sandwich shower counters. The cross marks the interaction point. The luminosity event is triggered by back-to-back coincidence (1-3, 2-4) CP counters and high energy shower in the corresponding S counters.

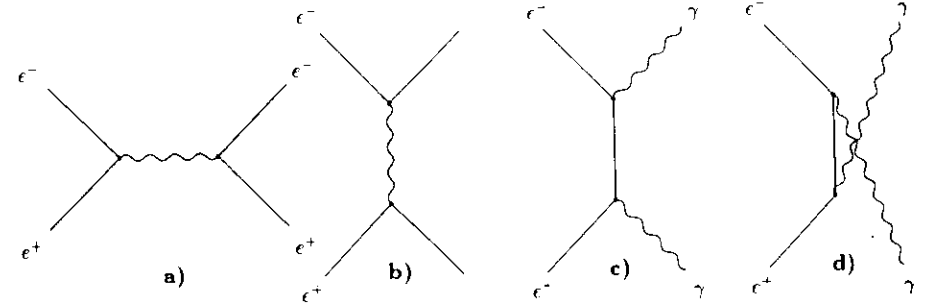


Figure B.2: The lowest order Feynman diagrams for: a) and b) Bhabha scattering, c) and d) $e^+e^- \rightarrow \gamma\gamma$.

W range. The value of η is determined by generating a sample of $e^+e^- (\gamma)$ and $\gamma\gamma(\gamma)$ Monte Carlo events with the program of Berends and Kleiss [34] and passing them through the full detector simulation as described in section 4.2. The luminosity is corrected for the direct decays $\Upsilon \rightarrow e^+e^-$ which contribute to N_{Lumi} .

A 2.5% systematic error on the luminosity was obtained by adding contributions from the following sources in quadrature: 1.0% from Monte Carlo statistics, 1.0% from 4th order QED corrections [82], 1.9% from the dependence on the cuts, 0.7% from the correction for direct decays $\Upsilon \rightarrow e^+e^-$, 0.2% from hadronic and beam-gas background, 0.1% from the non-leading energy dependence of the conversion factor η . It is worth mentioning that the luminosity found by the author [83] applying different selection criteria and of course a different normalization constant η agreed within the 0.5% with the values presented here, thus bringing additional confidence to the estimation of our systematics.

C. Asymmetric Errors of Poisson Distribution

For small counting rates the probability of observing n events is given by the Poisson distribution:

$$P(n) = \frac{\lambda^n \exp(-\lambda)}{n!} \quad (\text{C.1})$$

where λ is a real number. It is both, mean value and variance of the distribution. As this is a discrete distribution we can try to estimate the errors by assuming that our measurement n is the fluctuation at the level of $(1 - CL)$ from the distribution with a mean value λ_{low} smaller than n (see fig. C.1)

$$(1 - CL) = \sum_{i=0}^n \frac{\lambda_{low}^i \exp(-\lambda_{low})}{i!} \quad (\text{C.2})$$

Similarly we can assume that our observed number is the effect of the fluctuation at the level of CL from the distribution with the mean value of λ_{high} . This approach changes the problem from discrete to continuous one. Thus the asymmetric errors can be calculated from the differences $n - \lambda_{low}$, $\lambda_{high} - n$. The value of λ can be found solving eq. C.2 numerically. Taking CL of 16.5% we get the error estimate equivalent to one standard deviation in Gaussian distribution.

arbitrary scale

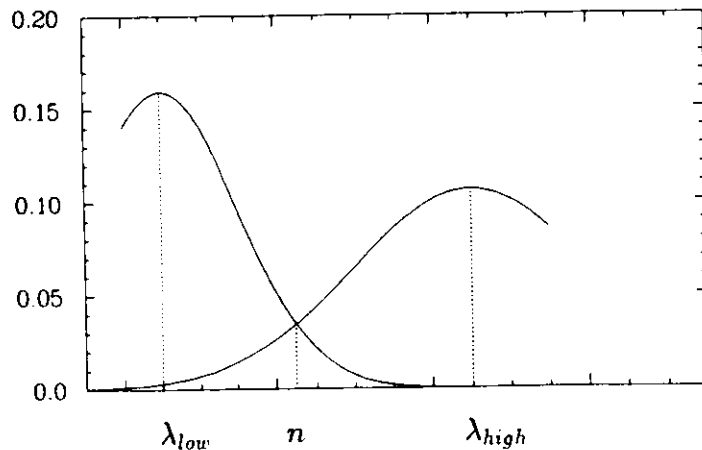


Figure C.1: The calculation of asymmetric errors of Poisson distribution.

Bibliography

- [1] R. Herb et al., Phys. Rev. Lett. **39** (1977) 252.
- [2] R.M. Barnett, M. Dine, L. McLerran, Phys. Rev. **D22** (1980) 594.
- [3] B. Niczyporuk et al. (LENA), Z. Phys. **C15** (1982) 299.
- [4] Z. Jakubowski et al., Z. Phys. **C40** (1988) 49.
- [5] Particle Data Group, M. Aguilar-Benitez et al., Phys. Lett. **170B** (1986) 1.
- [6] G. Bonneau, F. Martin, Nucl. Phys. **B27** (1971) 381.
- [7] F.A. Berends, R. Kleiss, Nucl. Phys. **B178** (1981) 141.
- [8] B. Gittelmann and S. Stone in "High Energy Electron-Positron Physics", edited by A. Ali and P. Söding (World Scientific 1988) p. 273-357.
- [9] R. Van Royen and W. Weisskopf, Nuovo Cim. **50** (1967) 617 and **51** (1967) 583.
- [10] K. Koller et al., Nucl. Phys. **B140** (1978) 449.
- [11] S.J. Brodsky, G.P. Lepage, P.B. Mackenzie, Phys. Rev. **D28** (1983) 228.
- [12] D.R. Yennie, S.C. Frautschi, H. Suura, Ann. Phys. **13** (1961) 379.
- [13] J.D. Jackson, D.L. Scharre, Nucl. Instr. Meth. **128** (1975) 13.
- [14] M. Greco, G. Pancheri-Srivastava, Y. Srivastava, Phys. Lett. **56B** (1975) 367.
- [15] Y.S. Tsai, SLAC-PUB-3129 (1983).
- [16] E.A. Kuraev, V.S. Fadin, Sov. J. Nucl. Phys. **41** (1985) 466.
- [17] F.A. Berends, G.J.H. Burgers, W.L. Van Neerven, Phys. Lett. **185B** (1987) 395.
- [18] M. Abramowitz, I.A. Stegun, "Handbook of Mathematical Functions" (Dover Publications, New York, 1972).
- [19] F.A. Berends, G.J. Komen, Phys. Lett. **63B**, (1976) 432.
- [20] T. Kinoshita, J. Math. Phys. **3** (1962) 650;
T.D. Lee, M. Nauenberg, Phys. Rev. **133** (1964) B1549.
- [21] K. Königsmann: Proc. 6th Int. Conf. on Physics in Collision (Chicago, 1986) and DESY 86-136 (1986);
W. Buchmüller, S. Cooper: MIT preprint MIT-LNS-159 (1987) and in "High Energy Electron-Positron Physics", edited by A. Ali and P. Söding (World Scientific 1988) p. 412-487;
J.P. Alexander et al.: SLAC-PUB-4501 (1988), submitted to Nucl. Phys.
- [22] DESY Storage Ring Group : DORIS, "Proc. of the IXth International Conference on High Energy Accelerators", Stanford 1974.
- [23] The DORIS Storage Ring Group, DESY 79-08 (unpublished).
- [24] H. Neseemann, K. Wille, IEEE Trans. on Nucl. Sci. **NS-30**, 1998 (1983) . DESY Internal Report DESY-M-83-09.
- [25] A.A. Sokolov, I.M. Ternov, Sov. Phys. Dokl. **18** (1964) 1203.
- [26] T. Skwarnicki, Ph. D. Thesis, internal F31 report, unpublished.

- [27] E.D. Bloom, C.W. Peck, *Ann. Rev. Nucl. Part. Sci.* **33** (1983) 143;
M. Oreglia et al. (Crystal Ball), *Phys. Rev.* **D25** (1982) 2259.
- [28] Y. Chan et al., *IEEE Trans. Nucl. Sci.* **NS-25-1** (1978) 333.
- [29] A. Osterheld et al. (Crystal Ball), SLAC-PUB-4160 (1987), submitted to *Phys. Rev. D*.
- [30] T. Sjöstrand, Lund preprint, LU TP 85-10, October 1985.
- [31] B.R. Webber, *Nucl. Phys.* **B238** (1984) 492;
G. Marchesini, B.R. Webber, *Nucl. Phys.* **B238** (1984) 1.
- [32] R. Ford, W. Nelson, SLAC-210 (1978).
- [33] H. Fesefeldt, Aachen preprint, PITHA 85/02.
- [34] F.A. Berends, R. Kleiss, *Nucl. Phys.* **B228** (1983) 537; *Nucl. Phys.* **B186** (1981) 22.
- [35] F.A. Berends, R. Kleiss, S. Jadach, *Z. Was. Acta Phys. Pol.* **B14** (1983) 413.
- [36] S.L. Cartwright, Two-Photon Physics, in: *Proc. 6th Int. Conf. on Physics in Collision* (Chicago, 1986), ed. M. Derrick (World Scientific, Singapore, 1987) pp. 341-361.
- [37] J.M. Vermaseren, *Nucl. Phys.* **B229** (1983) 347;
G.P. Lepage, *Jour. Comp. Phys.* **27** (1978) 192;
B. Muryn - private communication.
- [38] R.H. Dalitz, D.R. Yennie, *Phys. Rev.* **105** (1957) 1598.
- [39] S.I. Serednyakov et al., *JETP* **44** (1976) 1063;
R. Neumann, R. Rosmanith, *Nucl. Instr. Meth.* **204** (1982) 29.
- [40] D.P. Barber et al., *Phys. Lett.* **135B** (1984) 498.
- [41] Ch. Berger et al. (PLUTO), *Z. Phys.* **C1** (1979) 343.
- [42] P. Bock et al. (DESY-Heid.), *Z. Phys.* **C6** (1980) 125.
- [43] H. Albrecht et al. (DASP II), *Phys. Lett.* **116B** (1982) 383.
- [44] B. Niczyporuk et al. (LENA), *Phys. Rev. Lett.* **46** (1981) 92; *Phys. Lett.* **90B** (1981) 169.
In ref. [3], this group revised their $\Gamma_{ee}(1S)$ value, normalizing to their new measurement of the continuum R . However, the R they originally used is closer to the current average R , see ref. [52]; therefore we use their original Γ_{ee} . They used a modified Jackson-Scharre radiative corrections, which correspond to the Greco form given here as eq. 2.28 b (B. Niczyporuk, private communication).
- [45] T. Kaarsberg et al. (CUSB), Contributed paper to the 1987 International Symposium on Lepton and Photon Interactions at High Energies, Hamburg (1987).
- [46] Ch. Berger et al. (PLUTO), *Phys. Lett.* **93B** (1980) 497.
- [47] D. Besson et al. (CLEO), *Phys. Rev.* **D30** (1984) 1433.
- [48] ARGUS Collab. H. Albrecht et al.: *Z. Phys.* **C35** (1987) 283
- [49] R. Giles et al. (CLEO), *Phys. Rev. Lett.* **50** (1983) 877.
- [50] P. Haas et al. (CLEO), *Phys. Rev.* **D30** (1984) 1996.
- [51] H. Albrecht et al. (ARGUS), *Z. Phys.* **C28** (1985) 45.
- [52] R. Giles et al. (CLEO), *Phys. Rev.* **D20** (1984) 1285.
The values for Γ_{ee} , B_{had} before correction for $B_{\mu\mu}$ are quoted in ref. [53]. The value of $2\ell_{quarks}$ used is 0.034, as quoted in R. K. Plunkett, Cornell Ph.D. Thesis (1983).
- [53] D. Andrews et al. (CLEO), *Phys. Rev. Lett.* **50** (1983) 807.
- [54] P. M. Tuts (CUSB), *Int. Symp. on Lepton and Photon Interactions at High Energy*, Ithaca, N.Y. (1983), p. 284; and private communication.
- [55] Particle Data Group, G.P. Yost et al., *Phys. Lett.* **204B** (1988) 1.
- [56] E. Rice et al. (CUSB), *Phys. Rev. Lett.* **48** (1982) 906.
- [57] H. Albrecht et al. (DASP II), *Phys. Lett.* **116B** (1982) 383.
- [58] Ch. Berger et al. (PLUTO), *Phys. Lett.* **81B** (1979) 410.
- [59] S.G. Gorishny, A.L. Kataev and S.A. Larin, *Proc. Conf. on Hadron Structure*, Smolenice, Czechoslovakia, November 1987, Vol. 14 Physics and Applications, Inst. of Phys. EPRC, Slovak Academy of Sciences, Bratislava, 1988 p. 180 and Dubna preprint JINR E2-88-254.
- [60] R. Marshall, *Z. Phys.* **C43** (1989) 585 and preprint RAL-88-049, proceedings of the XXIV Int. Conf. on High Energy Physics, München 1988 p. 901 and preprint RAL-88-089.
- [61] W. De Boer, SLAC-PUB-4428 (1987).
- [62] G. D'Agostini, W. de Boer and G. Grindhammer, "Update of the CELLO Analysis on R ", contributed paper to the XXIV Int. Conf. on High Energy Physics, München 1988.
- [63] Z. Jakubowski, S. Keh, "CB Monte Carlo Progress Report", April 1985, internal F31 note (unpublished).
- [64] R. Brun, F. Bruyant, M. Maire, A.C. McPherson, P. Zancarini, "GEANT 3", CERN DD/EE/84-1, September 1987.
- [65] M. Suffert, \bar{p} -LEAR NOTE No. 41, March 1979, unpublished.
- [66] W. Metzger, "Comparison of the LUND Monte Carlo with Data on and near the Upsilon", preprint HEN-278, Nijmegen 1987, (unpublished).
- [67] M. Kobel, June 87, July 87 internal F31 note (unpublished);
Z. Jakubowski and M. Kobel, preprint DESY 89-165 (1989) accepted by NIM.
- [68] R.M. Sternheimer et al., *Phys. Rev.* **B3** (1971) 3681.
- [69] R.M. Sternheimer et al., *Phys. Rev.* **88** (1952) 851.
- [70] R.M. Sternheimer et al., *Atomic Data and Nucl. Data Tables.* **30** (1984) 261.
- [71] J.D. Jackson, "Classical Electrodynamics", 1975, New York.
- [72] G. Mechterheimer et al., *Nucl. Phys.* **A324** (1979), 379.
U. Klein et al. *Nucl. Phys.* **A329** (1979), 339.
- [73] C. Van der Velde-Wilquet et al., *Nuovo Cimento* **39A** (1977) 538.
- [74] J.B. Birks, *Proc. of the Phys. Society* **64** (1951), 874.
- [75] G.T. Wright, *Phys. Rev.* **91** (1953) 1282.
- [76] R. Wigmans, "High Resolution Calorimetry", invited talk given at "Experimental Methods for Colliding beam physics", SLAC, March 1987, USA.
- [77] R. Aleksan and F. Pierre, preprint DPhPE 87-12.
- [78] S.M. Shafroth "Response of Sodium Iodide to Neutrons" in "Scintillation Spectroscopy of Gamma Radiation", Gordon and Breach, London, 1967.
- [79] W.R. Nelson, T.M. Jenkins and J. Ranft, SLAC-PUB-4150 (1986).
- [80] P. Cloth et al., preprint Jül-2203, May 1988.
- [81] K. Wachs, "Luminosity Constant", October 1986, internal F31 note (unpublished).
- [82] B. Naroska, *Phys. Rep.* **148** (1987) 98.
- [83] Z. Jakubowski, "Note on the CB Lumi Constant", March 1986, internal F31 note (unpublished);
Z. Jakubowski, "Luminosity Constant", April 1986, internal F31 note (unpublished).

This study was performed within the Crystal Ball Collaboration:

D. Antreasyan, H.W. Bartels, D. Besset, Ch. Bieler, J.K. Bienlein, A. Bizzeti, E.D. Bloom, I. Brock, K. Brockmüller, R. Cabenda, A. Cartacci, M. Cavall-Sforza, R. Clare, A. Compagnucci, G. Conforto, S. Cooper, R. Cowan, D. Coyne, G. Drews, A. Engler, G. Folger, A. Fridman, J. Gaiser, D. Gelpman, G. Glaser, G. Godfrey, K. Graaf, F.H. Heimlich, F.H. Heinsius, R. Hofstadter, J. Irion, B. Janssen, Z. Jakubowski, K. Karch, K. Kees, S. Keh, T. Kiel, H. Kilian, I. Kirkbride, T. Kloiber, M. Kobel, W. Koch, A.C. König, K. Königsmann, R.W. Kraemer, S. Krüger, G. Landi, R. Lee, S. Leffer, R. Lekebusch, A.M. Litke, W. Lockman, S. Lowe, B. Lurz, D. Marlow, H. Marsiske, W. Maschmann, P. McBride, H. Meyer, B. Muryn, F. Messing, W.J. Metzger, B. Monteleoni, R. Nernst, B. Niczyporuk, G. Nowak, C. Peck, C. Pegel, P.G. Pelfer, B. Pollock, F.C. Porter, D. Prindle, P. Ratoff, M. Reidenbach, B. Renger, C. Rippich, M. Scheer, P. Schmitt, J. Schotanus, J. Schütte, A. Schwarz, F. Selonke, D. Sievers, T. Skwarnicki, V. Stock, K. Strauch, U. Strobusch, J. Tompkins, H.J. Trost, B. van Uitert, R.T. Van de Walle, H. Vogel, A. Voigt, U. Volland, K. Wachs, K. Wacker, W. Walk, H. Wegener, D. Williams, P. Zschorsch

All these people contributed to the data taking, hardware and software maintenance. Whenever we explicitly used somebody else's work in our offline data analysis we supplied a reference or footnote. Otherwise the author is solely responsible for the failures or mistakes.

The main research was done at DESY in Hamburg. Some work was also performed at Cracow Institute of Nuclear Physics. Prof. K. Rybicki was the supervisor for the writing up of thesis.